UNIVERSITY OF MISKOLC
FACULTY OF MECHANICAL ENGINEERING AND INFORMATICS

NUMERICAL SIMULATION OF THE HEAT AND MASS FLOW OF A SOLAR COLLECTOR APPLYING ALTERNATIVE LIQUIDS

PHD THESES

Prepared by

Mustafa Moayad Hasan
Mechanical Engineering Department (BSc),
Mechanical Engineering Department (MSc)

ISTVÁN SÁLYI DOCTORAL SCHOOL OF MECHANICAL ENGINEERING SCIENCES
TOPIC FIELD OF BASIC ENGINEERING SCIENCES
TOPIC GROUP OF TRANSPORT PROCESSES AND MACHINES

Head of Doctoral School

Dr. Gabriella Bognár
DSc, Full Professor

Head of Topic Group

Dr. László Baranyi
Full Professor

Scientific Supervisor

Dr. Krisztián Hriczó
Associated professor

Miskolc
2025

CONTENTS I
SUPERVISOR'S RECOMMENDATIONS III
LIST OF SYMBOLS AND ABBREVIATIONS IV
1. INTRODUCTION 5
1.1. Overview of Energy Sources and Solar Technologies 5
1.2. Various Solar Systems: Challenges and Enhancements 6
1.2.1. Freestanding DPSTCs 7
1.2.2. Building- Integrated DPSTCs 9
1.3. Enhancement of Solar Collector Applying Various Heat Transfer Fluids 10
1.4. Various Analysis Models of DPSTC 13
1.5. Research Objectives 15
1.5.1. MATLAB- Based Modeling 15
1.5.2. CFD Analysis using ANSYS 15
1.6. Outline of the thesis 16
2. METHODOLOGY 17
2.1. Mathematical Approaches 17
2.2. MATLAB Simulation 20
2.3. ANSYS Modelling and Validation 20
2.4. Friction Factor, Pumping Power, and Collector Area Size-Reduction 24
2.5. Energy Savings, CO_2 Emissions-Reduction and Annual Cost Savings 25
3. A DUAL- PURPOSE SOLAR COLLECTOR AS A PARALLEL FLOW HEAT EXCHANGER: A NOVEL MATHEMATICAL FRAMEWORK 27
3.1. Modelling The DPSTC 27
3.2. The Accuracy of Predictions 30
3.3. The Predicted Plate and Water Temperatures 31
3.4. The Predicted Heat Gain 32
4. THE OPTIMAL APPROACH OF VARIOUS ANALYSIS METHODOLOGIES OF A DUAL-PURPOSE SOLAR COLLECTOR 34
4.1. Structure of The Investigated DPSTC 34
4.2. The Developed Numerical Simulation and Error Metrics 35
4.3. The Performance of DPSTC 37
5. NUMERICAL INVESTIGATION OF A DUAL- PURPOSE SOLAR COLLECTOR USING DIFFERENT LIQUIDS 40
5.1. The Number of Investigated Cases 40
5.2. Thermophysical Properties of Working Fluids 40

5.3. The Effect of Airflow on The Exit Temperature of DPSTC 42
5.4. The Effect of Airflow on The Heat Gain of DPSTC 44
5.5. The Effect of Airflow on The Efficiency of DPSTC 45
6. EVALUATION OF A DUAL-PURPOSE SOLAR COLLECTOR USING MONO-NANOFLUIDS: A CFD SIMULATION **48**
6.1. Thermophysical Properties of Nanofluids 48
6.2. The Impact of Airflow on The Exit Temperatures of DPSTC 49
6.3. The Impact of Airflow on The Performance of DPSTC 51
6.4. The Impact of Liquid flow on The Exit Temperatures of DPSTC 53
6.5. The Impact of Liquid flow on The Performance of DPSTC 55
7. ENERGY, ECONOMIC, AND ECOLOGICAL ASPECTS OF A DUAL-PURPOSE SOLAR COLLECTOR USING VARIOUS LIQUIDS **58**
7.1. Thermophysical Properties of HNFs 58
7.2. Numerical Investigation Using HNFs 59
7.3. DPSTC Size Reduction 61
7.4. Fossil Fuel and Electricity Consumption With Associated CO_2 Emissions 62
7.5. Pressure Drop and Pumping Power 65
8. THESES – NEW SCIENTIFIC RESULTS **69**
ACKNOWLEDGEMENTS **71**
REFERENCES **72**
LIST OF PUBLICATIONS RELATED TO THE TOPIC OF THE RESEARCH FIELD **83**

SUPERVISOR'S RECOMMENDATIONS

I am pleased to write a letter of recommendation for Mustafa Moayad Hasan, who completed his doctoral research under my supervision at the István Sályi Doctoral School of Mechanical Engineering at the University of Miskolc. Throughout his doctoral studies, Mustafa consistently demonstrated exceptional intellectual abilities, strong research skills, and unwavering commitment to academic excellence, developing two innovative mathematical approaches that had not been used before. In addition, he carried out two separate modeling phases in his research, one using MATLAB and the other using ANSYS.

Mustafa's research focuses on the energy efficiency analysis of dual-purpose solar collectors, using alternative fluids and different analytical approaches, as well as various simulation tools. His work is characterized by scientific rigor, originality, and a high level of technical competence. He has demonstrated outstanding abilities in the design and execution of complex simulations, data analysis, and in-depth and accurate interpretation of results. His research results have contributed significantly to the development of the field, and he has actively shared these results with the academic community through presentations at domestic and international conferences and publications in renowned journals, including Q1, Q2, and Q4 journals.

Overall, Mustafa has proven himself to be a diligent, creative, and independent researcher who approaches challenges with perseverance and analytical acumen. I am confident that he will successfully defend his dissertation and continue to make valuable contributions to the academic community.

In summary, I wholeheartedly support and strongly recommend Mustafa Moayad Hassan for the degree of PhD.

Miskolc, 07. 11. 2025

Dr. Krisztián Hriczó

Supervisor

LIST OF SYMBOLS AND ABBREVIATIONS

NOMENCLATURE

SYMBOLS			GREEK LETTERS	
A	*Area [m^2]*		τ	*Transmittance*
C_p	*Specific heat* [*J/(kg.K)*]		α	*Absorptance*
C	*Capacity rate*		ε	*Effectiveness*
F_R	*Heat removal factor*		η	*Energy efficiency*
h	*Convection heat transfer coefficient [$W/(m^2K)$]*		ρ	*Density [kg/m^3]*
I	*Incedent solar radiation [W/m^2]*		μ	*Dynamic viscosity [mPa.s]*
k	*Thermal conductivity [W/(m.K)]*		ζ_{coal}	*Coal thermal conversion rate*
U	*Overall heat transfer coefficient* [*$W/(m^2.K)$*]		ζ_{gas}	*Conversion rate of the gas*
$\dot{m}$	*Mass flow rate* [*kg/s*]		ζ_{elec}	*Conversion rate of electric*
Re	*Reynolds number*		**Subscripts**	
Pr	*Prandtl number*		u	*Useful*
Nu	*Nusselt number*		$DPSC$	*Dual- purpose solar collector*
Q	*Heat transfer rate [W]*		f	*Fluid*
T	*Tempertaure [°C]*		t	*Total, top*
V	*Mean fluid velocity [m/s]*		c	*Collector*
Abbreviations			L	*Losses*
PV	*Photovoltaic*		a	*Ambient*
ST	*Solar Thermal*		b	*Bottom*
FPSCs	*Flat-Plate Solar Collectors*		s	*Side*
ETCs	*Evacuated Tube Collectors*		out	*Outlet*
PTCs	*Parabolic Trough Collectors*		in	*Inlet*
SACs	*Solar Air Collectors*		$min.$	*Minimum*
SWCs	*Solar Water Collectors*		$max.$	*Maximum*
PVT	*Photovoltaic-Thermal*			
DPSTC	*Dual-Purpose Solar Thermal Collector*			
HTFs	*Heat Transfer Fluids*			
CFD	*Coputational Fluid Dynamics*			
HNFs	*Hybrid Nanofluids*			

1. INTRODUCTION

1.1. Overview of Energy Sources and Solar Technologies

Energy is infiltrating all areas that impact our daily lives. It originates from either traditional sources such as coal, oil, and natural gas, collectively referred to as fossil fuels, or from alternative sources like solar, wind, hydro, nuclear, and geothermal, known as renewable energy [1]. Traditional energy resources raise numerous issues, including scarcity, volatile pricing, exhaustion, detrimental environmental effects, and heightened air pollution along with greenhouse gas emissions [2]. These pressing issues highlight the necessity for renewable energy sources to serve as viable alternatives to conventional energy in a diverse range of applications. Among renewable energy sources, solar energy is an eco-friendly, affordable, clean, and carbon-free option for energy [3]. Solar energy plays a crucial role in reducing greenhouse gas emissions and combating climate change. It provides a sustainable alternative to fossil fuels, enhancing global energy security and protecting the environment [4]. Various technologies and methods are utilized to capture, convert, and distribute solar energy for diverse applications. Solar energy technologies are primarily categorized into two major types: Photovoltaic (PV) systems and Solar Thermal (ST) systems. Both technologies harness solar energy but convert it into different forms of usable energy [5]. PV systems convert the visible part of sunlight directly into electricity using the photovoltaic effect [6]. PV systems consist mainly of panels made up of photovoltaic cells, inverters to convert DC to AC power, and various mounting and tracking systems to maximize solar exposure [7]. Unlike PV systems, ST systems consist of collectors that transform radiant heat from the sun into thermal energy, which can be utilized for heating fluids (both air and liquids), space heating, and even cooling through different technologies [8]. There are various kinds of solar collectors, including Flat-Plate Solar Collectors (FPSCs), Evacuated Tube Collectors (ETCs), and Parabolic Trough Collectors (PTCs). Each variety provides unique advantages and is suited for particular uses and operating circumstances, with each designed for varying temperature ranges and applications [9]. Among these kinds of collectors, FPSCs are widely used due to their simple design, low maintenance costs, lack of a sun-tracking system, and effectiveness in various climatic conditions [10]. FPSCs typically consist of a glass cover, an absorber plate (often painted black), and insulation layers. They can be categorized based on the type of fluid they use for heat transfer, primarily into Solar Air Collectors (SACs) and Solar Water Collectors (SWCs) [11]. FPSCs can be used for heating in both domestic and industrial sectors, act as solar cooling devices for applications such as air conditioning and refrigeration and can also be integrated into building heating systems to reduce reliance on fossil fuels [12].

1.2. Various Solar Systems: Challenges and Enhancements

As the PV systems convert the visible part of sunlight into electricity, the infrared portion is converted into thermal energy, which significantly raise the temperature of the PV panels, resulting in reduced power output and lifespan. Thus, it is crucial to explore effective cooling techniques for PV panels [13]. This can be achieved by integrating PV system with ST system, resulting in a hybrid technology known as a Photovoltaic-Thermal (PVT) system. This system converts solar radiation into both electrical and thermal energy, making it particularly suitable for applications with limited space, such as building-integrated systems, where separate collectors would be less efficient [14]. This arrangement captures the heat generated by the PV module to produce thermal energy, while also ensuring the high electrical efficiency of the PV module.

The main challenges associated with FPSCs include heat loss due to convective and radiative processes, along with low heat transfer coefficient between the absorber plate and the circulating fluid. These factors significantly reduce the thermal efficiency of FPSCs, constituting a major downside [15]. Researchers have focused on improving this aspect for decades through various strategies like employing various materials and designs for the absorber plate [16]. For instance, using reflectors with trapezoidal or parabolic shapes can enhance sunlight concentration on the collector plate, resulting in increased efficiency [17]. Additionally, incorporating nanofluids as heat transfer fluids can greatly boost thermal performance [18]. Other methods to minimize heat losses include applying selective coatings, using transparent insulation, and adjusting the collector's tilt. Furthermore, incorporating polymeric materials for the absorber elements can reduce costs while enhancing efficiency [19]. One of the most feasible solutions to overcome the drawbacks of FPSCs is by combining of two ST technologies (i.e., air and liquid heaters) in a single facility, known as a Dual-Purpose Solar Thermal Collector (DPSTC). This bi- fluid collector is mainly a FPSC with two separated and sealed sections, one for air heating and the other for liquid heating.It is one of a novel avenue that offers several benefits, including:

- Increased thermal performance and annual utilization of solar energy.
- Reduced installation area and overall costs.
- Achieving high temperatures with effective heat delivery from solar thermal systems.
- Generate hot air and hot liquid simultaneously or separately.

In general, the combination of two solar technologies in one device is an effective solution to address the limitations of traditional solar systems. This dual-function approach can optimize the use of available space by combining two functionalities into one unit, making it particularly useful in areas with limited space for solar installations. Figure 1.1 illustrates the categorization of dual-function collectors. The present study specifically focuses on DPSTC rather than PVT systems, and the following subsections provide detailed discussions on the diverse types of DPSTC, as well as their different designs and applications.

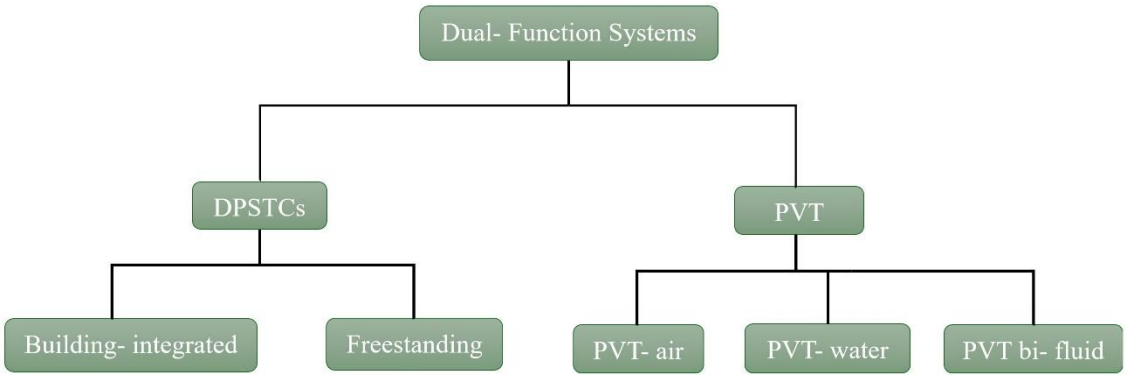

Figure 1.1. Classification of dual-function solar energy systems based on collector type and integration approach.

1.2.1. Freestanding DPSTCs

This category is fabricated, installed, and operated independently without being attached to buildings or other structures. These collectors are versatile and can be utilized in various applications, including residential, industrial, and agricultural settings. They can be installed in open spaces, reducing the need for building-mounted systems and allowing for more flexible placement [20]. Freestanding collectors require significant space for installation, which can be a limitation in densely populated areas. Additionally, tracking systems can be integrated with these types of collectors to enhance their efficiency, as they are always oriented towards the sun. However, the cost-effectiveness of these upgrades should be carefully assessed to balance performance and economic viability [21].

The initial research on the DPTSC was conducted by Assari et al. [22]. They constructed their collector by integrating V-corrugated air channels to the bottom of an absorber plate, where water pipes were positioned on top. Their investigations evaluated the collector in both single and dual modes. They found that the dual mode operation of the collector outperformed single mode, increasing outlet air temperature by 20% due to water circulation. In a related study, Assari et al. [23] conducted both experimental and theoretical investigations on the same collector, examining three air channel types: straight fin, triangular fin, and no fin. A variety of parameters were analyzed, including solar radiation, inlet water temperature, and airflow rate. Their findings indicated that higher inlet water temperatures decrease water heat gain but increase air heat gain, thus enhancing overall system efficiency. A separate study conducted an energy and exergy analysis of this collector, varying water inlet temperatures from 40°C to 90°C and air flow rates from 0.01 to 0.07 kg/s.m². Results showed that energy efficiency decreased with increasing water inlet temperatures, while exergy efficiency increased up to 60°C before declining. Conversely, higher air flow rates improved both energy and exergy efficiencies, especially in the triangle passage design [24, 25]. An L-shaped fin was developed to improve heat transfer in the air section of a DPTSC. Experiments showed average water heating efficiency of 50% and air heating efficiencies of 52% (daily mean) and 55% (instantaneous). Theoretical analysis indicated that higher airflow rates boost the efficiency of the L-shaped air channel but lower the outlet air temperature [26]. A DPTSC with a porous medium beneath the absorber plate

marks a new approach. Numerical analysis using ANSYS showed a temperature difference of 68 °C in the lower channel with the porous media, compared to 24.7 °C in the upper channel without it. The porous matrix improved the collector's thermal efficiency by enhancing heat transfer [27]. Integrating a vertical water storage tank with DPSTC was proposed by Nematollahi et al. [28]. This vertical tank reduces temperature stratification, leading to a more consistent fluid temperature and improved thermal efficiency by minimizing heat loss. Results show the dual-purpose system's efficiency is 3% to 5% higher than that of a single-purpose system. Recently, Kumar et al. [29] investigated a novel DPSTC using a pressurized shot-blasting technique to enhance the inner surface of the air channel and absorber plate for better thermal performance. They tested solar glycol with multi-walled carbon nanotube (MWCNT)-based nanofluids at 0.1 vol% and 0.2 vol% to boost the convective heat transfer coefficient. The air heater tests showed a maximum temperature difference of 25 °C, a heat transfer rate of 452W, and thermal efficiency of 33.2%. For the water heater, the maximum temperature difference was 18.32 °C, with a heat transfer rate of 680W and thermal efficiency of 51.03%. More and Pote [30] proposed an improved design of the DPSTC, which features serpentine copper tubes positioned above the absorber plate, along with a triangular air channel located beneath the absorber. The highest recorded efficiencies for this design reached 72.4% in experimental tests and 68.81% theoretically, with heat losses limited to only 20%. In contrast, conventional collectors typically experience heat losses ranging from 33% to 50%. DPSTC acts as both a heat collector during the day and a cold collector at night, as Miao et al. [31] demonstrated. Their design uses a double-pane polycarbonate cover instead of a single-pane glass. In heat collection mode, liquid is heated while flowing through copper tubes in the absorber plate. At night, it dissipates heat through radiation and convection between the panes. Experimental results indicate that this design offers greater heating and cooling capacities than uncovered collectors, leading to reduced energy consumption.

One application of DPTSC is its integration with drying systems for agricultural products. In this combination, the hot air produced by the DPTSC is utilized in an indirect forced convection dryer, while the hot water it generates can be used for domestic purposes or as a phase change material to facilitate continued drying during the night [32]. Other application of DPSTC is by integrating with humidification-dehumidification system to enhance the freshwater production. Rajaseenivasan and Srithar [33] conducted an experimental study on humidification-dehumidification system, consisting of a DPSTC, a humidifier, and a dehumidifier. The DPSTC supplies hot water and air to the humidification chamber, where they mix efficiently. The humid air is then condensed in the dehumidification chamber using cooling water. The study found that increasing the flow rates of air, water, and cooling water improved freshwater productivity. Additionally, raising the outlet air temperature with concave semi-circular turbulator in the DPSTC further enhanced productivity, resulting in an overall efficiency of 68%. Using DPSTC, storage tank, and an auxiliary heater in the automobile industry represent new trend. It can be used in some processes such as parts washing, paint drying, and corrosion protection [34].

Ma et al. [35] examined the effects of design parameters like insulation thickness, air channel height, and copper pipe diameter on DPSTC performance in both water and air heating modes. They

found that back insulation should be at least 0.06 meters thick to minimize heat loss. The diameter and number of copper tubes significantly impact water heating efficiency but have little effect on air heating. Optimal depths for the two air channels were determined, with water heating mode achieving over 55% daily efficiency and instantaneous air heating reaching up to 60%.

Zhang et al. [36] tested three operating modes of DPSTC including air heating, water heating, and combined air-water heating modes. The experimental results indicated that mode A achieved an average efficiency of 51.3%, mode B reached 51.4%, while mode C had the highest efficiency at 73.4%. They also found that the mass flow rate significantly affects efficiency, outlet temperature of the fluid, and heat transfer effectiveness.

1.2.2. Building- Integrated DPSTCs

DPSTC can be integrated in the building sector since it reduces building energy consumption and provides space heating in winter, water heating and lowers the cooling load in summer as well. Ji et al. [37] introduced a building-integrated dual-function solar collector that operates using natural water circulation. This new design was tested experimentally and numerically for water heating. The results showed a 2% reduction in the cooling load of a test room equipped with the collector compared to one without it. Furthermore, during winter, the average indoor temperature was 24.7 °C, while the ambient temperature was only 4.8 °C. Moreover, the DPSTC can enhance the thermal environment of the building and provide hot water in summer without overheating problems caused by other conventional passive solar heating systems.

To improve the aesthetic appeal and reduce heat loss, Luo et al. [38] introduced an innovative tile-shaped DPSTC that included an additional layer of Polymeric Methyl Methacrylate covering the glass. The collector experimentally tested and compared with DPSTC without Polymeric Methyl Methacrylate covers and one with semicircular covers. The daily thermal efficiency of the tile- shaped collector when it was operated in water heating mode varied from 54% to 61.8%. In contrast, the efficiencies for the DPSTC with semicircular covers and the DPSTC without Polymeric Methyl Methacrylate covers varied from 44.7% to 59.2% and 35.5% to 67.4%, respectively. Further research on the same collector in water heating mode was conducted by He et al. [39]. They investigated the effects of factors such as inlet water temperature, water mass flow rate, solar radiation, and ambient air temperature on thermal efficiency. The results indicated that a lower inlet water temperature, a higher water flow rate, a higher ambient air temperature, and lower solar radiation all contributed to improved thermal efficiency of the module. Additionally, a comparative study revealed that the tile-shaped covered collector achieves higher efficiency than a flat-plate collector under higher temperature operations. In a related study, Hu et al. [40] designed a novel roof type dual function solar collector by using a wavelike cover. They developed a dynamic model using MATLAB software and validated it experimentally. The model was adopted to predict the thermal efficiency and outlet water temperature of this collector under the same operating conditions employed by He et al. [39]. The simulated results indicated that the novel design achieved higher thermal efficiency and lower heat

loss coefficient. Furthermore, the wavelike collector provided better consistency for traditional Chinese buildings compared to other roof-integrated solar collectors.

Ma et al. [41] studied the thermal performance of a room with DPSTC compared to a reference room without it, under both controlled and non-controlled conditions. In the non-controlled scenario, the test room averaged 8.24 °C, while the reference room averaged 4.81 °C. Under controlled conditions, the temperature was set at 18 °C, with power consumption of 4.322 kWh for the test room and 7.796 kWh for the reference room. The study also found improved thermal efficiency with copper water tubes in the DPSTC compared to traditional passive solar air heaters without these tubes.

1.3. Enhancement of Solar Collector Applying Various Heat Transfer Fluids

The efficiency of solar heaters is highly dependent on the Heat Transfer Fluids (HTFs), which captures solar energy while circulating through the collector's tubes. HTF plays a vital role in multiple applications, including the heating and cooling buildings, automobiles, and biomedicine [42]. The enhancement of thermal performance in STs is a key research focus, particularly through the use of advanced HTFs [43].

Water is the predominant HTF utilized in FPSCs, but it has limitations like inferior thermal properties and challenges related to freezing and scale formation [44]. Moreover, blending Ethylene-Glycol or Propylene Glycol with water can create a versatile HTF suitable for varying climates, as glycol raises water's boiling point and lowers its freezing point. However, glycol-based liquids have about a third of the thermal conductivity compared to water [45].

In addition to water and glycol mixtures, other fluids, including molten salt (Hitec), mineral oil, Therminol, and Dowtherm oil, are utilized as HTFs in STs due to their beneficial thermo-physical characteristics. In a study of FPSC for domestic heating, three HTFs (Dowtherm A, Molten salt, and Therminol VP-1) have been tested [46]. Therminol VP-1 demonstrated superior performance due to its thermo-physical properties, particularly with a trapezoidal groove profile, achieving high thermal gain and efficiency. Another study using numerical simulations identified mineral oil and Dowtherm as better HTFs than water for FPSCs due to their lower heat capacities, with mineral oil reaching the highest exit temperature, making it suitable for industrial use [47].

The incorporation of ultrafine solid particles creates nanofluids, which enhance the efficiency of STs. These fluids demonstrate improved thermophysical properties, including better thermal conductivity and heat transfer capabilities, making them valuable for various industrial and engineering applications [48]. Recent studies have investigated nanofluids - comprising solid metals, metal oxides, and carbon nanostructures - as a promising alternative for enhancing the efficiency of FPSCs and other thermal applications [49-51]. Nanofluids, as HTFs, significantly affect the performance of FPSCs due to their high thermal conductivity, low density, and excellent optical properties [52]. Despite numerous studies on nanofluids, none have definitively identified the best nanofluid due to the varying design parameters, nanoparticle sizes, and conditions [53]. To identify

the ideal nanofluid, a focus should be placed on experimental, numerical, and theoretical studies that test multiple nanofluids under the same conditions. Numerous studies have assessed the impact of various nanofluids on the thermal and exergy performance of FPSCs [54]. Among the tested fluids, Multi-Walled Carbon Nanotube (MWCNT)/water and copper oxide (CuO)/water nanofluids consistently showed superior performance, typically at concentrations of 0.005% to 2% [55]. Another study investigated the effects of various nanofluids on the energy and exergy efficiencies of FPSC also indicated that MWCNT/water nanofluid achieved the highest energy efficiency improvement of 23.47%, followed by graphene/water at 16.97% and CuO/water at 12.64% [56]. It was observed that among all the investigated nanofluids, MWCNT-H_2O and CuO-H_2O are the most commonly utilized fluids in solar collectors. An investigation of a FPSC using CuO, Al_2O_3, and ZrO_2 nanofluids revealed efficiencies of 55% for CuO, 51.3% for Al_2O_3, 47% for ZrO_2, and 38% for water [57]. A study analyzed the effects of metal oxide nanofluids (CuO, Al_2O_3, SiO_2, TiO_2) through numerical methods. Results showed that CuO/water nanofluid was the most effective compared to other metal oxide nanofluids (Al_2O_3, SiO_2, and TiO_2), showing an increase in exergy efficiency by 4.35% and the convective heat transfer coefficient by 22% [58]. Experimental and numerical investigations highlighted that nanofluids significantly enhance heat transfer and system efficiency, especially when used with optimized geometries like fins or grooves. The inclusion of fins in absorbers further increased the thermal performance. Additionally, the use of CuO/water nanofluid reduced operational costs while maintaining high efficiency, and Al_2O_3/water offered advantages in maintenance and weight. A study examined how different nanofluids (Al_2O_3, SiO_2, and CuO) affect the performance of FPSC. It was found that CuO/water nanofluid offers superior thermal efficiency at lower volume percentages and reduces annual costs by 27.88%. Additionally, Al_2O_3/water nanofluid is preferred for its lower maintenance needs and reduced weight [59]. An evaluation of absorber performance was conducted using water, Al_2O_3/water , and CuO/water nanofluids. Results showed that Al_2O_3/water at 0.01% volume fraction achieved the highest efficiency of 77.5%, a 21.9% increase over pure water. CuO/water reached a peak efficiency of 73.9%, representing a 16.2% improvement over water [60]. In a separate study, experiments were conducted using CuO/water and Al_2O_3/water nanofluids in two different types of absorbers—finned and unfinned. The unfinned absorber's thermal efficiency improved by 2.1% and 4.05% with 0.2 wt% and 0.4 wt% CuO nanoparticles, respectively. The finned absorber saw enhancements of 3.02% and 5.5% with the same nanoparticle concentrations. For Al_2O_3 nanoparticles, the unfinned collector improved by 3.7% and 6.54%, and the finned tube by 4.8% and 7.8%. Overall, the finned absorber outperformed the unfinned one, especially with nanofluids [61]. Hawwash et al. [62] evaluated alumina oxide-water and copper oxide-water nanofluids in FPSC using a validated Coputational Fluid Dynamics (CFD) model. They found that a nanoparticle volume fraction of 0.5% for copper oxide nanoparticles achieved the highest thermal efficiency. Additionally, CuO/water nanofluid outperformed Al_2O_3/water nanofluid under the same conditions. Bazdidi-Tehrani et al. [63] numerically investigated TiO_2/water and CuO/water nanofluids, finding that higher nanoparticle concentrations moderately improved solar collector efficiency. CuO/water outperformed TiO_2/water , achieving a peak efficiency of 89%. Overall, nanofluids improve FPSC performance, but the degree of improvement depends on nanoparticle type, concentration, flow rate, and collector

design. However, in the context of the literature survey, it was observed that among all the investigated nanofluids, MWCNT/water and CuO/water are the most commonly utilized fluids in solar collectors. These nanofluids possess beneficial properties that can enhance the overall thermal performance of solar systems.

Currently, Hybrid Nanofluids (HNFs), combining various types of nanoparticles in a base fluid, have also shown promise in improving thermophysical, optical, rheological, and morphological properties [64]. Numerous studies show that HNFs in FPSCs provide higher thermal efficiency compared to mono nanofluids and conventional base fluids [65]. Carbon-based HNFs that combine graphene or carbon nanotubes with metallic nanoparticles exhibit excellent thermal conductivity, improved heat transfer, and increased stability, while reducing particle agglomeration and sedimentation [66]. Combining carbon-based and metallic nanoparticles improved thermal conductivity, heat transfer rates, and increased stability compared to single component nanofluids [67]. The effects of HNFs created from a (50:50) mixture of MWCNTs and Al_2O_3 in FPSC was investigated. The study analyzed how solar radiation intensity, nanoparticle volume concentration, and flow rate impact efficiency at various mass flow rates. Results indicated that the hybrid nanofluid improved efficiency by 26%, 29%, and 18% at flow rates of 1.5 L/min, 2.5 L/min, and 3.3 L/min, respectively [68]. Another research group investigated the effect of Cu-MWCNTs and Distilled Water (DW) in FPSC [69]. They found that varying inclination angle, flow rate, and volume concentration enhanced thermal efficiency by up to 26.28% compared to DW. The energy and exergy performance of FPSC with CuO-MWCNT and MgO-MWCNT hybrid nanofluids were studied by Verma et al. [70]. They found that MgO-MWCNT fluids had higher energy and exergy efficiencies (71.56% and 70.55%) compared to CuO-MWCNTs (70.63% and 69.11%).

Following the discovery of Single-Wall Carbon NanoTubes (SWCNT), researchers have investigated their unique properties [71]. The heat transfer enhancement in FPSC using SWCNT-CuO/water improved the heat transfer coefficient by 8% and boosted thermal efficiency by 5.16% [72]. Esfe et al. [73] conducted an experimental study on the thermal conductivity of SWCNTs-MgO/ ethylene glycol hybrid nanofluids. They found that the HNF exhibited superior thermal conductivity over single component nanofluids.

In a recent and innovative experimental investigation, ZrO_2-SiC nanoparticles at 0.1% concentration were tested in FPSC, highlighting a 31.64% increase in thermal efficiency and a 28.31% boost in exergy efficiency [74]. The studied literature indicated that water remains the preferred base fluid for HNFs in FPSCs compared to other types of base liquids [75].

When selecting nanoparticles for use in solar collectors, particularly focusing on size and concentration, several key factors should be considered to optimize performance:

- Nanoparticle size and concentration : Smaller nanoparticles (5- 20 nm) are more effective in enhancing the efficiency of solar collectors compared to larger sizes [76]. Lower

concentrations have been shown to yield higher thermal conductivity due to their high surface area-to-volume ratio [77]. Future studies should focus on optimizing these parameters to balance enhanced thermal conductivity and manageable viscosity.

- Aggregation and Sedimentation: Nanoparticles tend to aggregate, reducing their optical performance and stability. The use of additives or surfactants helps maintain uniform dispersion, minimize aggregation, and enhance stability by preventing particle clumping [78].
- Hybrid Nanofluids: Combining different types of nanoparticles can enhance both thermal conductivity and optical absorption properties [79].
- Production Cost and Environmental Impact: The production cost and environmental impact of nanofluids need to be addressed. This includes evaluating the lifecycle environmental impact and developing cost-effective production methods [80].

The future of nanoparticle additives in solar thermal collectors is promising, with numerous opportunities for enhancing efficiency and performance. By focusing on optimizing nanoparticle properties, ensuring stability, developing advanced formulations, and considering environmental and economic impacts, researchers can pave the way for more efficient and sustainable solar thermal technologies.

Thanks to the exceptional thermophysical characteristics of mono nanofluids and HNFs, more compact solar thermal collectors can be created without losing performance. Smaller collectors use less material, lower costs, and reduce manufacturing energy consumption. Numerous studies have evaluated the economic and environmental influences of solar systems. Faizal et al. [81, 82] conducted two separate studies on reducing the size of FPSC using MWCNT and Al_2O_3 nanofluids. They found that MWCNT nanofluid could reduce the collector size by up to 37%, while Al_2O_3 achieved a 24% reduction, lowering overall costs. Area reductions of 25.6% for Al_2O_3, 21.6% for SiO_2, 22.1% for TiO_2, and 21.5% for CuO lead to less weight, energy use, and production costs. Additionally, nanofluids can reduce CO_2 emissions by about 170 kg compared to traditional collectors [83]. A 0.05% volume of cerium oxide-water nanofluid was found to produce lower emissions of sulphur oxides, CO_2, and nitrogen oxides compared to plain water [84].

1.4. Various Analysis Models of DPSTC

Like other solar collector types, evaluating DPSTC is a crucial endeavour that aims to maximize their efficacy and validate their practical applicability. Based on the literature survey, there are numerous researchers have conducted different methods to analyse DPSTC.

Researchers have created models based on the principle of energy conservation for each collector component, including the glass cover, absorber plate, air and water streams, and back plate. Each component is described by its own energy balance equation that outlines how energy is transferred and transformed within the system, incorporating concepts such as conductive and convective heat transfer and longwave radiation exchange between the various components. A mathematical model

was developed to simulate the collector's performance, considering various factors affecting heat transfer and flow rates. The model assessed how changes in parameters like air flow rate and collector configuration influenced thermal efficiency, achieving a relative deviation in efficiency of less than 4% when compared to experimental results [26]. Somwanshi and Sarkar [85] proposed a simple mathematical model for a dual-purpose collector cum storage air-water heater. This model, derived from the energy balance equation for each collector component, estimates the theoretical temperature changes of both air and water based on parameters such as ambient temperature, solar radiation intensity, and mass flow rates. The model was validated through experiments, where the exit air and water temperatures were recorded and compared against theoretical predictions. Hu et al. [40] developed a mathematical expression for a novel wavelike roof DPSTC using energy conservation principles. Their dynamic model, built in MATLAB, accounted for conductive and convective heat transfer, as well as longwave radiation exchange. The simulation results were consistent with experimental data. Ma et al. [35] developed a mathematical model for both air and water heating modes under a steady-state energy balance equation. Their numerical model emphasized the main components of the collector: glass cover, backboard, and absorber plate. A finite difference method was applied to discretize the energy equations over time and space. The numerical results were compared against the experimental data to validate the model's accuracy, revealing good agreement.

Researchers worldwide widely employ the Effectiveness-Number of Transfer Unit (ε-NTU) method for conducting comprehensive performance assessments of the DPSTC. Researchers choose this technique because of its simplicity and versatility, which allows it to reliably forecast collector performance regardless of the system’s design. The effectiveness-NTU method is beneficial when only the inlet temperatures of fluids are known, simplifying the analysis by eliminating the iterative calculations required in methods like Log Mean Temperature Difference (LMTD) [86]. It's widely used in heat exchanger design, allowing for the determination of heat transfer effectiveness in solar collectors under varying conditions. The method's simplicity and reliability make it valuable for assessing the thermal performance of different collector geometries, providing a time-saving approach for researchers. Assari et al. [23] developed the mathematical model of the DPSTC based on the ε-NTU method. This model assumes mean temperatures for the absorber, water tubes, and air channels, treating the flows as homogeneous. It omits considerations of conduction and radiation in the tubes and channels, as well as convection and radiation losses from the back and sides. The model employs input parameters like solar radiation, water inlet temperature, and airflow rate. The heat exchange effectiveness was calculated, and the model was validated with experimental data. In a separate study, Assari et al. [24] focused on assessing both energy and exergy efficiencies of the DPSTC using the ε-NTU model. They examined three different shapes of air passages-triangular, rectangular, and commonly shaped channels-and discovered that the triangular passage displayed the highest exergy and energy efficiency. In the same context, Jaffari et al. [25] investigated the energy and exergy performance of DPSTC by employing the ε-NTU approach, specifically examining triangular-shaped air channels. Their study focused on air flow rate and water inlet temperature as key factors, with results indicating that DPSTC exhibits higher energy and exergy efficiency compared to individual

collectors. Zhang et al. [87] investigated the thermal performance of the DPSTC operating in three modes: air heating, water heating, and air-water compound heating. The mathematical representation of the DPSTC has been derived by applying the principles of the ε-NTU method. The models were validated with experimental data, demonstrating relative errors of less than 6%.

1.5. Research Objectives

The primary aim of this research is to conduct a comprehensive numerical investigation into the thermal performance of DPSTC by applying novel mathematical models and a range of alternative heat transfer fluids. To achieve this, the research was structured into two main phases:

1.5.1. MATLAB- Based Modeling:

The first phase focused on establishing a robust and novel theoretical framework for analyzing the DPSTC. The objectives were:

- To model the DPSTC as a parallel-flow heat exchanger and develop a novel mathematical framework based on the effectiveness-NTU (ε-NTU) method, an approach not previously applied for the analysis of this collector type.
- To develop and comparatively evaluate three different mathematical models for analyzing the DPSTC, each implemented in a separate MATLAB code, to identify the most accurate and robust methodology for predicting its performance.

1.5.2. CFD Analysis using ANSYS

The second phase involved applying the established models to evaluate the performance enhancements achievable with various advanced heat transfer fluids through detailed CFD simulations. The objectives were:

- To numerically investigate the influence of oil-based fluids (Therminol VP-1, Dowtherm A) as an alternative to water in DPSTC.
- To evaluate the performance of the DPSTC when using mono-nanofluids (CuO-H_2O, MWCNT-H_2O).
- To assess the thermal performance of the DPSTC when using hybrid nanofluids (MWCNT-CuO/H_2O, SWCNT-CuO/H_2O, ZrO-SiC/H_2O).
- To conduct a comprehensive energy, economic, and ecological analysis of the DPSTC, evaluating collector size reduction, CO_2 emissions, fossil fuel and electricity savings, pressure drop, and pumping power.

This research presents a novel approach by modeling DPSTC as a parallel flow heat exchanger, which has not been previously explored in the literature. It is also the first study to conduct CFD simulations to investigate the performance of oil-based fluids, mono-nanofluids, and various hybrid nanofluids in this specific type of solar collector. The work further contributes a unique environmental

and economic assessment of using these advanced liquids in a DPSTC, addressing previously unstudied aspects such as collector size reduction and pumping power requirements.

1.6. Outline of the thesis

The Introduction of this thesis underscores the significance of renewable energy, particularly solar energy. It reviews relevant literature that outlines the background, objectives, and structure of various solar systems, with a specific focus on DPSTC. Additionally, it discusses the different models adopted by researchers for analyzing DPSTCs. The introduction also discusses the diverse types of hear transfer fluids employed in ST systems. Chapter 2 discusses the methodology employed in the analysis of the collector, including the geometry used, the mathematical approaches, numerical methods applied, and the appropriate numerical software utilized, and the parameters employed. In Chapter 3, a novel mathematical approach using the ε-NTU method is applied to analyze the DPSTC, treating it as a parallel flow heat exchanger—an area not previously explored in the literature. In Chapter 4, I developed three mathematical approaches centered on formulating the heat removal factor equation, which is essential for calculating the effective heat gain of solar collectors. Each model was implemented through a dedicated MATLAB code, and the most accurate and efficient version was selected. In Chapter 5, I investigated the impact of oil-based heat transfer fluids (Therminol VP-1 and Dowtherm A), alongside water, on the performance of the DPSTC using ANSYS Fluent. The analysis enabled the identification of the fluid that most effectively enhances the overall thermal performance of the system. In Chapter 6, I investigated the impact of mono-nanofluids—specifically multi-walled carbon nanotube (MWCNT)-water and copper oxide (CuO)-water, at 0.5% volume concentration using ANSYS Fluent. We conducted two simulation phases, each employing different operating parameters. We identified the optimal operating conditions and the superior nanofluid, highlighting the clear advantages of using nanofluids to enhance the thermal performance of the system. In Chapter 7, I conducted two simulation phases. The first evaluated the impact of three hybrid nanofluids—1% vol MWCNT-CuO/H_2O, 1% vol SWCNT-CuO/water, and 0.1% vol ZrO-SiC/water, on DPSTC performance under various operating conditions. The second phase involved an environmental assessment of all numerical results from the current and previous chapters, focusing on fuel and electricity savings, CO_2 emission reductions, and the influence of different fluids on size reduction, pressure drop, and pumping power in the DPSTC.

2. METHODOLOGY

In this chapter, I provide and explore the diverse mathematical methodologies that have been applied to analyze DPSTC. These methods are diverse, encompassing both novel mathematical models and numerical simulations. The proposed mathematical models are developed and solved using MATLAB software, while computational fluid dynamics (CFD) are employed for numerical analysis. The following subsections will discuss each approach adopted throughout our study.

2.1. Mathematical Approaches

Mathematical models of DPSTC face challenges such as fluid interaction, heat loss, and the complexities of air ducts. These issues make it challenging to analyze the system under variable incident energy and multiple influencing parameters. Nevertheless, several mathematical models have been developed to analyze and optimize the performance of DPSTC.

For modeling the DPSTC, the most crucial output parameter is the useful heat gain of the collector ($Q_{u,DPSC}$) which includes both water and air sections, and it is computed using the following equation [23]:

$$Q_{u,DPSC} = Q_{u,\ water} + Q_{u,\ air}\ . \tag{2.1}$$

The useful heat gain ($Q_{u,f}$) for any solar thermal collector is determined by the variance between the solar energy absorbed ($Q_{Absorbed}$) which depicts the transformation of incident solar irradiance into useful heat gain and the total heat losses (Q_{Lost}), which comprise both thermal and optical losses (U_L) [88]:

$$Q_{u,f} = Q_{Absorbed} - Q_{Lost}\ . \tag{2.2}$$

These quantities can be computed using the standard formulations provided by Duffie and Beckman [88]:

$$Q_{Absorbed} = (\tau\alpha) I_t\ A_c\ , \tag{2.3}$$

$$Q_{Lost} = U_L\ A_c\big(T_{plate} - T_a\big)\ , \tag{2.4}$$

where $\tau\alpha$ is transmittance- absorptance product, and I_t portrays the incident irradiance on a slanted surface, A_c stands to the collector area, T_{plate} represents the absorber plate temperature, and T_a corresponds to the ambient temperature.

Thus, combining these terms as shown by Duffie and Beckman [88], Equation (2.2) becomes:

$$Q_{u,f} = A_c\big[(\tau\alpha) I_t - U_L(T_{plate} - T_a)\big]\ , \tag{2.5}$$

where the overall heat loss coefficient of the collector (U_L) stands for heat losses from the top (U_t), back (U_b), and sides (U_s) surfaces of the solar collector [88]:

$$U_L = U_t + U_b + U_s \, . \tag{2.6}$$

The useful heat gain can be expressed in terms of the inlet fluid temperature ($T_{f,in}$) and a parameter called the collector heat removal factor (F_R). This widely used expression is formulated in Duffie and Beckman [88] as:

$$Q_{u,f} = A_c \, F_R\big[(\tau\alpha) I_t - U_L\big(T_{f,in} - T_a\big)\big]. \tag{2.7}$$

The heat removing factor of a collector (F_R) establishes a connection between the real increase in useful energy and the potential yield if the entire collector surface reaches the operating fluid temperature at the inlet [23]:

$$F_R = \frac{\dot{m}_f \, C_{p,f} \, (T_{f,out} - T_{f,in})}{A_c\big[(\tau\alpha) I_t - U_L (T_{f,in} - T_a)\big]} \, , \tag{2.8}$$

here the subscript (f) stands for fluid, which is water or air, $\dot{m}_f$ represents the flow rate of water or air, and $C_{p,f}$ is the fluid's specific heat.

The previously outlined mathematical equations are implemented for a single-purpose solar collector or when the DPSTC is operated in a single mode (i.e., air or water mode). Researchers adopting a segmented approach to DPSTC analysis, dividing it into distinct air and water sections, often utilize the equations outlined above.

In contrast, the DPSTC can be treated as a unified entity implementing the Effectiveness- NTU method into the analytical framework. The useful heat gain in this approach is given as [23]:

$$Q_{u,f} = \varepsilon_f \, \dot{m}_f \, C_{p,f} \, (T_{plate} - T_{f,in}), \tag{2.9}$$

rearranging this equation:

$$Q_{u,f} = \varepsilon_f \, \dot{m}_f \, C_{p,f} \, (T_{plate} - T_{f,in} - T_a + T_a). \tag{2.10}$$

Thus;

$$Q_{u,f} = \varepsilon_f \, \dot{m}_f \, C_{p,f} \, \big(T_{plate} - T_a\big) + \varepsilon_f \, \dot{m}_f \, C_{p,f} \, (T_a - T_{f,in}), \tag{2.11}$$

but, $\big(T_{plate} - T_a\big)$ can be suistituted by using equation (5), the useful heat gain is obtained as:

$$Q_{u,f} = \varepsilon_f \, \dot{m}_f \, C_{p,f} \left(\frac{A_c(\tau\alpha) I_t - Q_{u,f}}{A_c \, U_L}\right) + \varepsilon_f \, \dot{m}_f \, C_{p,f} \, (T_a - T_{f,in}). \tag{2.12}$$

Rearranging equation (2.12), gives:

$$Q_{u,f} = \left(\frac{\varepsilon_f \dot{m}_f C_{p,f}}{U_L A_c + \varepsilon_f \dot{m}_f C_{p,f}}\right) A_c\left[(\tau\alpha)I_t - U_L(T_{f,in} - T_a)\right], \quad (2.13)$$

by comparing Equations (2.7) and (2.13), it can be noticed that term (F_R) in the effectiveness- NTU approach is:

$$F_R = \frac{\varepsilon_f \dot{m}_f C_{p,f}}{U_L A_c + \varepsilon_f \dot{m}_f C_{p,f}}. \quad (2.14)$$

The concept of effectiveness parameter is defined as the ratio of the actual heat delivery to the maximum heat delivery that can be transferred to fluids, and it is given as [23]:

$$\varepsilon_f = 1 - exp\left[-\frac{h_f A_f}{\dot{m}_f C_{p,f}}\right], \quad (2.15)$$

here, ε_f measures the heat exchange effectiveness, A_f is the fluid's heat exchange surface area, and h_f is the heat transfer coefficient of the fluid.

From Eq. (2.15), NTU defines as:

$$NTU = \frac{h_f A_c}{\dot{m}_f C_{p,f}}. \quad (2.16)$$

A new term, the heat removal coefficient for the second fluid (U_f), is incorporated into Equation (2.6) [23]:

$$U_f = \frac{\varepsilon_f \dot{m}_f C_{p,f} (T_{plate} - T_{f,in})}{A_f (T_{plate} - T_a)}. \quad (2.17)$$

Thus, Equation (2.6) will be reformulated as:

$$U_L = U_t + U_b + U_s + U_f. \quad (2.18)$$

In the present study, we treat the DPSTC as a parallel flow heat exchanger and utilize the effectiveness equation for such exchangers, as referenced in standard heat transfer handbooks, in our mathematical analysis and it can be calculated as [89]:

$$\varepsilon_f = \frac{1 - exp[(-h_f A_f / C_{min.})(1 + C_{min.}/C_{max.})]}{(1 + C_{min.}/C_{max.})}, \quad (2.19)$$

here $(C = \dot{m}_f C_{p,f})$ is defined as the capacity rate, which relies on the mass-flow rates and specific heats of the fluid. The minimum and/or maximum capacity rate may pertain to either the air or water.

The heat transfer coefficient of the fluid, (h_f) can be computed based on the Nusselt number relation in the following manner [90]:

$$Nu = 3.66 + \frac{0.0668\left(\frac{D_h}{L}\right)Re\ Pr}{1+0.04\left[\left(\frac{D_h}{L}\right)Re\ Pr\right]^{2/3}}, \tag{2.20}$$

in which the notations D_h and L represent the diameter and the length of water risers, respectively. Re and Pr represent the Reynolds and Prandtl numbers, respectively. These dimensionless numbers are calculated by Duffie and Beckman [88] as:

$$Re = \frac{\rho\ V\ D_h}{\mu}, \tag{2.21}$$

$$Pr = \frac{C_{p,f}\ \mu}{k}, \tag{2.22}$$

where ρ is the fluid density, V is the mean fluid velocity, μ is the dynamic viscosity, and k is the thermal conductivity.

The thermal efficiency (η) of any solar thermal device is a crucial measure of its performance. It is stated to be the proportion of beneficial thermal yield to the entire amount of incident irradiation. Therefore, the energy efficiency of the DPSTC is calculated as:

$$\eta = \frac{Q_{u,DPSC}}{A_c I_t}. \tag{2.23}$$

2.2. MATLAB Simulation

In the current study, a comprehensive MATLAB code has been meticulously developed to simulate the DPSTC based on the proposed mathematical model detailed in subsection 2.1. The code incorporates an extensive array of specifications and design parameters, covering both the physical and thermal properties pertinent to the water and air sections that constitute the DPSTC.

During the simulation process, a set of meteorological data, which includes external temperature, wind speed, and incident solar irradiation, was employed. These data points, along with the operating parameters-specifically the mass flow rates for the inlet air and water, as well as their respective inlet temperatures-mirror those used by [28].

2.3. ANSYS Modelling and Validation

ANSYS software package is a powerful computational fluid dynamic (CFD) widely used for simulating fluid flow, heat transfer, and other related phenomena. The modeled DPSTC consists of a single glass cover, an absorbent plate, seven lower-bonded parallel liquid tubes attached to the absorber plate, seven upper-bonded V-corrugated air channels attached to the top of the absorber and connected to the back insulation from the bottom (see Figure 2.1).

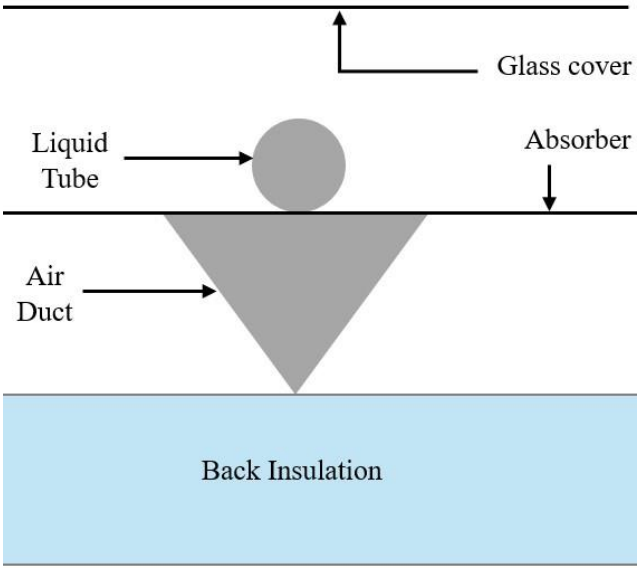

Figure 2.1. Schematics of the DPSTC system studied.

This design is consistent with that proposed by Assari et al [23] and the specific dimensions and characteristics of the collector, as modelled in ANSYS, are thoroughly outlined in Table 2.1.

Table 2.1. Detailed specifications of the DPSTC [23].

Absorber material	Aluminum sheet, 1.0 mm thickness	Absorber length	1.94 m
Air duct material	Galvanized steel, 0.5 mm thickness	Absorber width	0.95 cm
Cover material	Glazing, 6.0 mm thickness	No. of glazing	1.00
Pipe material	Zinc, 1.0 mm thickness	Pipe diameter	7.00 mm
Air duct shape	Triangle with a 60° angle	Air channel height	6.00 cm

The three-dimensional geometry of the collector was built using the ANSYS Design Modeler. Half of a single air duct and water tube is modeled to optimize the approach. By incorporating symmetrical planes into the design, calculations could be simplified. This technique included building a semi-circular construction with a symmetric wall, substantially minimizing the required mesh elements. Consequently, this ensures improved mesh quality and simultaneously reduces the analysis processing time. The developed 3D geometry of DPSTC is shown in Figure 2.2. The model contains a half-liquid tube and a half-air channel.

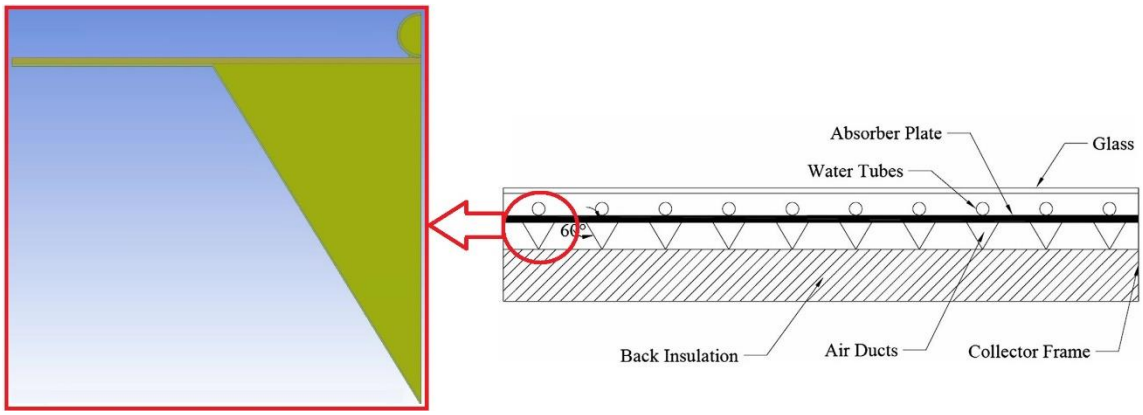

Figure 2.2. The cross-sectional view of the DPSTC (right) and its corresponding simplified ANSYS model (left).

The conformal mesh is generated, as shown in Figure 2.3. The mesh is developed, consisting of tetrahedron elements with a structured mesh (prism layers) and a growth rate of 1.01. The boundary conditions of the studied model are defined by creating named selections in the Fluent meshing. Among these named boundaries, symmetry boundaries are helpful for minimizing the size of the computational domain. They are used when the physical geometry and the anticipated flow or thermal pattern show mirror symmetry.

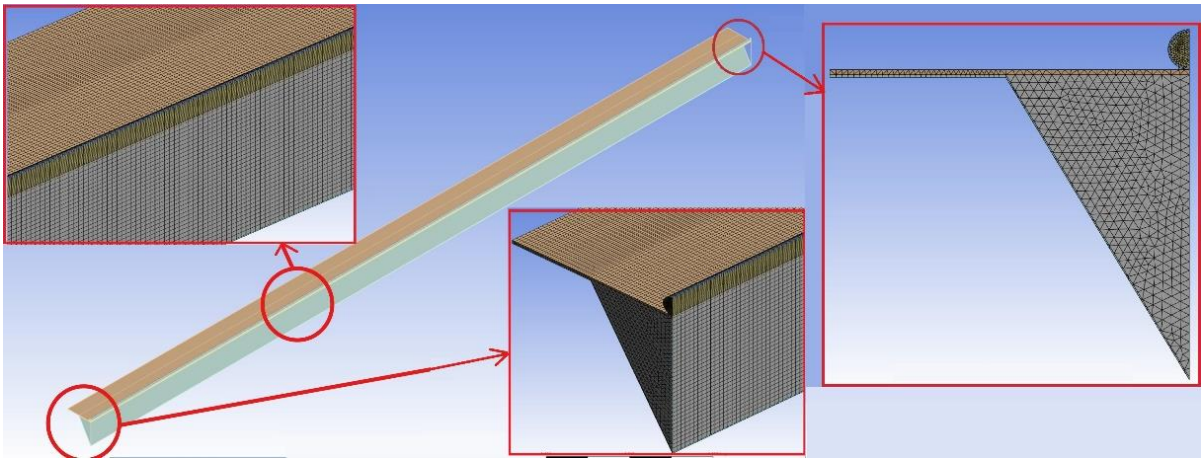

Figure 2.3 Geometry and the mesh configuration for the studied DPSTC.

The mesh quality is rigorously tested using the conventional grid-independence test method. This test is a critical stage in CFD as it ensures that results depend on the physical model, not the mesh size. The number of mesh elements increased from 595,182 to 1,334,844, and there was no considerable change in temperature after the increment of the number of elements after 1,308,692 (Figure 2.4). The average mesh quality, skewness, and orthogonal quality are 0.78983, 0.12956, and 0.87791, respectively, which are considered suitable for computations, ensuring the reliability of our results.

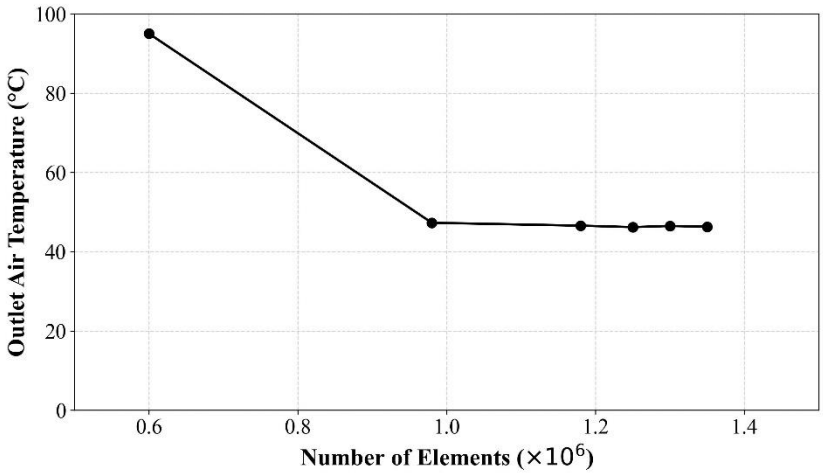

Figure 2.4. Mesh independence test.

The following assumptions are considered in the current investigation for the solution setup in ANSYS Fluent:

- The fluid flow is laminar, as the Reynolds number falling within the laminar regime.
- The fluid flow is steady, meaning its properties do not change with time.
- The properties of materials remain invariant with temperature changes.
- The fluids are assumed incompressible, meaning their density remains constant throughout the flow.
- Heat losses via the borders are discarded.
- No-slip conditions are imposed on the system.

The energy equation is implemented with the laminar flow model, assuming a constant heat flux on the absorbent plate and a steady inlet fluid temperature. For numerical analysis, the pressure, momentum, and energy equations are discretized using a second-order upwind method. Gradient calculations are performed using the Green-Gauss node-based approach. Pressure-velocity coupling is achieved through a coupled scheme, while the remaining simulation settings are maintained at their default values. The residual criteria for the simulation are established with continuity and momentum set at 10^{-5}, and energy at 10^{-6}.

The current CFD model simplifies nanofluids by treating them as a single-phase, homogeneous fluid with enhanced thermophysical properties, which is computationally efficient but overlooks the complex multi-phase nature of these fluids. To capture physical realism over time, effects like Brownian motion, sedimentation, and aggregation need to be considered in the future work. Brownian motion describes the erratic movement of nanoparticles due to collisions with fluid molecules, crucial for enhancing thermal conductivity. Although the single-phase model implicitly accounts for this by using an effective thermal conductivity, a more detailed two-phase model, like an Eulerian-Lagrangian or Discrete Phase Model, could better simulate particle motions and heat transfer [91]. Sedimentation occurs when denser nanoparticles settle out of suspension, due to their higher density compared to the base fluid. This occurs at low flow rates or during stagnant conditions, leading to an uneven distribution of nanoparticles, establishing a concentration gradient within the fluid. Over time, this can lead to fouling on the surfaces of collectors, obstruct the narrow flow channels, and impair

the overall thermal efficiency of the system. The current steady-state model does not account for this time-dependent decline in performance [92]. Aggregation involves nanoparticles clustering together to create larger aggregates due to inter-particle forces. This phenomenon is harmful because it lowers the effective surface area of the nanoparticles available for heat transfer, can alter the thermophysical characteristics of the fluid—particularly by raising viscosity, which increases the pumping power needed—and accelerates sedimentation, as larger clusters settle more rapidly [93]. To address these effects, transitioning to a more complex multi-phase simulation, such as ANSYS Fluent's Mixture or Eulerian models, is essential. This would allow tracking of nanoparticle concentration and incorporate changes in fluid properties, providing valuable insights into the long-term stability and reliability of the solar collector that the current single-phase model does not adequately address.

To rigorously assess the current model and establish its precision and dependability in forecasting outcomes, a thorough validation process has been conducted. Comprehensive data on solar insolation, as well as air and inlet temperatures, have been meticulously gathered from the experiments conducted by Assari et al. [23]. Following this, simulations were executed under equivalent conditions to those of the original experiments. The results from the simulations strikingly align with the experimental data, as illustrated in Figure 2.5. The relative error is computed to demonstrate the convergence between simulated and experimental findings. The highest value of this error is 1.044%, while the minimum value is 0.085%.This striking concordance confirms that the current CFD model of the solar collector has been validated successfully.

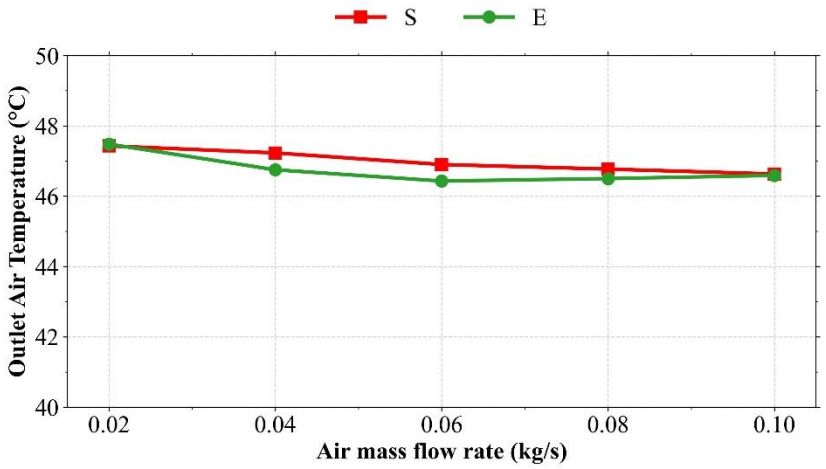

Figure 2.5. Validation of the present simulation results (S) against the experimental data (E) reported by Assari et al. [23].

2.4. Friction Factor, Pumping Power, and Collector Area Size-Reduction

The friction factor (f) for all the examined liquids in the simulation is determined by the following equation [94]:

$$f = \frac{\Delta P}{\left(\frac{L}{D}\right)\left(\frac{\rho v^2}{2}\right)}, \tag{2.24}$$

here L, D, ρ, and v denote the pipe length, pipe diameter, liquid density, and liquid flow velocity, respectively. The values of total pressure drop (ΔP) across the collector are obtained directly from the simulation results.

The velocity of the liquid v, is given by:

$$v = \frac{\dot{m}}{\pi\, \rho \frac{D^2}{4}}\,. \tag{2.25}$$

A key parameter in solar collectors is the pumping power (W_P) which is required to derive the fluid through the collector's pipes or ducts. It is crucial in evaluating system efficiency as it is significant in maintaining a constant flow in the system. Factors affecting pumping power include the mass flow rate, pipe roughness, fittings, bends, valves, and other obstructions. It is defined as [95]:

$$W_P = \Delta P \left(\frac{\dot{m}}{\rho}\right). \tag{2.26}$$

This study aims to evaluate whether using different HTFs instead of water in DPSTC can reduce collector size, leading to cost savings and more efficient use of installation space. The reduction in the collector area (A_{red}) is given as [96]:

$$A_{red} = \frac{\dot{m}_f\, C_{p,f}\, (T_{out,f} - T_{in,f})}{\eta\, I_t\, (\tau\alpha)}. \tag{2.27}$$

2.5. Energy Savings, CO_2 Emissions-Reduction and Annual Cost Savings

Heating water for residential and industrial consumes electric or fossil fuel-burning heaters, particularly in cold season. However, due to rising carbon emissions, there is a shift towards renewable energy sources. Employing DPSTC, a form of FPSC, can reduce greenhouse gas emissions and reliance on fossil fuels [97].

This study calculates the amount of coal (M_{coal}), natural gas (V_{gas}), and electricity (P_{elec}) tht can be saved by using DPSTC instead of using conventional coal- fired, gas- fired, and electric boilers to produce the same heat gain. The corresponding CO_2 (M_{CO_2}) emissions associated with these savings are also calculated. The calculations assume that the DPSTC operates for one hour daily at noon, using a single solar radiation value during the simulation.

If a coal-burning boiler is used for heating purposes, the coal mass and CO_2 emissions are determined as follows [98]:

$$M_{coal} = \frac{Q_{DPSC}}{q_{coal}\, \zeta_{coal}}, \tag{2.28}$$

$$M1_{CO_2} = \frac{3.67\, F\, Q_{DPSC}}{q_{coal}\, \zeta_{coal}}, \tag{2.29}$$

where, q_{coal} is the coal calorific value, (MJ/Kg), ζ_{coal} is the coal thermal conversion rate, 65%, and F is carbon emission factor, 0.73 [98].

If a natural gas boiler is used, the gas volume which can be consumed, and its related CO_2 emissions is determined as [98]:

$$V_{gas} = \frac{Q_{DPSC}}{q_{gas}\,\zeta_{gas}}, \tag{2.30}$$

$$M2_{CO_2} = \frac{3.67\,F\,Q_{DPSC}}{q_{coal}\,\zeta_{gas}}, \tag{2.31}$$

here, q_{gas} is the natural gas calorific value, (MJ/Kg), ζ_{gas} is the conversion rate of the natural gas 98%, and F is the carbon emission factor, 0.40 [98].

Finally, if an electric boiler is used, its energy saving and CO_2 emissions are as follows [98]:

$$P_{elec} = \frac{Q_{DPSC}}{\zeta_{elec}}, \tag{2.32}$$

$$M3_{CO_2} = \frac{3.67\,F\,Q_{DPSC}}{q_{coal}\,\zeta_{elec}}, \tag{2.33}$$

here ζ_{elec} represents the conversion rate of electro thermal value 80%, and F is the carbon emission factor, 0.87 [98].

Environmental evaluation requires the calculation of annual CO_2 emissions and related costs [99]. To accomplish this, it was assumed that the DPSTC operates for 6 hours a day, and for 300 days a year, taking the average price of 14.5 $ for CO_2/ton [100].

3. A DUAL-PURPOSE SOLAR COLLECTOR AS A PARALLEL FLOW HEAT EXCHANGER: A NOVEL MATHEMATICAL FRAMEWORK

This chapter introduces a specialized mathematical framework to analyze the unique thermal behavior of the DPSTC. The approach is conceptually grounded in modeling the collector as a parallel flow heat exchanger, a strategy justified by its dual-fluid channel structure. The analysis is built upon two well-established, foundational methodologies: the fundamental solar thermal equations as formulated by Duffie and Beckman [88] and the ε-NTU method. The primary novelty of this work lies in a specific and consequential modification within the ε-NTU framework. While previous analyses of the DPSTC have often employed a generalized expression for collector effectiveness (Eq. 2.15), this study makes a crucial distinction. By treating the DPSTC rigorously as a parallel flow heat exchanger, the effectiveness (ε_f) is calculated using the specific equation for that configuration (Eq. 2.19). This value is then used to determine the heat removal factor (F_R) via Eq. 2.14. This targeted application of the parallel flow effectiveness equation represents the core analytical contribution of this chapter. To the author's best knowledge, this specific analytical path has not been previously applied to the DPSTC, offering a more theoretically consistent model for this unique collector type. To implement and validate this framework, a comprehensive MATLAB code was developed. The model was simulated using a set of meteorological data, including external temperature, wind speed, and incident solar irradiation. To ensure the reliability and robustness of the suggested model, the simulation results were compared against experimental data from existing studies, focusing on two key metrics: relative percentage error (RPE) and average relative percentage error (ARPE) [101].

3.1. Modeling the DPSTC

The collector modeled in the current simulation study is identical to that designed by Assari et al. [23]. It consists of seven identical circular tubes and seven triangular air ducts; all units are assumed to perform identically; the schematic of the collector is depicted in Figure 3.1.

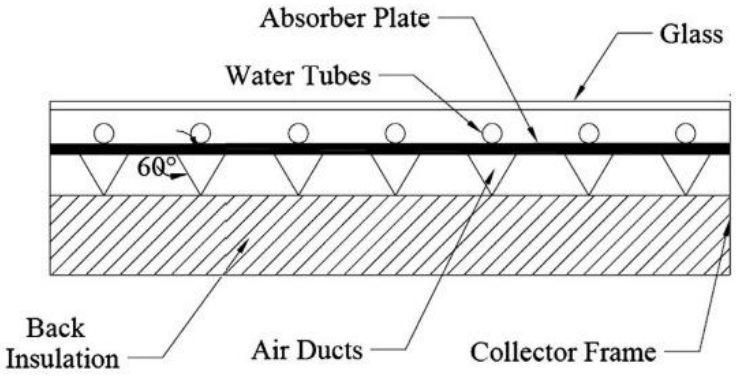

Figure 3.1. Schematic of the DPSTC used in the current study.

The design parameters of the modelled collector are presented in Table 3.1. These parameters align closely with those utilized by Assari et al. [23], ensuring accuracy and consistency in the simulation.

Table 3.1. Physical and optical constants adopted from Assari et al. [23] and used in the MATLAB simulation.

Category	Parameter/ Setting	Symbol/ Value	Parameter/ Setting	Symbol/ Value
Physical and Optical Properties	Glazing	Flout glass, 6 mm thickness	Air duct Geometry	Triangle (60°), 6 cm height
	Absorber Plate	Black-painted aluminum, 1 mm thickness	Collector dimensions	0.94m × 1.94m
	Pipe material	Zinc	Number of water pipes	7
	Pipe diameter	7 mm	Number of air ducts	7
	Collector thickness	14 cm	Preservative case	Galvanized steel
	Insulation material	Glass wool	Insulation thermal conductivity	0.039 W/(m.K)
	Bottom insulation thickness	5 cm	Absorptivity	0.93
	Absorber thermal conductivity	237 W/(m.K)	Side insulation thickness	2 cm
Boundary & Operating Conditions	Ambient Temperature	45 °C	Wind Speed	1.5 m/s
	Solar radiation	900 W/m²	Water Inlet Temperature	40- 90 °C
	Air Mass Flow Rate	0.01–0.07 kg/(s. m²)	Water Mass Flow Rate	0.02 kg/s

The procedural steps followed in the MATLAB simulations are visually represented in the flow chart illustrated in Figure 3.2.

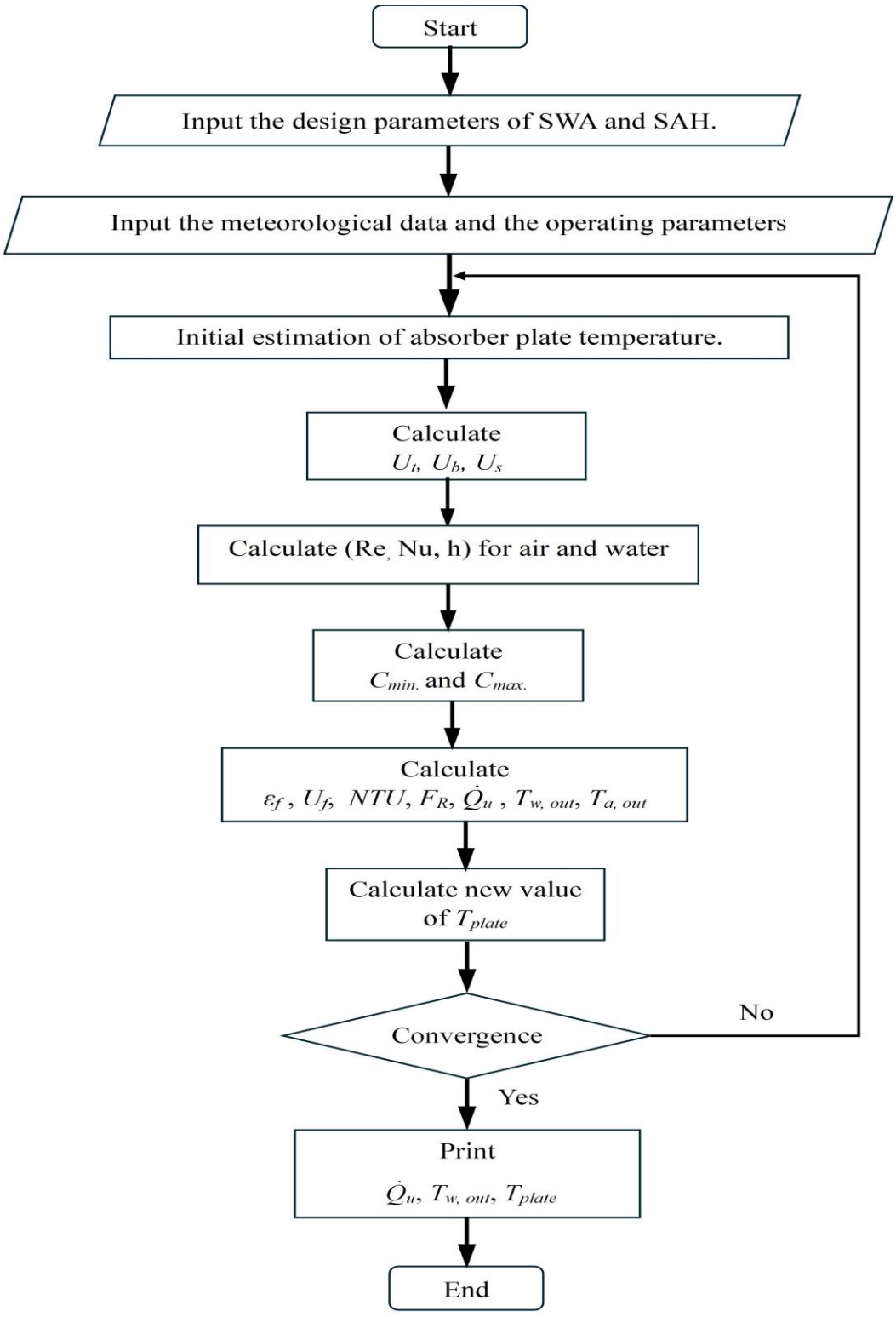

Figure 3.2. MATLAB simulation flow diagram.

At the outset of the simulation, an initial estimation of the plate temperature is required. This estimation is crucial for calculating the top heat loss coefficient (U_t). Following this, the heat loss coefficients from the back (U_b) and side (U_s) surfaces have been computed after inputting all essential parameters. The next phase involves computing the Reynolds number (Re) and the Prandtl number (Pr), which are pivotal in obtaining the Nusselt number (Nu). The Nusselt number serves as a critical factor in determining the convection heat transfer coefficient (h). Subsequently, the heat capacity rate (C) is calculated, facilitating the determination of the number of transfer units (NTU). This, in turn, allows us to assess the heat effectiveness (ε), which plays a significant role in calculating the heat removal coefficient for the second fluid (U_f). With this information, the total heat loss coefficient (U_L) can be computed, which enables us to derive the useful heat gain from both the water and air sections. Consequently, the outlet temperatures for both fluids can be accurately predicted. The simulation progresses by recalculating a new value of the mean plate temperature, which is then compared against the initial estimation. If the difference between these two temperature values falls below the threshold of (10^{-5}), convergence is deemed to have been achieved, and the simulation concludes. Conversely, if the difference exceeds this criterion, the newly calculated mean plate temperature is substituted as the new estimate, initiating a fresh iteration of the process. Once the simulation is complete, the next step involves printing the heat gains and outlet temperatures. Additionally, both the Relative Percentage Error (RPE) and the Absolute Relative Percentage Error (ARPE) were calculated. These are standard statistical tools for evaluating model performance in forecasting and regression, as described in foundational texts on applied statistics, such as Montgomery and Runger [102]. It is noteworthy that the experimental data acquired from Nematollahi et al. [28] have been incorporated within the MATLAB code to facilitate a robust comparison between the estimated and actual values, enabling the generation of the required graphical representations.

3.2. The Accuracy of Predictions

To quantify the precision of MATLAB prediction, both RPE and ARPE have been calculated. RPE is presented as a percentage and conveys the difference between observed and projected values. On the other hand, ARPE provides a summary statistic that represents the average RPE across multiple forecasts. It serves as a single value that encapsulates a model's whole accuracy. ARPE refers to the percentage difference between the observed and the predicted values. A lower ARPE corresponds to greater accuracy or precision, whereas a higher ARPE indicates larger errors. The calculated error values have been analyzed and are presented in Table 3.2.

Table 3.2. Comparison of Experimental Data [28] and Predicted Data (This Work) for Absorber Temperature, Water Outlet Temperature, and Useful Heat Gain with Corresponding RPE and ARPE.

Absorber Temperature, (°C)			Water outlet Temperature, (°C)			Useful heat absorbed, (W)		
Experimental Data [28]	**Predicted Data (This Work)**	**Relative Error (%)**	**Experimental Data**[28]	**Predicted Data (This Work)**	**Relative Error (%)**	**Experimental Data** [28]	**Predicted Data (This Work)**	**Relative Error (%)**
50.97	**60.49**	**2.94**	**46.97**	**52.82**	**12.46**	**1253.90**	**1382.44**	**10.25**

57.35	63.44	1.84	53.94	55.52	2.93	1615.60	1588.79	1.66
62.94	67.74	1.43	60.04	57.79	3.74	1730.50	1676.27	3.13
66.50	69.17	0.79	64.03	59.17	7.58	1632.62	1659.67	1.66
68.53	70.05	0.44	67.01	65.09	2.86	1441.13	1579.07	9.57
70.78	71.96	0.34	70.05	70.32	0.38	1113.48	1352.95	21.51
71.94	77.55	1.63	71.94	70.52	1.97	791.49	895.06	13.09
ARPE		1.3			4.5			8.6

The discrepancies observed in the error percentages can largely be attributed to the methodology of employing averaged data collected over a six-day observation period. Since the input parameters utilized in the MATLAB simulation were derived from the mean values of measurements taken across these days, they may not precisely represent the actual input received by the system. This averaging process introduces a notable discrepancy between the simulated and actual system performance. Additionally, certain parameters that were incorporated into the simulation-such as the thermal conductivity of the insulation materials, the thickness of the insulation, the thermal conductivity of the glass cover, as well as the absorptance and thermal conductivity characteristics of the absorber-were estimated due to their absence in the experimental study. These estimates can significantly influence the actual heat losses from the system. Consequently, this can result in variations between the predicted heat dissipation rates and the real-world heat loss experienced by the system, leading to a divergence between theoretical predictions and actual performance outcomes.

3.3. The Predicted Plate and Water Temperatures

The change in temperatures of the absorber plate and the water outlet over time is illustrated in Figure 3.3. The data presented in the figure convincingly shows that the temperatures of the absorber plate increase steadily over time as solar intensity rises. This increase in intensity not only elevates the temperature of the absorber plate but also significantly impacts the water outlet temperatures. Notably, our simulations indicate that the absorber temperature is consistently higher than what was observed experimentally. This discrepancy can be attributed to several key factors. First, the calculations for heat losses from the collector may not fully account for real-world conditions. Additionally, the gap between calculated and actual heat flow highlights essential insights, as the design and shape of the absorber plate play a vital role in influencing temperature variations. Furthermore, the interactions of heat flow between the water and air sections further illustrate the complexities involved in predicting fluid and absorber temperatures.

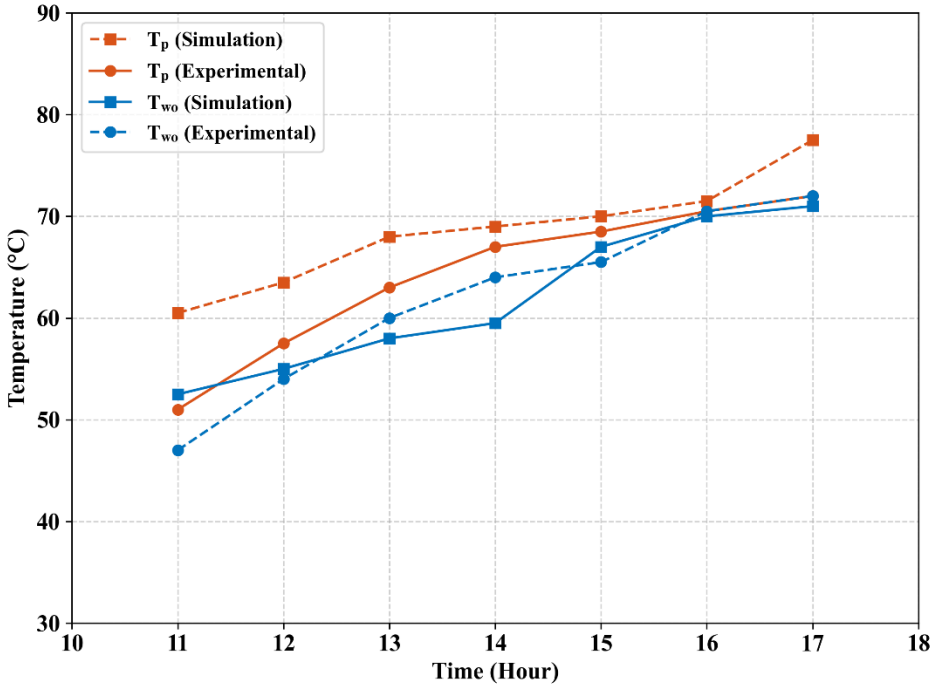

Figure 3.3. Variation of outlet water temperature (T_{wo}) and absorber plate temperature (T_P) over time: Simulation (This work) vs. Experimental data [28].

The maximum value of (RPE) for the absorbing plate and the outlet temperature of water were determined to be 2.94% and 12.46%, respectively. Meanwhile, the (ARPE) for the absorber plate and water outlet temperature was 1.3% and 4.5%, respectively. This implies that, on average, the predicted outlet water temperatures have a slightly higher average deviation compared to the absorber plate temperatures. Considering the graph's visual representation, it is evident that the temperature of the absorber plate and the water outlets exhibit similar trends and fluctuate within a similar range.

3.4. The Predicted Heat Gain

The comparison between the predicted useful energy and the experimental results is depicted in Figure 3.4. It provides valuable insights into the accuracy and precision of the energy predictions. The analysis revealed that for the useful energy, the maximum value of (RPE) is 21.51% and the value of (ARPE) is 8.6%.

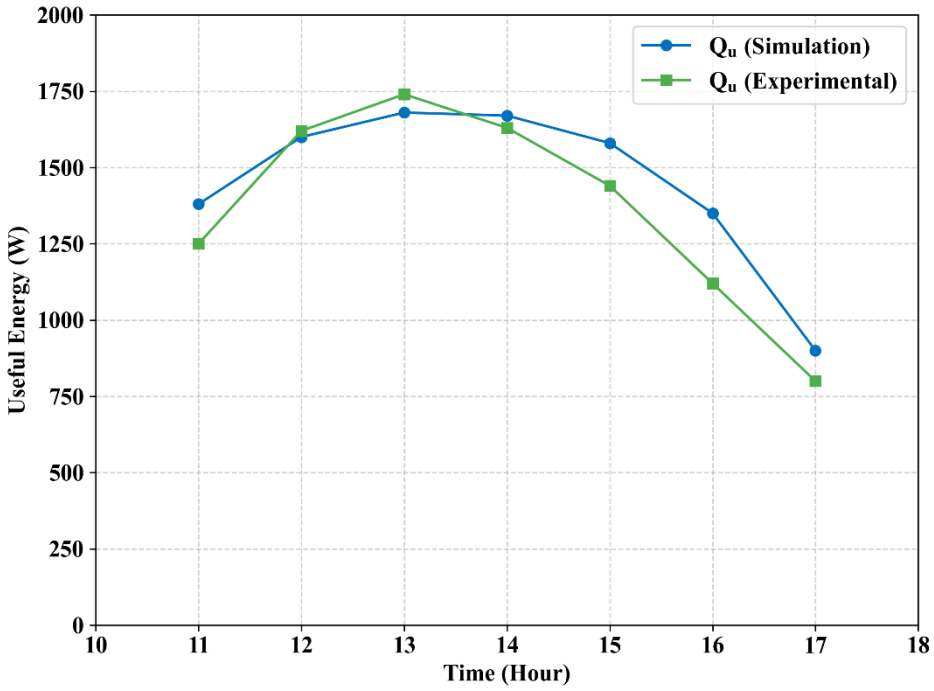

Figure 3.4. Variation of useful heat gain over time: comparison of Simulation (This work) and Experimental data [28].

The deviation between the forecasted and actual values of useful heat gain can be ascribed to the predicted effectiveness values. These values are crucial for calculating the heat removal factor and play a key role in determining heat gain. Furthermore, the actual absorber solar irradiance may differ from the calculated values in the current simulation, partly due to the estimated optical properties of the glass cover, which can influence the heat gain values. Additionally, the assessment of heat losses may not fully represent actual conditions, which could further contribute to this deviation. Accumulated errors in estimating effectiveness, absorbed solar energy, and heat losses contribute to the observed deviations. Despite these factors, there is generally a good level of convergence with experimental results.

As a summary, The DPSTC was treated as a parallel flow heat exchanger, using a formulation for effectiveness that is similar to those for other heat exchangers, differing from earlier research methods. The ε- NTU method was used to analyze the system, with RPE and ARPE metrics verifying the simulation results. The predicted outcomes closely match the experimental findings, underscoring the reliability and stability of this proposed model for predicting collector performance.

In the next chapter we developed three mathematical approaches with three MATLAB codes to further analyze the DPSTC.

4. THE OPTIMAL APPROACH OF VARIOUS ANALYSIS METHODOLOGIES OF A DUAL-PURPOSE SOLAR COLLECTOR

In this chapter, I utilized multiple analytical approaches to analyze DPSTC. Specifically, I developed the heat removal factor equation, which is crucial for calculating the effective heat gain of solar collectors. I developed three distinct MATLAB codes (C1, C2, and C3), each implementing a different mathematical model. In the first method, I derived the heat removal factor based on effectiveness values found in the existing literature. In the second method, I applied the heat removal factor specifically for the DPSTC when it operates as a single-purpose collector. In my third and novel approach, I treated the DPSTC as a parallel flow heat exchanger, using the effectiveness equation instead of the heat removal factor. To the best of my knowledge, no previous research has conducted these three distinct analyses of the DPSTC simultaneously. The simulation results demonstrated good consistency with experimental data. To assess the discrepancies between the simulated and actual results, I calculated two important metrics: the Root Mean Square Error (RMSE) and the Mean Absolute Error (MAE). It was found that C3 outperformed the other models based on the computed errors, as it exhibited the lowest error values. Consequently, code C3 can accurately predict both the water and air outlet temperatures, as well as the thermal performance of the DPSTC. This research can make a significant contribution by assisting future researchers in their studies of the DPSTC [97].

4.1. Structure of The Investigated DPSTC

The collector used in the simulation is the same as the one utilized by Saleh and Jasim [103]. The system is comprised of two distinct sections: water and air section. The air portion is a rectangular duct without fins, whereas the water section consists of risers and two primary headers (see Figure 4.1).

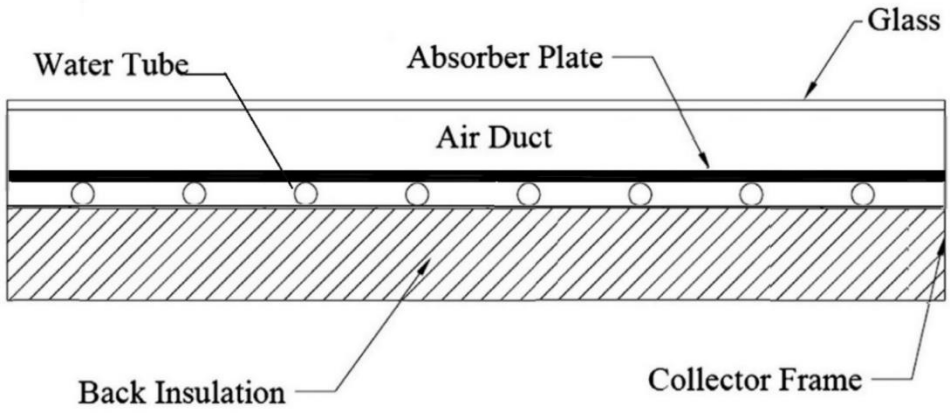

Figure 4.1. Schematic layout of the investigated DPSTC.

4.2. The Developed Numerical Simulation and Error Metrics

The novelty of the current study lies in developing the effectiveness-NTU method, a widely employed approach found in existing literature and research papers. I developed three analysis methodologies with three MATLAB codes to numerically investigate each of the identified analysis methodologies. For each code, I conducted mathematical modeling, simulations, and experimental validation. To ensure consistency and comparability, the present simulation adopted the same input parameters, both climatic and operational, as those utilized in the experimental study. The validation procedure was conducted against experimental data given in [104].

The analytical approaches chosen for each code differ from one another. The three analytical methodologies are defined as follows:

- **Methodology 1:** This approach corresponds to the conventional ε-NTU method, which is widely adopted by researchers in the analysis of DPSTC. In this method, the effectiveness equation provided earlier in Eq. (2.15) is substituted into Eq. (2.14) to calculate the heat removal factor F_R. The resulting F_R value is then utilized to evaluate the useful heat gain, as expressed in Eq. (2.7). This method's computational implementation is referred to as code C1.
- **Methodology 2 :** This method is commonly applied to the DPSTC when it is operated as a single-purpose collector (either air or water heating). In this case, the heat removal factor F_R is directly calculated using Eq. (2.8), and it is subsequently used in Eq. (2.7) to determine the useful heat gain. The computational model based on this approach is designated as code C2.
- **Methodology 3:** This novel methodology eliminates the traditional step of calculating the heat removal factor. Instead, it models DPSTC as a parallel-flow heat exchanger and directly applies the specific effectiveness relation for this configuration, as provided in Eq. (2.19), to determine the useful heat gain given by Eq. (2.7). This methodology represents the core innovation of the present study, and its computational implementation is referred to as code C3.

The simulation software is utilized to forecast the properties of a system, including the temperature of hot water and air, and the amount of usable energy absorbed by the fluid. The computational algorithm is illustrated in the flow chart displayed in Figure 4.2.

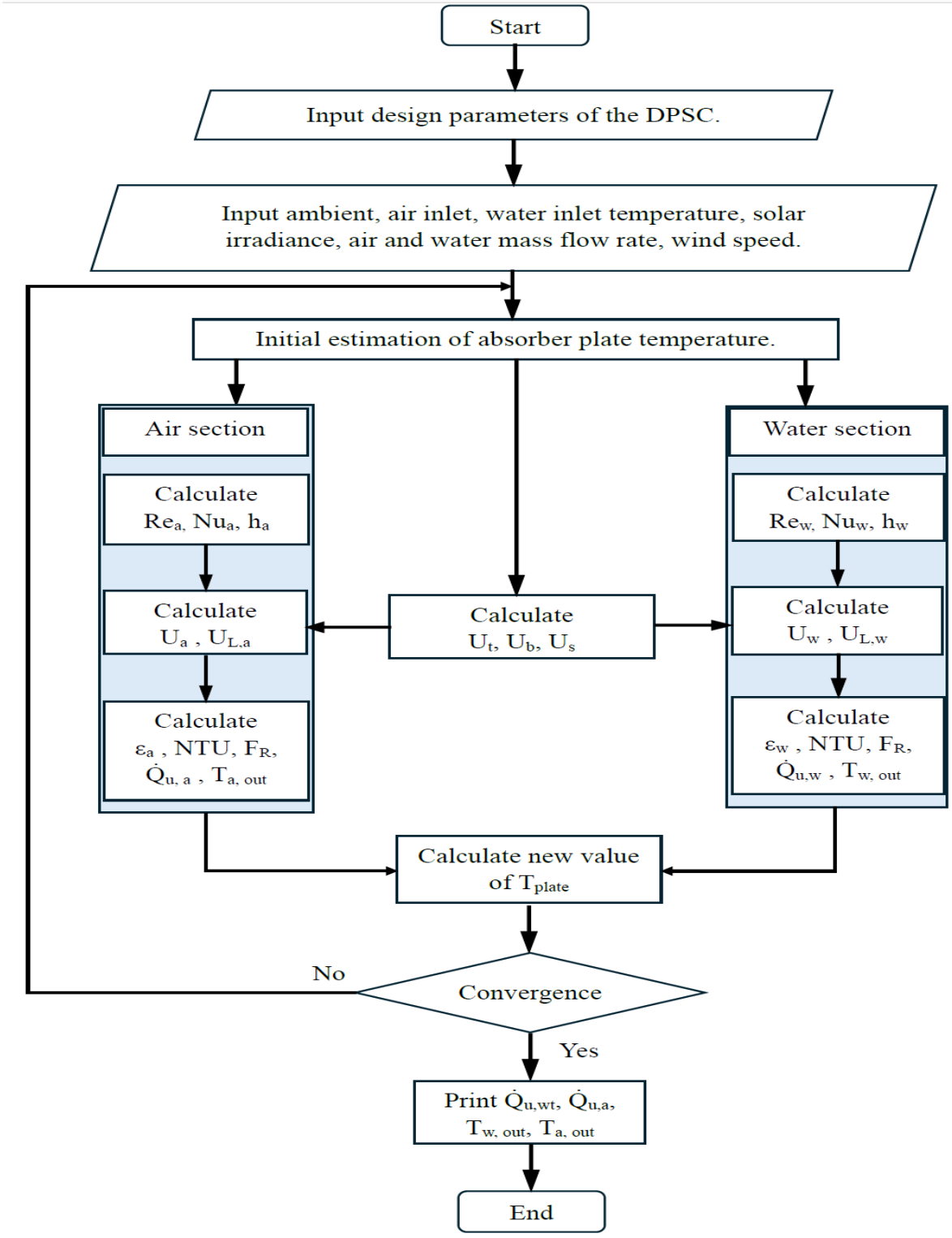

Figure 4.2. Simulation flow chart.

Two indicators have been employed Among the many tools that have been used to analyze the DPSTC performance prediction accuracy. The first is the MAE, which captures the average absolute deviation between two datasets. It is expressed mathematically as [105]:

$$MAE = \frac{1}{n}\sum_{i=1}^{n} |(T_{out,(S)} - T_{out,(E)})|. \quad (4.1)$$

The second criterion is the RMSE, a defined measure that combines the spread of individual errors. The largest values strongly dominate it due to the squaring operation. Especially in cases where prominent outliers occur, the usefulness of RMSE is questionable, and the interpretation becomes more complex [106]:

$$RMSE = \sqrt{\frac{1}{n}\sum_{i=1}^{n}(T_{out,(S)} - T_{out,(E)})^2}. \quad (4.2)$$

In this context, n, $T_{out,(S)}$, and $T_{out,(E)}$ are the total number of values that have been analyzed, the outlet fluid (water and air) temperature received from the simulation, and the temperature obtained from experiments.

4.3. The Performance of DPSTC

The air outlet temperature obtained from the three MATLAB codes C1, C2, and C3 along with the experimental results is illustrated in Figure 4.3. The predicted results and experimental data coincide extremely well during the first three hours. The variations begin around eleven o'clock and persist until five o'clock in the afternoon.

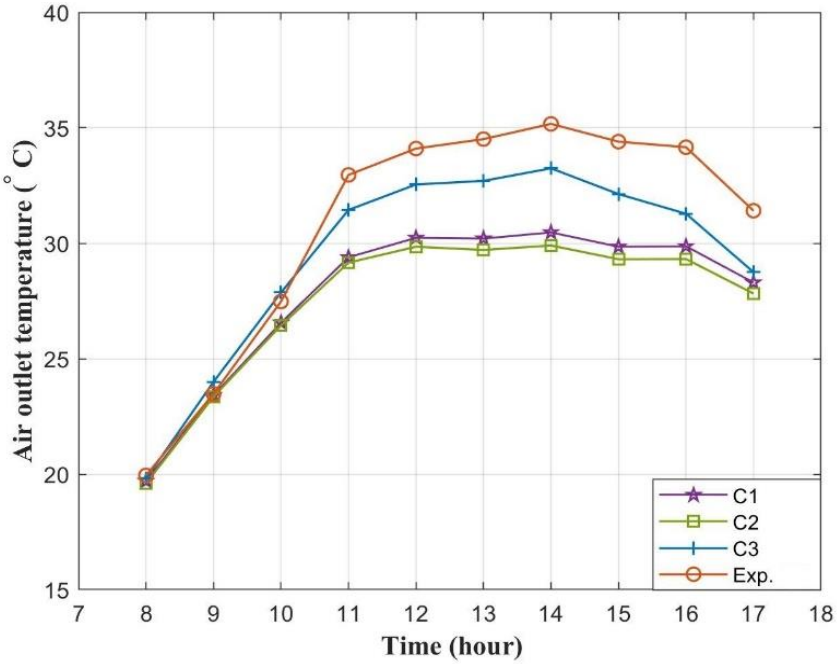

Figure 4.3. The variation of air outlet temperature with time for the three codes.

It is worth mentioning that the gap between our ingenious code C3 and experimental findings is only one and a half to three degrees Celsius, while it exceeds five degrees Celsius for both C1 and C2. However, the error values between the output numerical results and the measured data are then calculated. The RMSE values for C1, C2, and C3 are 3.4%, 3.8%, and 1.8%, respectively. The MAE values for C1, C2, and C3 were 3%, 3.3%, and 1.5%, respectively. It is crucial to emphasize that the RMSE and MAE values of our mathematical model C3 reveal superior temperature prediction competencies compared to mathematical models C1 and C2. Figure 4.4 plainly shows the tremendous capability of our innovative and proposed mathematical model C3 for forecasting the water outlet temperature.

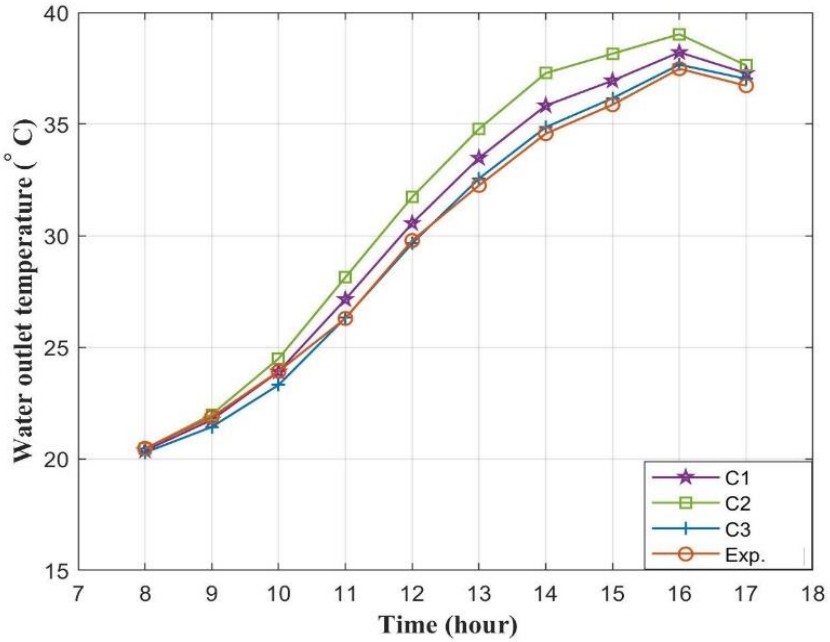

Figure 4.4. The variation of water outlet temperature with time for the three codes.

It is obvious that the predicted values of the outlet water temperature obtained from the simulation codes highly reflect the experimental results. While the predicted temperatures are relatively consistent with the actual temperature, the temperature yielded from code C3 remains superior due to the relatively lower error values compared to the remaining codes C1 and C2. Nevertheless, the RMSE values for C1, C2, and C3 are 0.8%, 1.7%, and 0.3%, respectively. The MAE values for C1, C2, and C3 were 0.7%, 1.4%, and 0.3%, respectively.

As a summary, the mathematical equation of the heat removal factor F_R was improved in this chapter. Three mathematical codes, C1, C2, and C3, each with its theoretical technique, were numerically tested using the MATLAB simulation tool. Among the tested codes, code C3, which comprises a novel mathematical technique, can precisely predict the water and air outlet temperature and the thermal performance of the DPSTC as well. Code C3 outperformed the other models based on the computed erroneous because it has the lowest error values compared to the other models. This

can be a significant contribution that can assist future researchers in their studies for DPSTC. This study contributes to the ongoing discourse on solar collector analysis by offering insights into the benefits and limitations of employing multiple methods in performance evaluation. The key characteristics, limitations, and performance outcomes of the three analytical methodologies investigated in this study are summarized in Table 4.1.

Table 4.1. Summary and Comparison of the Three Analytical Methodologies.

Comparison Criteria	**Methodology 1 (Conventional ε-NTU)**	**Methodology 2 (Single-Purpose)**	**Methodology 3 (Novel approach)**
Description	A widely used approach based ε-NTU method.	A simplified approach that treats DPSTC as if it were operating in a single mode.	A novel approach that models the DPSTC specifically as a parallel flow heat exchanger.
Core Principle	Calculates the heat removal factor F_R as a function of the collector's general effectiveness (ε).	Calculates F_R using the direct formula for a single-purpose collector.	Bypasses F_R and directly uses the effectiveness equation to find useful heat gain.
Key Equations Used	ε_f (Eq. 2.15) → F_R (Eq. 2.14) → $Q_{u,f}$ (Eq. 2.7)	F_R (Eq. 2.8) → $Q_{u,f}$ (Eq. 2.7)	ε_f (Eq. 2.19) → $Q_{u,f}$ (replaces F_R term in Eq. 2.7)
Advantages	Established and familiar method.	Mathematically simple for single-mode analysis.	Theoretically more accurate for DPSTC's dual-channel, parallel flow geometry.
Limitations	The general effectiveness equation may not perfectly capture the specific physics of a DPSTC.	Inaccurate for a dual-purpose system with simultaneous air and water heating.	As a novel approach, it requires rigorous validation, as performed in this study.
Predictive Accuracy			
Air Outlet Temp. Errors	RMSE: 3.4% MAE: 3.0%	RMSE: 3.8% MAE: 3.3%	**RMSE: 1.8%** **MAE: 1.5%**
Water Outlet Temp. Errors	RMSE: 0.8% MAE: 0.7%	RMSE: 1.7% MAE: 1.4%	**RMSE: 0.3%** **MAE: 0.3%**
Overall Assessment	Moderate predictive accuracy.	Lowest predictive accuracy.	**Highest predictive accuracy (Optimal)**

In the next chapter, we utilized ANSYS Fluent software to model DPSTC, investigating various liquids as alternatives to water under different operating conditions.

5. NUMERICAL INVESTIGATION OF A DUAL- PURPOSE SOLAR COLLECTOR USING DIFFERENT LIQUIDS

In this chapter, I investigated the influence of various heat transfer fluids on the thermal behavior of DPSTC using ANSYS Fluent. I observed a significant lack of Computational Fluid Dynamics (CFD) studies focused on this kind of collector, which makes this aspect a key innovation in my work. I utilized three different working fluids: water, Therminol VP-1, and Dowtherm A. My examination of oil-based liquids, in addition to conventional water, is particularly relevant given that water is rendered ineffective in extreme hot and cold climate conditions — freezing at 0 °C and boiling at 100 °C under atmospheric pressure. Furthermore, the lack of research exploring the use of these alternative fluids in DPSTC adds another layer of innovation to my study [107].

5.1. The Number of Investigated Cases

Throughout the simulation, I analyzed how various airflow rates impacted exit temperatures, heat gains, and the thermal efficiency of the DPSTC. The input boundary conditions employed in the simulation are detailed in Table 5.1. The liquid domain maintains fixed inlet conditions of 40 °C with a flow rate of 0.02 kg/s. In the air domain, the inlet temperature is set to 45 °C, with variable mass flow rates.

Table 5.1. Input parameters and their corresponding values used in the numerical simulation, as reported in Ref. [23].

Input parameter	Range
Solar irradiance	900 W/m^2
Inlet air temperature	45 °C
Inlet liquid temperature	40 °C
Air flow rate	0.02-0.1 kg/s
Liquid flow rate	0.02 kg/s

I treated each liquid as a unique case, conducting five simulations at varying air flow rates ranging from 0.02 to 0.1 kg/s, increasing in increments of 0.02. As a result, a total of 15 simulations were conducted throughout this study.

5.2. Thermophysical Properties of Working Fluids

The present study considers Therminol VP-1 and Dowtherm A working fluids. Therminol VP-1 is an artificial heat transfer liquid characterized by its extraordinary thermal stability and low viscosity to guarantee effective, trustworthy, and regular performance across an optimum operational temperature range from 12 °C to 400 °C. It offers excellent thermal stability among natural HTFs [108]. The thermal features of these HTFs vary depending on the temperature. The thermo-physical features of Therminol VP-1 can be obtained from the following correlations [109], which is specifically designed for the range of (285.15 K ≤ T ≤ 698.15 K):

$$C_p = \begin{cases} 2.125 \cdot 10^3 - 11.017T + 0.049862T^2 \\ -7.7663 \cdot 10^{-5}T^3 + 4.394 \cdot 10^{-8}T^4, \end{cases} \quad (5.1)$$

$$\rho = \begin{cases} 1.4386 \cdot 10^3 - 1.8711T \\ +2.737 \cdot 10^{-3}T^2 - 2.3793 \cdot 10^{-6}T^3, \end{cases} \quad (5.2)$$

$$k = \begin{cases} 0.14644 + 2.0353 \cdot 10^{-5}T \\ -1.9367 \cdot 10^{-7}T^2 + 1.0614 \cdot 10^{-11}T^3, \end{cases} \quad (5.3)$$

$$\mu = \begin{cases} 3.661 \cdot 10^2 - 3.0154T \\ +8.3409 \cdot 10^{-3}T^2 - 7.723 \cdot 10^{-6}T^3, \end{cases} \quad (5.4)$$

where, C_p, ρ, k, and μ referred to the specific heat (J/kg·K), density (kg/m3), thermal conductivity (W/m·K), and density (mPa·s), respectively.

The correlations used to calculate the thermo-physical properties of Dowtherm A in the range of temperatures (288.15 K≤T≤678.15 K) are given as follows [109]:

$$C_p = 911.4 + 2.011T + 9.368 \cdot 10^{-4}T^2, \quad (5.5)$$

$$\rho = 1190 - 0.2243T - 7.866 \cdot 10^{-4}T^2, \quad (5.6)$$

$$k = 0.1856 - 1.6 \cdot 10^{-4}T, \quad (5.7)$$

$$\mu = 10^{5.274}T^{-3.247} + 10^{27.75}T^{-12.3}, \quad (5.8)$$

In this study, a meticulously developed MATLAB code is employed to compute the thermo-physical characteristics related to Therminol VP-1 and Dowtherm A liquids based on the above correlations in the range of temperatures 20-65°C. The average value for each property is then imported into ANSYS Fluent software. The properties of all the materials (solids and fluids) utilized in the simulation are given in Table 5.2.

Table 5.2. Thermophysical properties of the material and working fluids are utilized in the simulation.

Material	C_p, (J/kg·K)	ρ, (kg/m^3)	k (W/m·K),	μ, (Pa·s)
Therminol VP-1	1609.73	1046.000	0.1339	0.0027
Dowtherm A	1698.53	1024.200	0.1315	0.0016
Aluminum	871.00	2719.000	202.4000	-
Zinc	389.00	7140.000	116.0000	-
Water	4182.00	998.200	0.6000	1.0030·10-3
Galvanized Steel	470.00	7850.000	52.0000	-
Air	1006.43	1.2250	0.0242	1.7894·10-5

5.3. The Effect of Airflow on The Exit Temperature of DPSTC

An analysis of how airflow rate affects the exit temperature of each examining liquid is shown in Figure 5.1. The average temperature at the outlet is 45.32 °C when the inflow water temperature is 40 °C. In contrast, when utilizing Therminol VP-1 at the same inlet temperature, the average exit temperature increases to 51.82 °C. Similarly, Dowtherm's average outlet temperature is slightly lower at 51.53 °C.

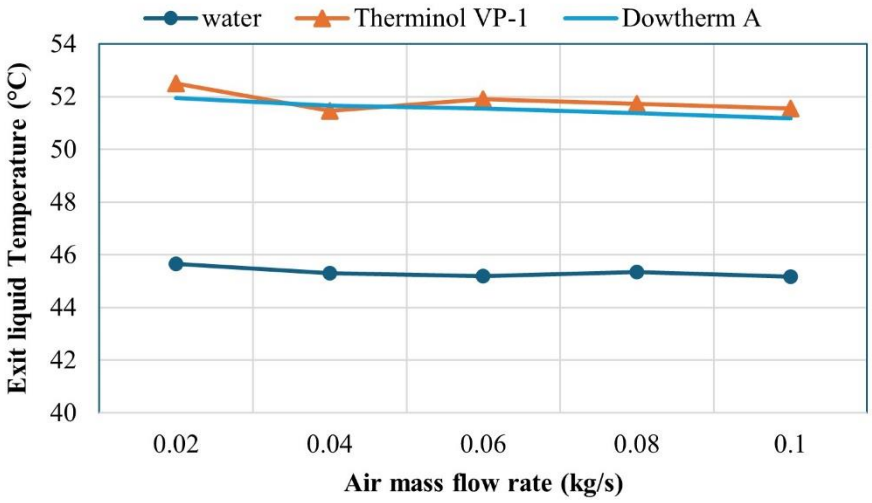

Figure 5.1. The variation of exit liquid temperature with air flow rates.

It is observed that increasing the air flow rates has minimal effect on the exit temperatures of the studied liquids since the input air temperature is significantly greater than the liquid temperature, thereby, increasing airflow may not a substantial impact on reducing the exit liquid temperature. However, there is still a notable increase of 17.5%, 29.55%, and 28.83% in the outlet temperatures of the water, Therminol VP-1, and Dowtherm A, respectively, compared to the inlet liquid temperature of 40 °C. Notably, Therminol and Dowtherm demonstrate higher exit temperatures than water, with an average enhancement of 14.33% and 13.7%, respectively. The maximum outlet liquid temperature occurs at an airflow rate of 0.02 kg/s, while the inlet liquid temperature is 40 °C. These temperatures are 52.5 °C, 52 °C, and 45.6 °C for Therminol VP-1, Dowtherm A, and water, respectively.

The variation in airflow rate slightly impacts the outlet air temperature when the three liquids are utilized, as shown in Figure 5.2. Increasing airflow decreases the residence time of the air in contact with the duct surface, thereby reducing the duration available for thermal exchange processes. This expedited airflow results in a lower outlet air temperature. The outlet air temperature when using Therminol is greater than that of water and Dowtherm. The average increase in exit air temperature is 6.67% for Therminol and 6% for Dowtherm relative to the case using water.

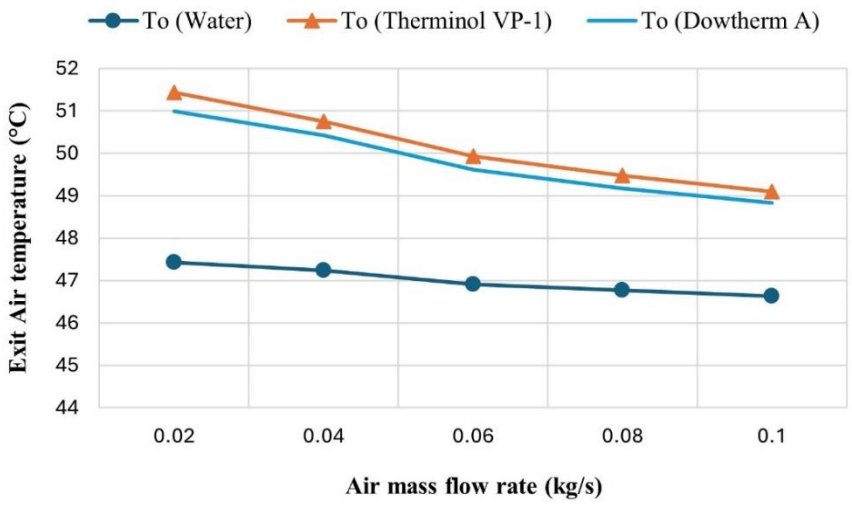

Figure 5.2. The variance of exit air temperature with air flow rate

The maximum outlet air temperatures recorded are 51.4 °C, 51 °C, and 47.4 °C when using Therminol VP-1, Dowtherm A, and water, respectively. These temperatures occur at an airflow of 0.02 kg/s, with inlet air and liquid temperatures set at 45 °C and 40 °C, respectively. The high incident heat flux with the large surface area of the air duct and the low airflow allow the air temperature to rise significantly. The temperature contours for all domains (liquid tube, air duct, and absorber plate) of the DPSTC are illustrated in Figure 5.3 based on an air and water flow rate of 0.02 kg/s.

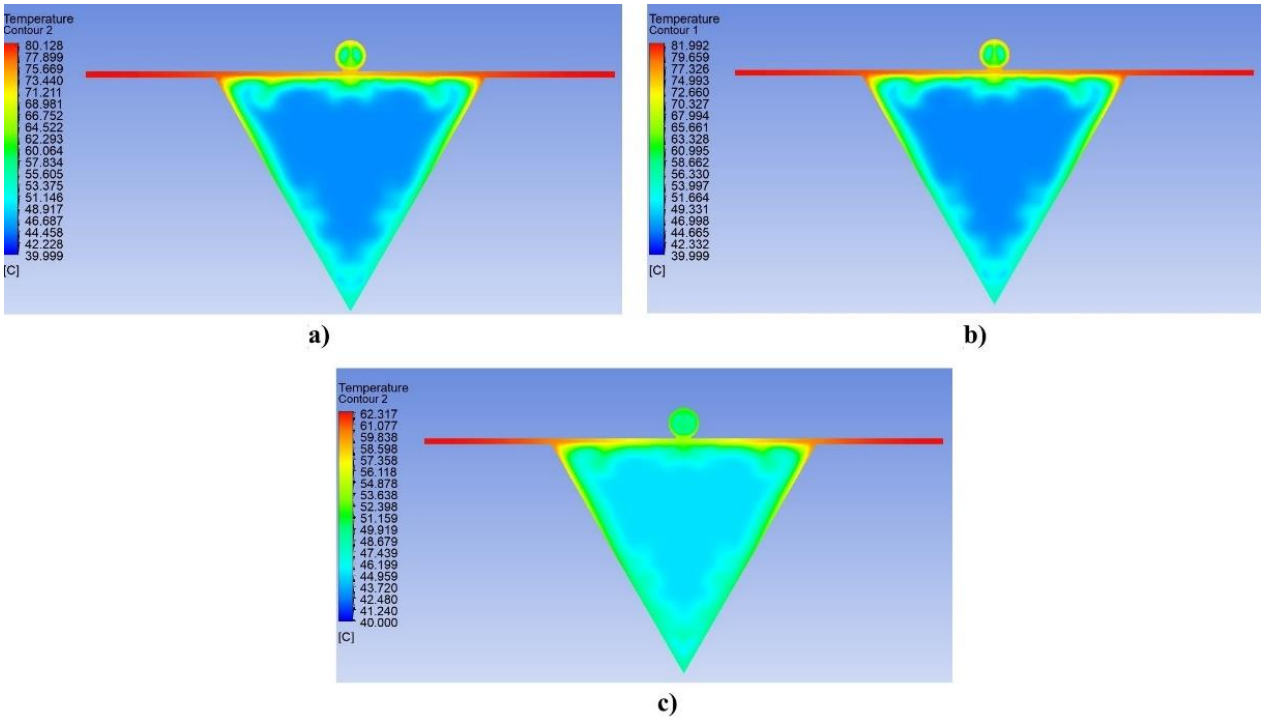

Figure 5.3. Temperature contour of all domains of the DPSTC when using three liquids: a) Dowtherm A, b) Therminol VP-1, and c) Water.

Therminol and Dowtherm exhibit similar temperature contours, as shown in Figures 5.3 a and b, ranging between 40 °C and 82 °C. Both liquids have nearly identical thermal conductivity and heat capacity, making distinguishing between their temperature contours difficult. The absorber plate reaches higher temperatures with Therminol and Dowtherm compared to water, and it continues to exhibit the highest temperature values for both the exit liquid and air. Conversely, the temperature contour of water varies between 40 °C and 62 °C. Additionally, water demonstrates more homogeneous behavior than Therminol and Dowtherm, likely attributed to its higher thermal conductivity and heat capacity, as depicted in Figure 5.3 c.

5.4. The Effect of Airflow on The Heat Gain of DPSTC

As expected, the liquid heat gain remains relatively constant because the heat flux is constant, which means the heat transfer rate is stable. This stability arises from the consistent heat transfer coefficient and driving temperature difference. Moreover, the constant flow rate of the liquid ensures a uniform flow and, thereby, a stable convective heat transfer, which helps maintain a constant heat gain. Keeping the inlet liquid temperature constant ensures the heated pipe surface, which remains steady. In contrast, variations in airflow disrupt this stability, thereby increasing air heat gain with airflow rate. This can enhance the convection heat exchange between the air and the duct, as it is demonstrated in Figure 5.4.

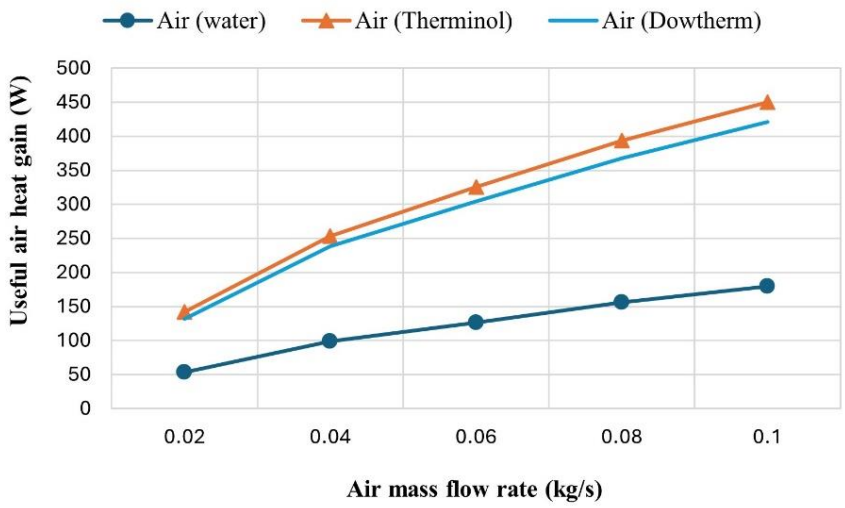

Figure 5.4. The variance of useful air heat gain with air flow rates.

As it is depicted in Figure 5.4, Therminol VP-1 and Dowtherm provide advantages over water in terms of air heat delivery, as they exhibit lower heat capacities than water.

This characteristic allows water to absorb the incident heat on the absorber more rapidly than the other two liquids, leaving less time for the air to heat up when using water. This difference is evident when comparing liquid heat delivery, illustrated in Figure 5.5, where water shows the highest heat delivery values compared to Therminol and Dowtherm. Although water outperforms Therminol and

Dowtherm A in heat gain from the liquid side of the DPSTC, the total heat gain, representing the combined air and liquid heat gains for Therminol and Dowtherm, exceeds that of water.

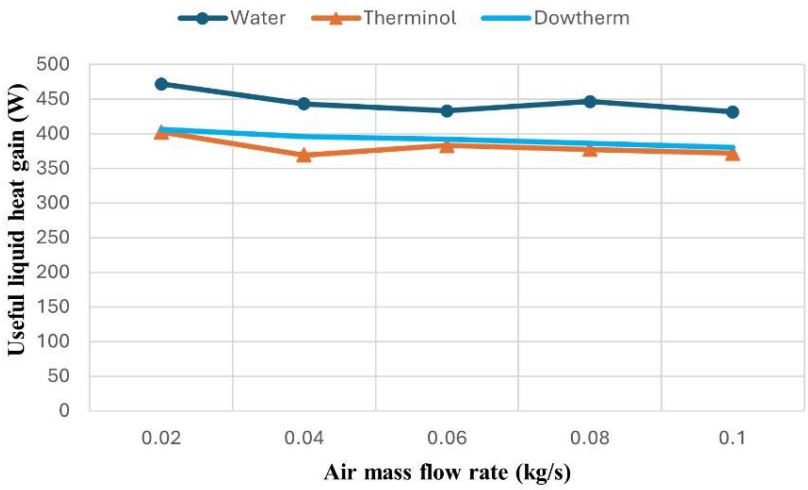

Figure 5.5. The variance of liquid useful heat gain with air flow rates

5.5. The Effect of Airflow on The Efficiency of DPSTC

The efficiencies of the liquid side, air side, and combined collector are presented in Figures 5.6-5.8, respectively. Efficiency is the proportion of beneficial heat obtained to the entire amount of irradiance hitting the absorber. It is evident from Figures 5.6 and 5.7 that the efficiencies of the air and liquid sides of the DPSTC mirror the trends observed in useful gain since the incident radiation remains constant. For all values of the air flow rate, the liquid side efficacy when using water is greater than that of the other liquids.

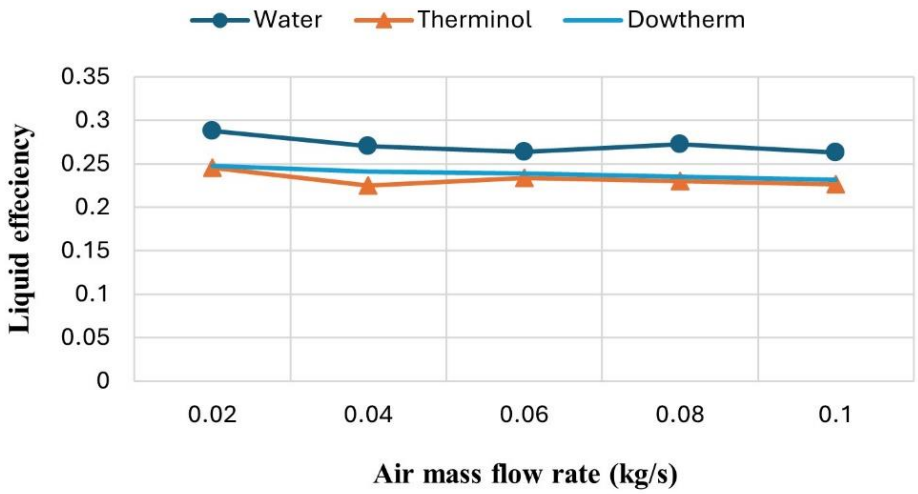

Figure 5.6 The efficiency of the liquid side of the DPSTC with an air flow rate

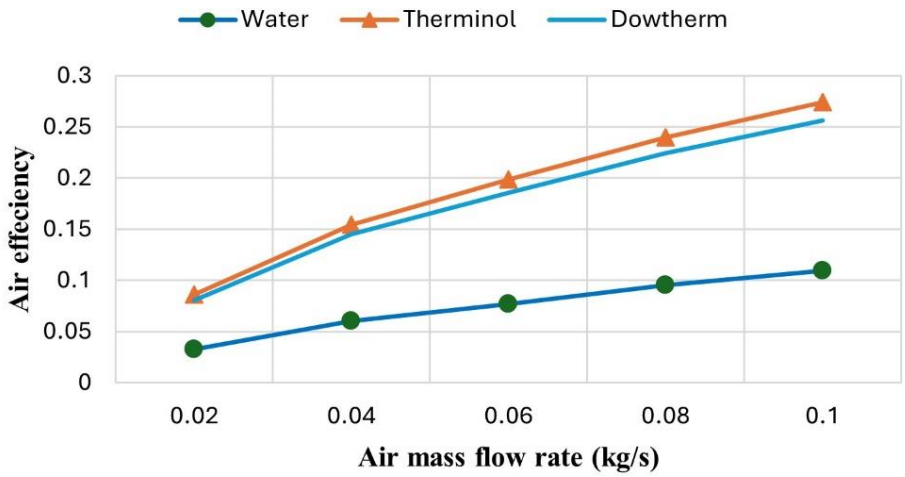

Figure 5.7. The efficiency of the air side of the DPSTC with an air flow rate.

The maximum air efficiency of Therminol VP-1, Dowtherm A, and water is 27.4%, 25.6%, and 10.9%, respectively, which corresponds to the highest air flow of 0.1 kg/s. These maximum air efficiency values are of significant importance as they directly impact the total thermal efficiency of the DPSTC (see Figure 5.8), which stands for the sum of the air and liquid sides' efficiencies.

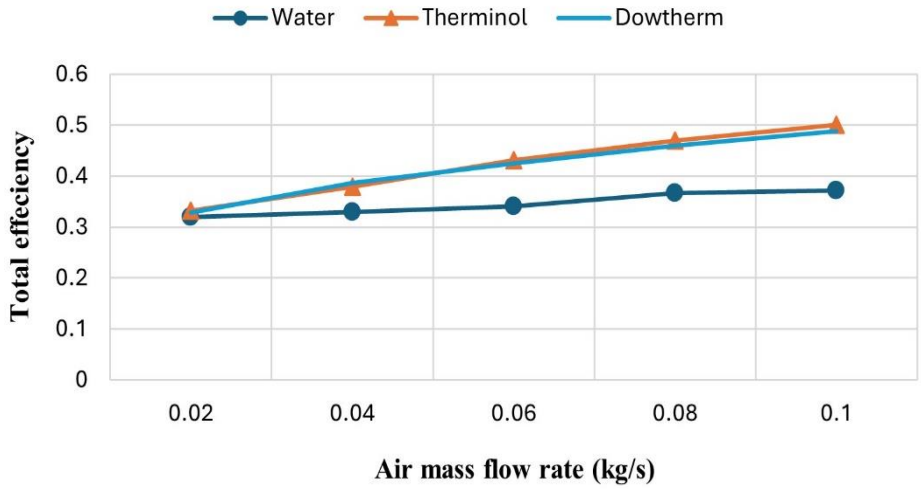

Figure 5.8. Total efficiency of the DPSTC with an air flow rate.

The rise in air efficacy results from the higher air flow rate, which drops the temperature difference between the absorbent surface and the air. That minimizes the heat losses and maximizes the heat absorbed by the air.

The total efficiency of the DPSTC is directly influenced by the increased airflow rate, particularly for both Therminol and Dowtherm liquids. Both liquids show a consistent increase in efficiency as the airflow rate rises, with the maximum efficiency recorded at 0.1 kg/s. This highlights the significant role of the airflow rate in the system's performance, as it influences the efficiency of both liquids.

As a summary, and based on the aforementioned findings, using Therminol and Dowtherm as HTF instead of water can efficiently ameliorate the gross thermal effectiveness of the DPSTC.

It is crucial to emphasize that although water offers the best temperature distribution, Therminol and Dowtherm have higher temperature values of the absorber plate, outlet air, and liquid. More investigations can be carried out by varying the other operating parameters, and their results can be discussed to confirm the robustness of these kinds of alternative liquids for use in solar thermal systems. Future recommended work includes conducting CFD simulations with varying liquid flow rates and a range of inlet fluid temperatures.

In the next chapter, we investigated the use of nanofluids as alternatives to oil-based liquids to evaluate the performance of the DPSTC using the same model outlined previously. We also tested the collector under different liquid flow rates along with varying air flow rates.

6. EVALUATION OF A DUAL-PURPOSE SOLAR COLLECTOR USING MONO-NANOFLUIDS: A CFD SIMULATION

In this chapter, I analyzed the performance of DPSTC using computational fluid dynamics simulations in ANSYS Fluent. For this purpose, I employing nano fluids, specifically CuO-H_2O and MWCNT-H_2O, at a volume concentration of 0.5%. I selected these nanofluids based on an extensive literature review, which showed that these two nanofluids are among the most frequently used in solar collectors due to their favorable properties that can significantly enhance the overall thermal performance of solar systems. Consequently, I examined both nanofluids alongside water and compared their thermal performance to that of water. To the best of my knowledge, no prior research specifically investigating the use of these nanofluids in DPSTCs, which highlights the novelty of my work. In this numerical investigation, I modeled the same system fabricated by Assari et al. [23]. The input boundary conditions employed in the simulation are consistent with those outlined in Table 5.1. To validate the CFD simulation results, I compared them with experimental data presented in Chapter 2. Furthermore, my investigation consisted of two distinct phases of simulation. In the first phase, I focused on varying air flow rates while maintaining all other parameters constant. In the second phase, I systematically varied the liquid flow rate whereas the other parameters were held constant. In both phases, I evaluated the effects of the two nanofluids on the outlet temperatures of the air and liquid streams from the DPSTC. Additionally, I assessed how varying flow rates influenced the heat gains and overall thermal efficiency [54].

6.1. Thermophysical Properties of Nanofluids

Various researchers [62] have proposed methods for calculating the thermophysical properties of nanofluids. These properties depend on the thermophysical characteristics of the base fluid, the nanoparticles, and their concentration. The equations below present the most widely used correlations for density, specific heat, viscosity, and thermal conductivity of nanofluid:

$$\rho_{nf} = (1-\varphi)\rho_{bf} + \varphi\rho_{np}\,, \tag{6.1}$$

$$\left(C_p\right)_{nf} = \frac{(1-\emptyset)\left(\rho C_p\right)_{bf} + \emptyset\left(\rho C_p\right)_p}{\rho_{nf}}, \tag{6.2}$$

$$\mu_{nf} = (1 + 2.5\emptyset + 6.5)\mu_f\,, \tag{6.3}$$

$$k_{nf} = \left[\frac{K_p + 2K_{bf} - 2\emptyset\left(K_{bf} - K_p\right)}{K_p + 2K_{bf} + \emptyset\left(K_{bf} - K_p\right)}\right] k_{bf}\,, \tag{6.4}$$

where ρ, C_p, μ, and k represent the density, specific heat capacity, dynamic viscosity, and thermal conductivity, respectively. The subscripts nf, bf, and p denote the nanofluid, base fluid, nanoparticle, respectively. The particle volume fraction refers to by φ.

In the present study, two different types of nanoparticles, CuO and MWCNT, were used to create two distinct nanofluids with water as the base fluid. The volume concentrations of these nanoparticles were set at 0.5%. For this numerical analysis, specific nanoparticle dimensions, such as diameter in nanometers, were not included as input parameters. Instead, the physical model utilizes the bulk thermophysical characteristics of the nanoparticle materials, which serve as input for well-established empirical correlations. The main objective of this research is to assess the overall thermal performance trends of the resulting nanofluids rather than delving into particle-scale phenomena. Since this is a theoretical and numerical study, we assume the nanofluid's stability. The correlations used to determine the properties of the nanofluid are predicated on the assumption of an ideal, stable, and homogeneous suspension, in which the nanoparticles are evenly distributed without any clustering or settling.

To determine the thermophysical properties of the nanofluids, I developed a MATLAB program that enables the user to input a range of parameters, including all the properties outlined in Table 6.1, and the volume concentration of the selected nanoparticles. These inputs are then seamlessly substituted into the appropriate equations to compute the properties of the nanofluid. The calculated properties are carefully stored in a dedicated MATLAB workspace, ensuring they are readily available to serve as inputs for the ANSYS simulation during the definition of materials in the cell zone conditions [54].

Table 6.1. The thermo-physical properties of the base fluid and nanoparticles.

Physical properties	Water [72]	MWCNT [68]	CuO [62]
$\boldsymbol{\rho}$ (kg/m^3)	998.2	2100	6000
$\boldsymbol{k}$ (W/(m. K))	0.613	3000	33
$\boldsymbol{C_p}$ (J/(kg. K))	4182	519	551
$\boldsymbol{\mu}$ (mPa·s)	0.001	-	-

6.2. The Impact of Airflow on The Exit Temperatures of DPSTC

The effect of increasing airflow on the outlet air temperature when using different liquids is illustrated in Figure 6.1. For all cases, the outlet air temperature exceeds the inlet air temperature. Increasing the air flow rate has a minimal effect on the outlet air temperature when utilizing 0.5% CuO-H_2O and 0.5% MWCNT-H_2O. In contracts, with water, increasing the airflow rate lowers the outlet air temperature from 47.4 °C to 46.6 °C. For both nanofluids, the increase in outlet air temperature is about 1 °C. However, when using water, the temperature increase is approximately 2.5 °C at an airflow rate of 0.02 kg/s and 1.6 °C at an airflow rate of 0.1 kg/s. This difference can be attributed to water's higher specific heat capacity than the tested nanofluids.

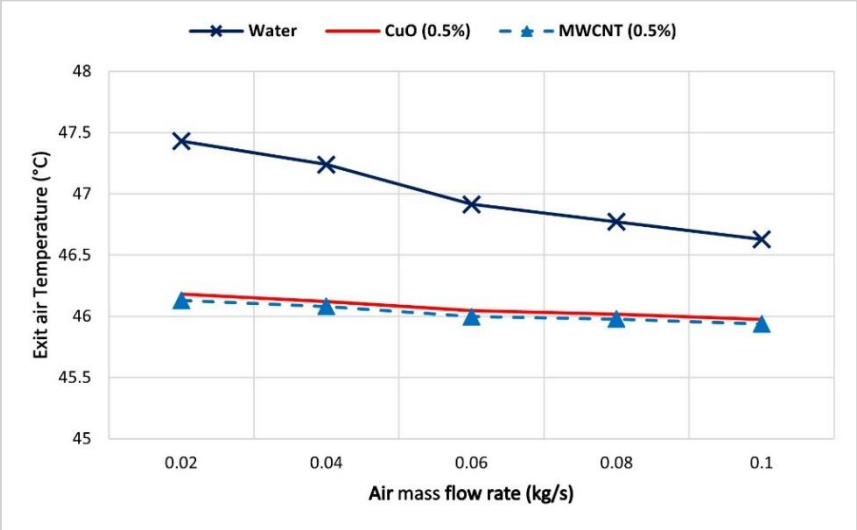

Figure 6.1. The effect of airflow rate on the exit air temperature for various HTLs.

In the liquid section of the DPSTC, Figure 6.2 illustrates the relationship between the outlet liquid temperature and the increasing airflow rate. With an inlet liquid temperature of 40 °C, a significant rise in outlet liquid temperature is observed across all cases. The 0.5% CuO-H_2O and 0.5% MWCNT-H_2O nanofluids achieve the highest outlet temperature, approximately 10 °C higher than the inlet temperature, representing a 25% enhancement. In contrast, water shows only a 13% increase in outlet liquid temperature. This difference may be attributed to the enhanced thermal conductivity of the nanofluids, along with the laminar flow, which increases the time available for the liquids to be heated.

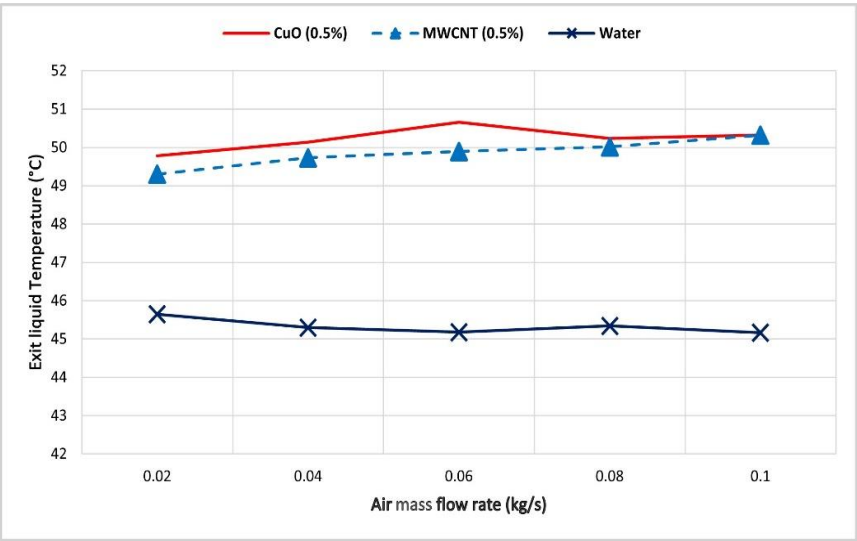

Figure 6.2. The effect of airflow rate on the exit liquid temperature for various HTLs.

The increase in air mass flow rate results in a temperature drop of approximately 0.5°C at the liquid outlet when water is used. Furthermore, it is essential to highlight that CuO nanoparticles exhibit superior performance compared to MWCNT in terms of outlet air and liquid temperatures, owing to their greater heat capacity.

The temperature contours across all domains - liquid tube, air duct, and absorber plate - of the DPSTC are presented in Figure 6.3 corresponding to an air flow rate of 0.06 kg/s. It shows the temperature contour at a plane located at the DPSTC's exit. While the temperature distributions in the liquid sections of both cases presented in Figures 6a and 6b are similar, the CuO-H_2O nanofluid demonstrates superior performance on average compared to the MWCNT-H_2O. The lower flow rate, which results in laminar flow, leads to less mixing and weaker heat diffusion throughout the liquid pipe, particularly when using water. In the air section, as depicted in Figure 6.3c , the air inside the duct exhibits a uniform temperature distribution compared to Figures 6.3a and 6.3b, indicating better heat penetration.

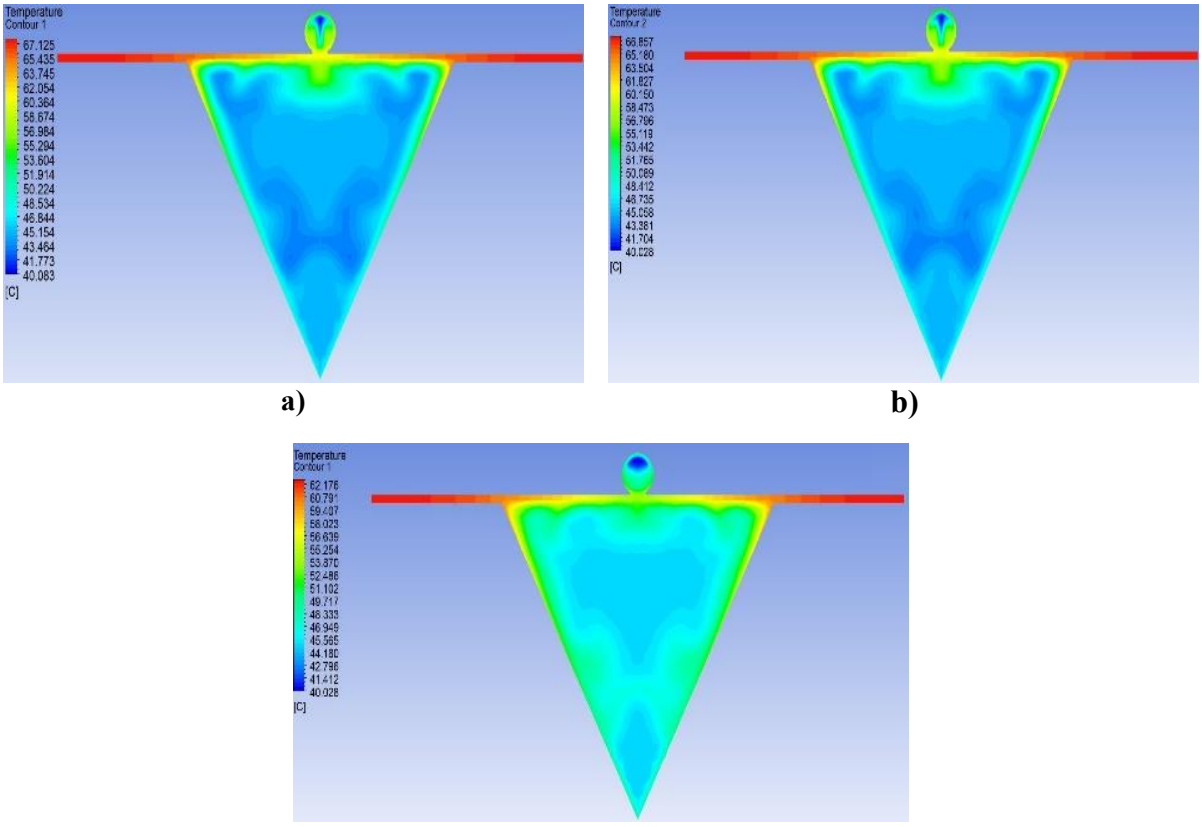

Figure 6.3. Temperature contour of the DPSTC under steady-state conditions using different working fluids, a) CuO-H_2O, b) MWCNT-H_2O, and c) Water.

6.3. The Impact of Airflow on The Performance of DPSTC

The overall performance of DPSTC can be assessed by calculating the total heat gain from the collector's air and liquid components. The total useful heat gain consistently rises for all tested fluids as a higher air flow rate enhances the convective heat transfer, leading to more effective heat absorption. Using CuO at a 0.5% concentration, followed by MWCNT at the same concentration, provides advantages over other liquids circulating in the collector, particularly in terms of total heat

gain, as illustrated in Figure 6.4. An increase in airflow is correlated with an increase in the total heat gain of the DPSTC. The maximum recorded values of heat gain rate are 965.939 W for 0.5% vol MWCNT and 970.168 W for 0.5% vol CuO. In contrast, the minimum recorded values are 801.994 W and 843.816 W for the same nanofluids. Both 0.5% vol MWCNT and 0.5% vol CuO showed a maximum enhancement percentage of 58.18% and 58.87%, respectively, compared to using water, which resulted in a lower heat gain.

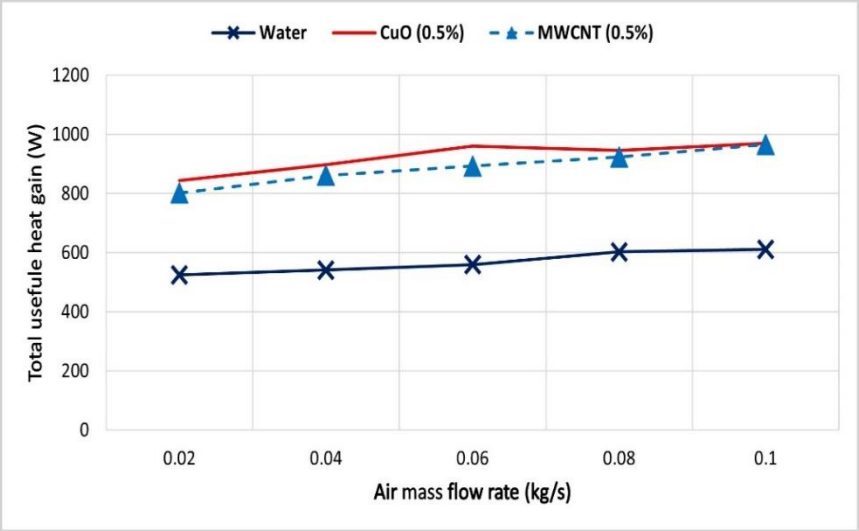

Figure 6.4. Variation of useful heat gain with airflow rate for various HTLs.

The overall efficiency of the DPSTC is significantly affected by the increase in air flow rate, especially when using 0.5% CuO and 0.5% MWCNT nanofluids (see Figure 6.5). The average efficiency enhancement is 62.77% for the 0.5% CuO nanofluid and 56.56% for the 0.5% MWCNT nanofluid, compared to water.

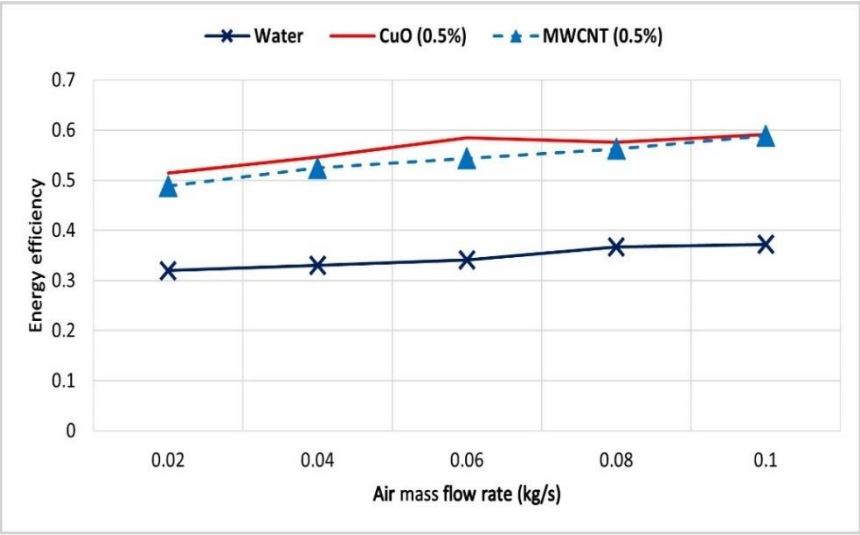

Figure 6.5. Variation of energy efficiency with airflow rate for various HTLs.

To provide a quantitative summary of the findings from sections 6.2 and 6.3 of this investigation, Table 6.2 consolidates key performance metrics. These metrics include outlet temperatures, total useful heat gain, and overall efficiency for the base fluid and both nanofluids. The comparison was conducted while maintaining a constant liquid flow rate of 0.02 kg/s and varying the air flow rate. Results for both the lowest and highest air flow rates are presented to illustrate the impact of this variation. This table facilitates a direct comparison of the performance of the fluids under identical operating conditions.

Table 6.2. Key performance metrics for base fluid and nanofluids at constant liquid flow rate (0.02 kg/s) and varying air flow rates.

Air Flow Rate	Fluid	Exit Liquid Temp. (°C)	Exit Air Temp. (°C)	Total Heat Gain (W)	Total Efficiency (%)
0.02 kg/s (lowest airflow)	Water	45.64	**47.43**	525	32
	0.5% MWCNT-H_2O	49.29	46.12	802	48.8
	0.5% CuO-H_2O	**49.78**	46.18	**843.81**	**51.4**
0.1 kg/s (highest airflow)	Water	45.15	**46.63**	610.65	37.2
	0.5% MWCNT-H_2O	50.32	45.93	966	58.8
	0.5% CuO-H_2O	**50.32**	45.97	**970**	**59.1**

As demonstrated quantitatively in Table 6.2, the CuO-H_2O nanofluid consistently achieved the highest total heat gain and overall efficiency across all airflow rates, reaching a peak of 970 W and 59.1% efficiency at 0.1 kg/s, highlighting its enhanced heat transfer capability.

6.4. The Impact of Liquid flow on The Exit Temperatures of DPSTC

After completing the fifteen intricate simulation processes, which focused on varying air flow rates, it became clear that optimal performance was observed at the highest flow rate utilized in the study, specifically 0.1 kg/s. As vividly depicted in the earlier figures, this optimal flow rate not only fostered maximum efficiency but also elevated the outlet liquid temperature to its peak and harnessed the greatest useful energy. This elevated performance uniquely distinguished it from all other tested rates. Building upon these exciting findings, a series of an additional fifteen simulations explored the fascinating dynamics of the same liquids: water, CuO-H_2O, and MWCNT-H_2O. The liquid flow rate varied systematically from 0.02 kg/s to 0.1 kg/s while keeping other parameters constant and maintaining the air flow rate at a constant 0.1 kg/s. Throughout this phase, a thorough analysis was conducted on the effects on both the outlet air and liquid temperatures, the useful heat gain, and overall efficiency.

Figure 6.6 illustrates the relationship between outlet air temperature and various liquid flow rates. As the liquid flow rate increases, the outlet air temperature decreases. Specifically, the temperature reduction is approximately 0.5 °C when water is used, whereas it reaches around 1.5 °C with nanofluids. This reduction can be attributed to the fact that higher flow rate values lead to a shorter heating duration for the liquid as it traverses through the risers. Consequently, this negatively impacts the outlet air temperature, particularly given the already high airflow. This prevents adequate heating of the air due to the high fluid velocity.

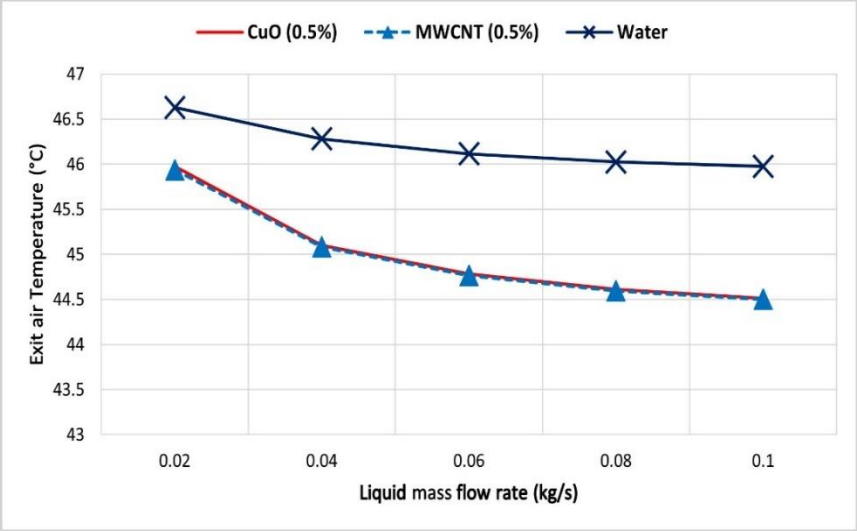

Figure 6.6. Variation of exit air temperature with liquid flow rate for various HTLs.

The relationship between outlet liquid temperature and liquid mass flow is shown in Figure 6.7. As anticipated, the outlet liquid temperature decreases as the liquid mass flow increases. Specifically, when the liquid mass flow rate increases from 0.02 kg/s to 0.1 kg/s, the outlet water temperature decreases by approximately 2.5°C. In comparison, the temperature drop for nanofluids over the same flow range is around 6 °C. The increased flow rate shortens the duration of heat exchange between the fluids, resulting in reduced heat transfer and, consequently, a lower outlet temperature. Overall, for all tested liquids, the outlet liquid temperature remains higher than the inlet temperature. For both CuO-H_2O and MWCNT-H_2O nanofluids at a flow rate of 0.02 kg/s, the outlet temperature increases by about 10 °C, representing a 25% rise over the inlet temperature. In comparison, the temperature increase for water is only 5 °C, corresponding to a 12.5% increase at the same flow rate.

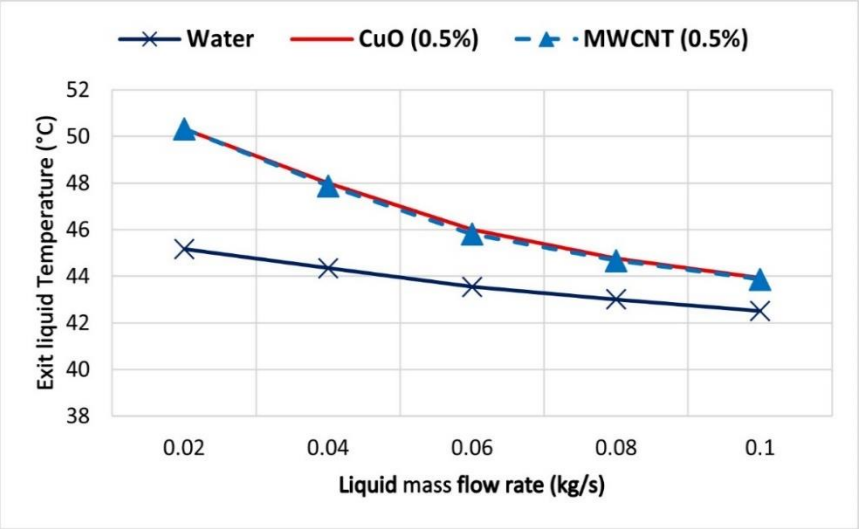

Figure 6.7. The effect of liquid flow rate on the exit liquid temperature for various HTLs.

6.5. The Impact of Liquid flow on The Performance of DPSTC

Displaying the temperature contour of the two nanofluids may not provide meaningful insights, as their temperature distributions are identical. Consequently, readers would be unable to differentiate between the contours of the two liquids. Instead, it would be more advantageous to illustrate the useful heat collected from both the air and liquid components of the collector, as well as the associated thermal efficiency. These aspects are depicted in Figures 6.8 and 6.9, respectively.

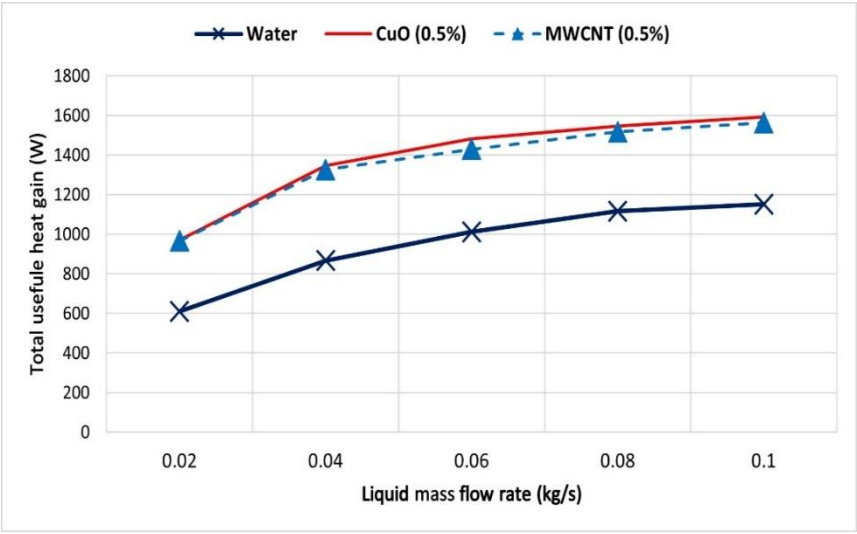

Figure 6.8. Impact of liquid flow rate on total useful heat gain for various HTLs.

At elevated mass flow rates, the fluid exhibits an increased velocity, resulting in a reduced dwell time within the collector. Consequently, the increment in temperature is minimized. Nevertheless, the increased mass being heated per unit of time leads to an increase in the total energy transferred. Furthermore, this condition also mitigates thermal losses attributable to a lower average fluid temperature, thereby enhancing the efficiency of the collector system.

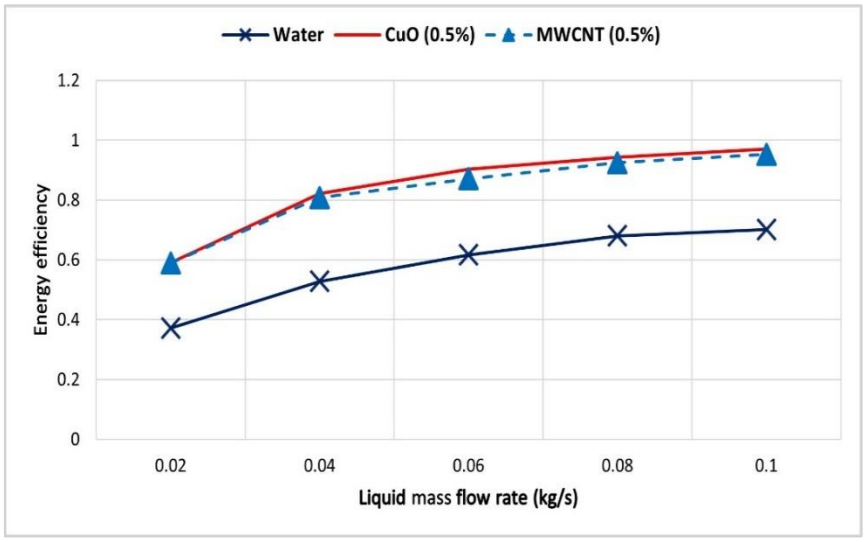

Figure 6.9. Impact of liquid flow rate on total energy efficiency for various HTLs.

In Figure 6.9 the efficiency of the DPSTC is improved when using certain liquids and increasing the liquid flow rates. Notably, when water is used as the circulating liquid, the efficiency increases from 37% to 70% as the flow rate rises from 0.02 kg/s to 0.1 kg/s. Additionally, the use of both nanofluids boosts the overall efficiency of the DPSTC. At a flow rate of 0.02 kg/s, both nanofluids demonstrate an enhancement of approximately 59%. At a flow rate of 0.1 kg/s, the CuO-H_2O nanofluid achieves an efficiency of 97%, while the MWCNT-H_2O nanofluid reaches an efficiency of 95%. This indicates the superiority of CuO over MWCNT.

Table 6.3 presents a detailed quantitative analysis of the outcomes from the second phase of simulations. It contrasts the performance of water, MWCNT-H_2O, and CuO-H_2O at a steady airflow rate of 0.1 kg/s, while the liquid flow rate was gradually raised from 0.02 kg/s to 0.1 kg/s.

Table 6.3. Key performance metrics for base fluid and nanofluids at constant air flow rate (0.1 kg/s) and varying liquid flow rates.

Liquid Flow Rate	Fluid	Exit Liquid Temp. (°C)	Exit Air Temp. (°C)	Total Heat Gain (W)	Total Efficiency (%)
0.02 kg/s (lowest liquid flow)	Water	45.15	**46.63**	610.65	37.2
	0.5% MWCNT-H_2O	50.32	45.93	966	58.8
	0.5% CuO-H_2O	**50.32**	45.97	**970.16**	**59.11**
0.1 kg/s (highest liquid flow)	Water	42.9	**45.97**	1152	70.2
	0.5% MWCNT-H_2O	43.87	44.5	1563.2	95.2
	0.5% CuO-H_2O	**43.93**	44.5	**1592**	**97**

The data presented in Table 6.3 clearly demonstrate that increasing the liquid flow rate is essential for maximizing system efficiency. The advantages of the CuO-H_2O nanofluid become particularly evident at the highest flow rate of 0.1 kg/s, where it achieves an overall efficiency of 97% and a total heat gain of 1592 W. This marks a significant improvement compared to water, which reaches a maximum efficiency of 70.2% and a heat gain of 1152 W under the same conditions.

As a summary, I highlighted the significant benefits of employing nanofluids, specifically CuO-H_2O at a concentration of 0.5%, in enhancing the thermal performance, heat gain, and overall system efficiency of DPSTC, thereby suggesting a significant advancement over traditional water-based systems. The superior thermal conductivity and heat capacity of CuO nanofluid were pivotal in achieving these improvements. It was conclusively shown that the DPSTC, operating under conditions of an air flow rate of 0.1 kg/s and a liquid flow rate of 0.1 kg/s, achieved optimal performance, especially with the application of nanofluids.

In the next chapter, we further analyzed the same DPSTC presented in Chapter 5 using different hybrid nanofluids. Additionally, the previous simulations were repeated and combined with new results to support an environmental assessment.

7. ENERGY, ECONOMIC, AND ECOLOGICAL ASPECTS OF A DUAL-PURPOSE SOLAR COLLECTOR USING VARIOUS LIQUIDS

In this chapter, I divided the study into two parts. In the first part, I investigated the performance of DPSTC numerically using three different kinds of hybrid nanofluids: 1%vol MWCNT-CuO/H_2O, 1%vol SWCNT-CuO/H_2O, and 0.1%vol ZrO-SiC/H_2O. This investigation builds upon previous numerical studies reported in [107] and [54], in which I examined various working fluids, including water, Therminol, Dowtherm, and mono nanofluids, specifically 0.5%vol CuO-H_2O and 0.5%vol MWCNT-H_2O within the DPSTC. The novelty of the present work lies in the application of HNFs, particularly the ZrO-SiC/H_2O nanofluid in DPSTC, a topic that, to the best of my knowledge, has not been explored before. No prior studies have investigated the use of HNFs in DPSTC, making the application of ZrO-SiC/H_2O uniquely significant. Only one publication has addressed this liquid concerning its impact on solar water collector performance, which motivates me to further explore its potential. In the second part of this chapter, I evaluated all the numerical results obtained in the first part related to the HNFs, in conjunction with previous simulations presented in Chapters 5 and 6, through an environmental assessment. I analyzed the savings in coal, gas, and electricity, along with their corresponding carbon dioxide emissions. Furthermore, I explored the size reduction, pressure drop, and pumping power of the DPSTC while applying various liquids. These aspects have not previously received attention in the field of DPSTC [110].

7.1. Thermophysical Properties of HNFs

The calculation of the thermophysical properties of the hybrid nanofluid needs to predetermine the total volume fraction ($\emptyset_{hnf}$) which is determined as [111]:

$$\emptyset_{hnf} = \emptyset_{np1} + \emptyset_{np2}\ , \tag{7.1}$$

The following theoretical equations are employed to evaluate the density (ρ_{hnf}), specific heat ($C_{p,hnf}$), thermal conductivity (k_{hnf}), and dynamic viscosity (μ_{hnf}) of the HNF [74]:

$$\rho_{hnf} = \emptyset_{np1}\rho_{np1} + \emptyset_{np2}\rho_{np2} + (1-\emptyset)\rho_{bf}\ , \tag{7.2}$$

$$C_{p,hnf} = \frac{\emptyset_{np1}\rho_{np1}C_{p,np1}+\emptyset_{np2}\rho_{np2}C_{p,np2}+(1-\emptyset_T)\rho_{bf}C_{p,bf}}{\rho_{hnf}}, \tag{7.3}$$

$$\mu_{hnf} = \mu_{bf}\left(\frac{1}{(1-\emptyset_T^{2.5})}\right), \tag{7.4}$$

$$k_{hnf} = \frac{\frac{\emptyset_{np1}k_{np1}+\emptyset_{np2}k_{np2}}{\emptyset_T}+2k_{bf}+2(\emptyset_{np1}k_{np1}+\emptyset_{np2}k_{np2})-2\emptyset_T k_{bf}}{\frac{\emptyset_{np1}k_{np1}+\emptyset_{np2}k_{np2}}{\emptyset_T}+2k_{bf}-2(\emptyset_{np1}k_{np1}+\emptyset_{np2}k_{np2})+2\emptyset_T k_{bf}}, \tag{7.5}$$

here, the subscripts 1 and 2 indicate nanoparticle types; superscripts hnf, np and bf indicate hybrid nanofluid, nanoparticle and base fluid.

In line with the methodology outlined in Chapter 6 for mono-nanofluids, the specific particle sizes and stability characteristics of the hybrid nanoparticles were not defined as direct inputs for the model. The numerical model relies on effective bulk thermophysical properties, which are derived from established correlations. This approach assumes a uniform and stable dispersion of nanoparticles within the base fluid. Table 7.1 presents the properties of the HNFs used in the current simulation, which serve as inputs for the ANSYS setup.

Table 7.1. Thermophysical properties of the various HNFs used in the simulation.

Physical properties	ZrO2- SiC [74]	MWCNT- CuO [72]	SWCNT- CuO [72]
$\boldsymbol{\rho}$ (kg/m^3)	1002.554	1003.132	1013.129
$\boldsymbol{k}$ (W/(m. K))	0.785	0.6164	0.6164
$\boldsymbol{C_p}$ (J/(kg. K))	4163.2	4127.99	4085.58
$\boldsymbol{\mu}$ (mPa·s)	0.00165	0.00105	0.00105

7.2. Numerical Investigation Using HNFs

In this section of the study, ANSYS Fluent simulation has been utilized to analyze the DPSTC. A comprehensive description of this collector, including geometry modeling, meshing, setup processes, and validation has been presented in detail Chapter 2. During the simulation, the fluid flow regime is assumed to be laminar. The solar radiation kept at 900 W/m², with constant inlet temperatures for both air and liquid at 45°C and 40°C, respectively. Previous investigation concluded that the collector's performance metrics improve significantly at a high air flow rate of 0.1 kg/s. In light of this finding and to avoid prolonging the simulation duration, the current simulation is conducted at a fixed air flow rate of 0.1 kg/s, while varying the liquid flow rates from 0.02 to 0.1 kg/s.

The variation of the exit liquid temperatures and total heat gain of the DPSTC with the liquid mass flow for various tested liquids is shown in Figures 7.1 and 7.2. It is logical that increasing the mass flow rate lowers the outlet temperature due to reduced time for heat transfer. Interestingly, the highest outlet temperature occurs at a flow rate of 0.02 kg/s, while the lowest occurs at 0.1 kg/s. When using SWCNT-CuO/H2O, the exit temperature reaches a maximum of 50.38 °C, compared to approximately 45 °C for other liquids, including water (see Figure 7.1). The temperature drop observed with SWCNT-CuO/H_2O is 6.5°C, whereas for other liquids, it is only 2.8°C.

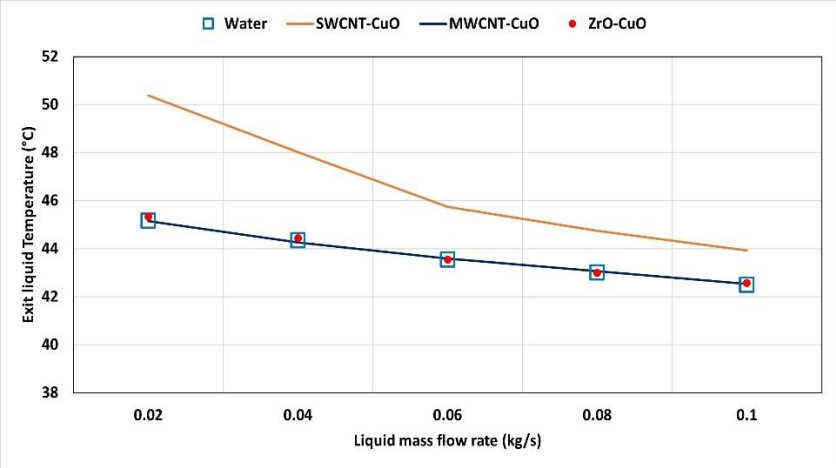

Figure 7.1. The variation of the exit liquid temperature of DPSTC with liquid flow rate.

The total heat gain of the DPSTC, as a function of liquid mass flow rate, is illustrated in Figure 7.2. It is evident that higher liquid flow rates result in higher heat gain, as the increased liquid velocity improves convective heat transfer and overall heat exchange process. The SWCNT-CuO/H_2O exhibited the highest heat gain values of 1587.9 W followed by ZrO-SiC/H_2O at 1182 W, MWCNT-CuO/H_2O at 1166.3 W, and finally by water at 1152 W. Notably, SWCNT-CuO/H_2O showed a 37.8% improvement in heat gain compared to water.

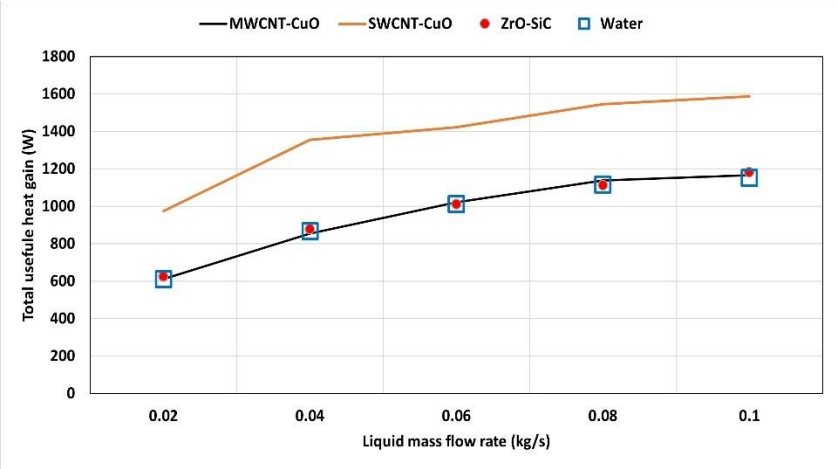

Figure 7.2. The variation of total heat gain of the DPSTC with liquid flow rate.

According to the prior numerical studies [54] and [107], it has been determined that the utilization of Therminol, Dowtherm, and CuO-H_2O liquids can significantly improve the overall performance of the DPSTC. Consequently, these HTFs are currently undergoing further examination at varying liquid flow rates to optimize their performance. The outcomes of this test are depicted in Figure 7.3, which illustrates the total heat gain.

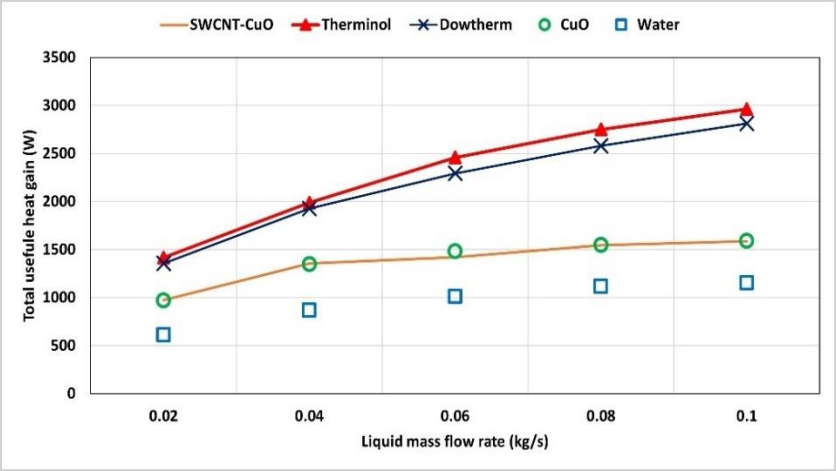

Figure 7.3. Variation of heat gain of DPSTC with various working liquids at different liquid flow rates.

The highest heat gain of the DPSTC is achieved when utilizing both Therminol and Dowtherm. The maximum recorded values are 2962.2 W for Therminol and 2812.1 W for Dowtherm, representing remarkable improvements of 157% and 144%, respectively, compared to using water. Additionally, when compared to CuO-H_2O and SWCNT-CuO/H_2O, which produce nearly identical results, the enhancements reflect increases of 86.5% for Therminol and 77% for Dowtherm. This superiority is attributed to the advantageous thermal properties of oil-based liquids in contrast to nanofluids and hybrid nanofluids.

7.3. DPSTC Size Reduction

The percentage reduction in the DPSTC area for various working liquids is illustrated in Figure 7.4, focusing on the best-performing types: Therminol, Dowtherm, CuO-H_2O, and SWCNT-CuO/H_2O. These liquids demonstrate improved thermal performance, necessitating less area to achieve the same thermal output.

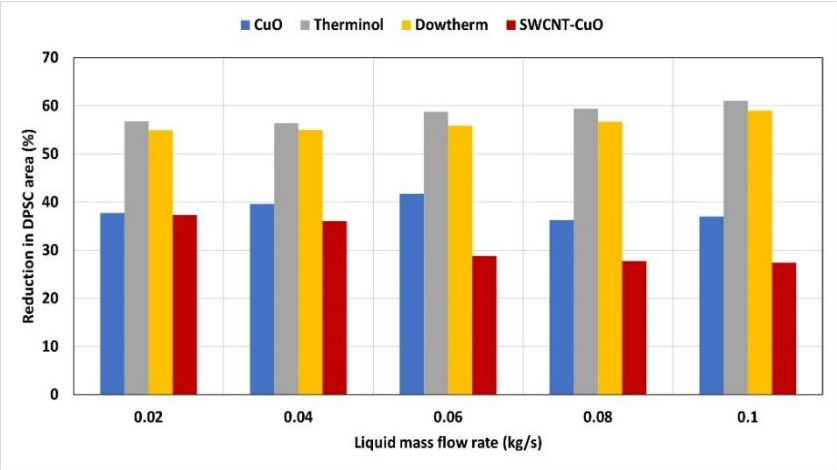

Figure 7.4. Reduction in DPSTC area for various working liquids under varying flow rates.

The decrease in the collector area signifies improved thermal performance, as a more effective heat transfer medium requires less space for equivalent thermal results. Therminol shows the greatest reduction in the DPSTC area, increasing from about 57% at 0.02 kg/s to over 60% at 0.1 kg/s, with Dowtherm closely trailing behind. These findings underscore the strong performance of synthetic oils at elevated mass flow rates.

In contrast, nanofluids present less favorable reductions, specifically, SWCNT-CuO experiences the smallest reduction in DPSTC area, around 27% at 0.1 kg/s, while CuO achieves modest improvements (35% to 40%) beyond a flow rate of 0.06 kg/s. Notably, SWCNT-CuO exhibits a decrease in area reduction with increasing flow rates, likely due to viscosity or nanoparticle dispersion issues that offset thermal conductivity benefits.

7.4. Fossil Fuel and Electricity Consumption with Associated CO_2 Emissions

If a coal- fired boiler is assumed to be used to produce an equivalent useful heat gain as achieved applying Therminol, Dowtherm, CuO-H_2O, and SWCNT-CuO/H_2O liquids in the DPSTC, the potential savings in coal mass, the corresponding reduction in CO_2 emissions, and yearly CO_2 cost savings are shown in Figures 7.5.

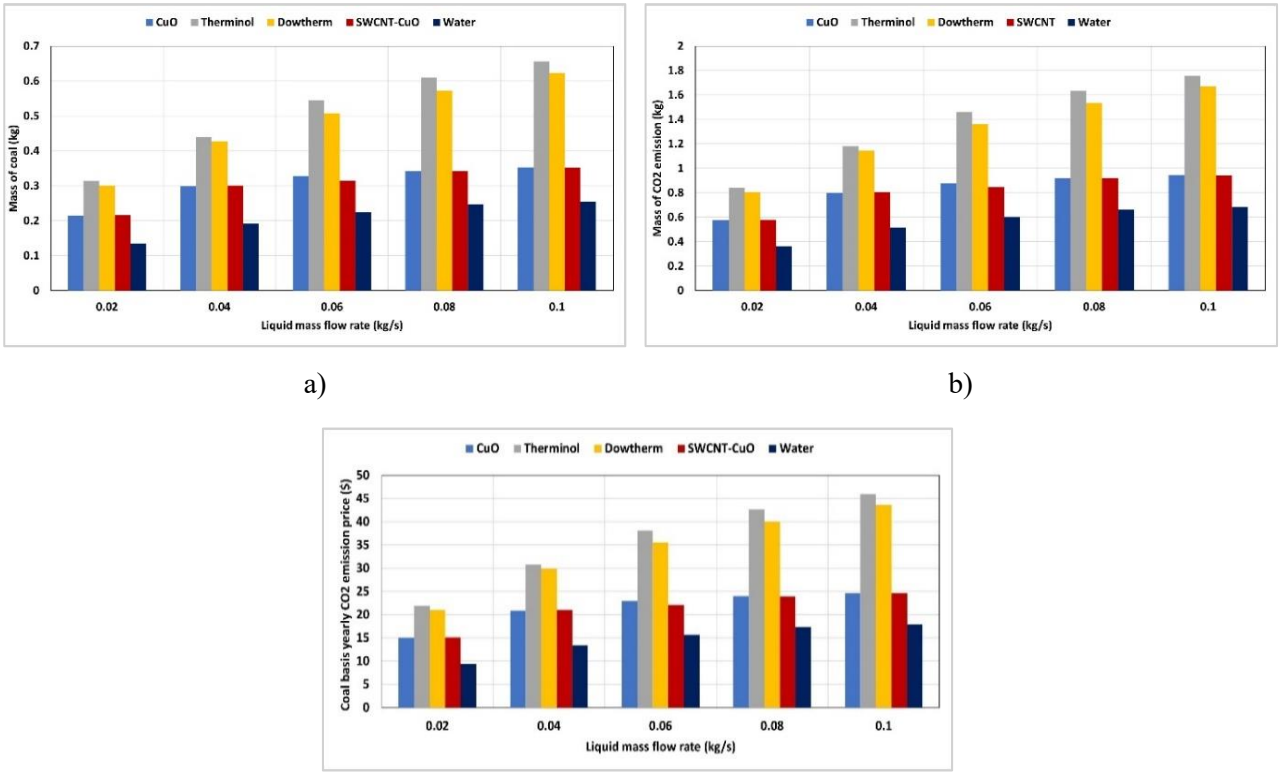

Figure 7.5. (a) Saved coal, (b) CO_2 emissions, and (c) annual CO_2 cost savings when using DPSTC with different liquids instead of a coal- fired boiler at various liquid flow rates.

The data presented in Figure 7.5a indicates that the coal savings increase with higher flow rates due to enhanced heat transfer. Applying nanofluids and oils significantly reduces coal consumption compared to other liquids. At a flow rate of 0.1 kg/s, Therminol achieves the highest coal savings, totaling 0.67 kg, closely followed by Dowtherm, which saves over 0.62 kg. In contrast, CuO/H_2O and SWCNT-CuO/H_2O can save around 0.36 kg. Water, on the other hand, shows the lowest coal savings, highlighting its inferior efficiency relative to other liquids.

Figure 7.5b depicts the CO_2 emissions savings achieved by various working fluids as the liquid flow rate varies. Therminol and Dowtherm achieve the highest savings, about 1.8 kg and 1.7 kg at a flow rate of 0.1 kg/s, significantly surpassing nanofluids, which save 0.91 kg, and water at 0.68 kg. Notably, water exhibits the lowest CO_2 savings, a result of its limited thermal capacity and lower heat transfer efficiency.

Figure 7.5c shows the annual CO_2 cost savings from coal consumption. At a liquid flow rate of 0.1 kg/s, Therminol and Dowtherm provide the highest annual savings, reaching 45.9$ and 43.5$, respectively. In comparison, both SWCNT-CuO/H_2O and CuO/H_2O achieve maximum savings of 24.6$. On the other hand, water has the lowest annual CO_2 cost savings of 17.8$.

The gas savings and CO_2 emissions resulting from various liquids utilized in DPSTC, when compared to gas-fired boilers are shown in Figures 7.6a and b. All liquids demonstrated increased gas savings at higher flow rates, which subsequently led to greater reductions in CO_2 emissions, as these emissions are directly related to fossil fuel consumption.

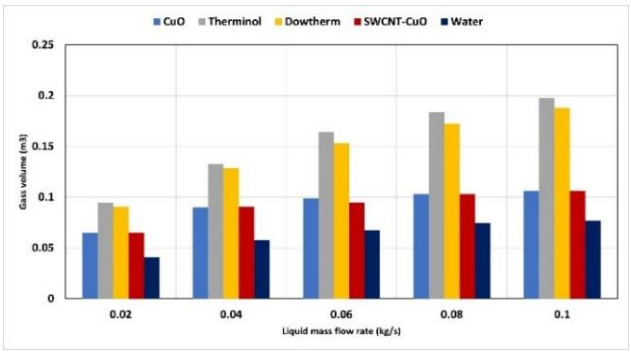

a)

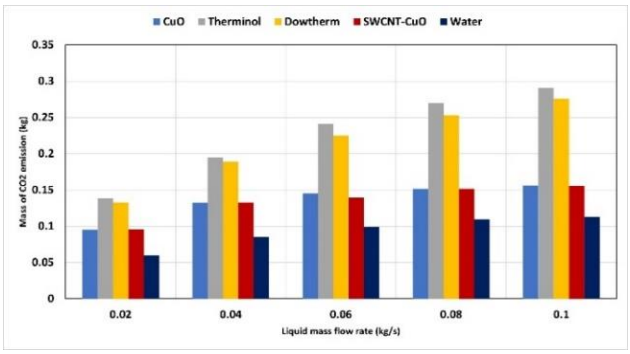

b)

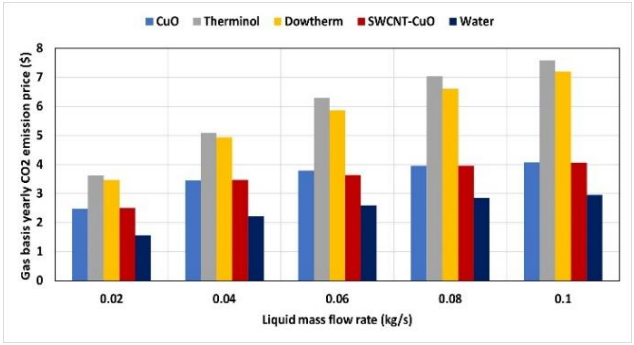

c)

Figures. 7.6. (a) Saved gas, (b) CO_2 emissions, and (c) annual CO_2 cost savings when using DPSTC with different liquids instead of a gas- fired boiler at various liquid flow rates.

In Figure 7.6a, Therminol and Dowtherm achieved the highest gas savings of about 0.20 m^3 at 0.1 kg/s. SWCNT-CuO and CuO nanofluids performed moderately, outperforming water but still falling short of the performance of thermal oils. Water exhibited the lowest gas savings due to its reduced heat transfer efficiency. A similar trend can be observed in Figure 7.6b,where Therminol and Dowtherm attained the greatest CO_2 reductions, arround 0.29 kg at a flow rate of 0.1 kg/s, whereas water consistently showed the least emissions reduction. The maximum annual savings of CO_2 emissions recorded at 7.5$ for Therminol, 7$ for Dowtherm, 4$ for both SWCNT-CuO and CuO nanofluids, and 3$ for water (see Figure 7.6c). It is attributed to the fact that burning gas has the lowest environmental impact, as it produces fewer CO_2 emissions.

The energy savings achieved by using various liquids in DPSTC, as compared to electric boilers, along with their associated CO_2 emissions, are shown in Figure 7.7a and b. Higher liquid flow results in increased energy savings and reduced CO_2 emissions. Figure 7.7a shows that Therminol and Dowtherm provide the greatest energy savings, up to 3.65 kWh and 3.5 kWh respectively, which correlates to CO_2 reductions of nearly 1.7 kg at a flow rate of 0.1 kg/s (see Figure 7.7b). SWCNT-CuO and CuO nanofluids show moderate savings, surpassing water but lagging behind thermal oils. Water yields the lowest savings, not exceeding 1.5 kWh even at maximum flow rates. Accordingly, the maximum annual savings of CO_2 emissions were 44.5$ for Therminol, 42.2$ for Dowtherm, 23.8$ for both SWCNT-CuO and CuO nanofluids, and 17.3$ for water (see Figure 7.7c).

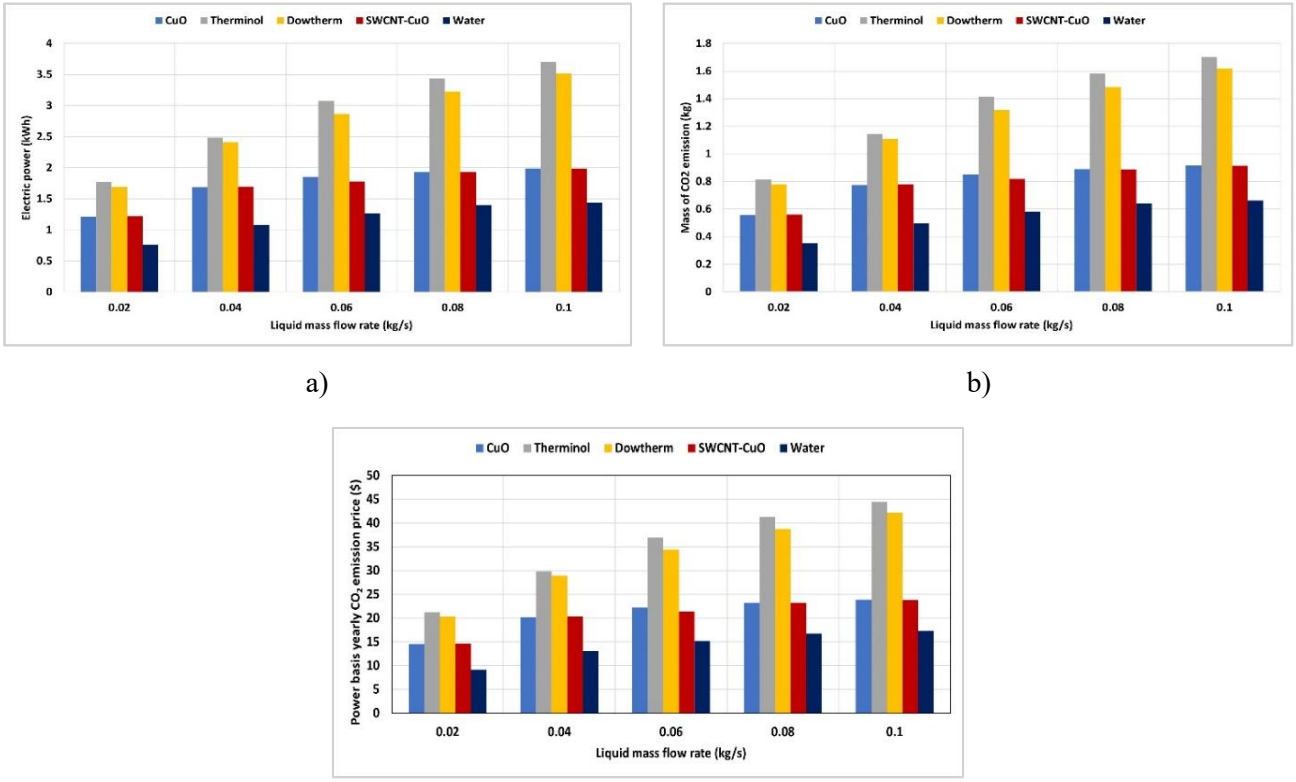

a) b)

c)

Figure 7.7. (a) Saved power, (b) CO_2 emissions, and (c) annual CO_2 cost savings when using DPSTC with different liquids instead of electric boiler at various liquid flow rates.

7.5. Pressure Drop and Pumping Power

The relationship between pressure drop and pumping power as functions of increasing mass flow rate is depicted in Figure 7.8. Pumping power is directly proportional to the mass flow rate. As anticipated, the pressure drop consistently rises with the mass flow rate for all liquids, primarily due to the increased flow velocity, which heightens the frictional resistance within the flow channel.

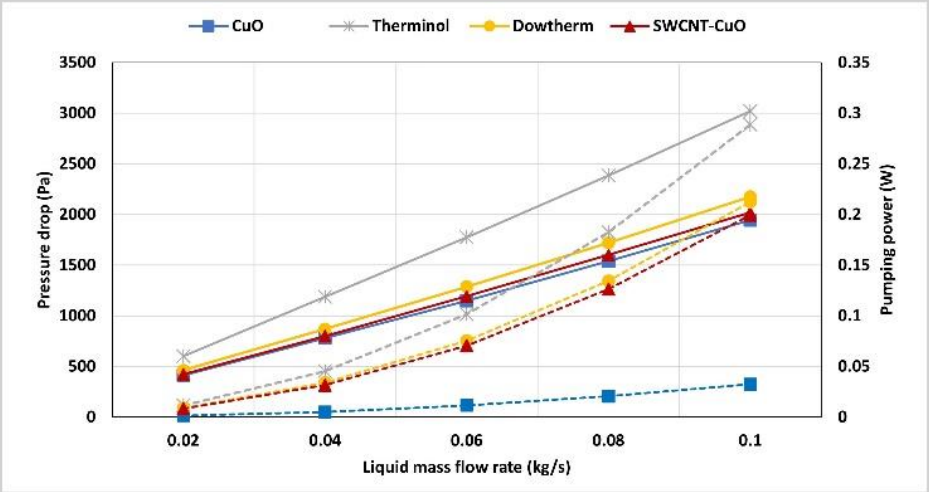

Figure 7.8. The variation of pressure drop (solid line) and pumping power (dotted line) with liquid flow rate.

Notably, CuO nanofluid exhibits lower pumping power and pressure drop than other liquids due to its relatively lower viscosity. In contrast, Therminol demonstrates the highest pressure drop and pumping power, followed by Dowtherm, owing to its greater viscosity and density. This results in increased friction, which may lead to higher operational costs due to the elevated pressure drop and pumping power, which are critical considerations in system design. CuO, Dowtherm, and SWCNT-CuO strike a balance with moderate pressure drops and pumping power, potentially enhancing thermal performance.

As a summary, I concluded that SWCNT-CuO/H_2O liquid significantly improves the overall thermal performance of the DPSTC when compared to MWCNT-CuO/H_2O and ZrO-SiC/H_2O liquids. The improvement in exit liquid temperature and total heat gain are recorded at 11.5% and 38%, respectively. This indicates that this particular HNF can be effectively applied in DPSTC applications.

I revealed that both Therminol and Dowtherm significantly outperformed CuO/H_2O, SWCNT-CuO/H_2O, and water. Additionally, a considerable reduction in DPSTC area was observed: up to 61% for Therminol, 59% for Dowtherm, 41.7% for CuO/H_2O, and 37% for SWCNT-CuO/H_2O, all relative to water.

The maximum potential savings in coal, gas, and electricity from the use of coal-fired, gas, and electric boilers are as follows: Therminol achieves savings of 0.67 kg, 0.20 m^3, and 3.7 kWh, Dowtherm offers 0.62 kg, 0.18m^3, and 3.5 kWh, both CuO/H_2O and SWCNT-CuO/H_2O yield 0.36 kg, 0.1m^3, and 1.98 kWh, and water results in 0.25 kg, 0.07m^3, and 1.4 kWh. Additionally, the associated CO_2 emissions (in kg) linked to these savings have also been computed. I concluded that DPSTC has a lower environmental impact compared to other STs. However, pumping power is a critical operating factor that can adversely influence performance. The findings indicate that

Therminol requires the highest pumping power at 0.3 W, while both Dowtherm and SWCNT-CuO/H_2O require approximately 0.2 W, with CuO requiring the least power at 0.03 W. To minimize hydraulic losses while still obtaining potential thermal benefits, it is advisable to maintain a low liquid flow rate for all liquid types.

After conducting a thorough analysis of the thermal performance (Section 7.2), the implications of system design (Sections 7.3 and 7.5), and the associated environmental and economic advantages (Section 7.4) of various advanced heat transfer fluids, it is now important to integrate these insights into a single, cohesive framework.

Table 7.2 provides a definitive comparison of all leading fluids, water, thermal oils, mono-nanofluids, and hybrid nanofluids. It compares their performance metrics at two critical operational conditions: a low liquid flow rate (0.02 kg/s) and a high liquid flow rate (0.1 kg/s), both at a constant high air flow rate of 0.1 kg/s. This detailed summary facilitates a direct evaluation of the important trade-offs between optimizing thermal efficiency, reducing system size and pumping power, and achieving significant environmental and economic benefits. It acts as the final synthesis of this study, offering the essential information needed to identify the most suitable fluid for specific application objectives.

Table 7.2. Comprehensive comparison of thermal performance, system design, and environmental impact for all tested fluids at low (0.02 kg/s) and high (0.1 kg/s) liquid flow rates.

Performance Metric	Working Fluid (Type)	at low liquid flow rate (0.02 kg/s)	at high liquid flow rate (0.1 kg/s)
THERMAL PERFORMANCE			
Exit Liquid Temp. (°C)	Water (Base Fluid)	45.15	42.5
	Therminol	51.54	46.33
	Dowtherm	51.17	46
	0.5% CuO-H_2O	50.32	43.93
	1% SWCNT-CuO/H_2O	50.38	43.92
Total Useful Heat Gain (W)	Water (Base Fluid)	610.65	1152
	Therminol	1415.3	2962.2
	Dowtherm	1355.2	2812.1
	0.5% CuO-H_2O	970.1	1592
	1% SWCNT-CuO/H_2O	975	1587.9
SYSTEM DESIGN and HYDRAULICS			
Collector Area Reduction (%)	Water (Base Fluid)	*Baseline*	*Baseline*
	Therminol	56.8	61.1
	Dowtherm	55	59

		0.5% CuO-H_2O	37.7	37
		1% SWCNT-CuO/H_2O	37.3	27.4
Pressure Drop (Pa)		Water (Base Fluid)	*Baseline*	*Baseline*
		Therminol	601.7	3019.1
		Dowtherm	462.75	2175.3
		0.5% CuO-H_2O	414	1944.6
		1% SWCNT-CuO/H_2O	423.5	2019.2
Pumping Power (W)		Water (Base Fluid)	*Baseline*	*Baseline*
		Therminol	0.0115	0.288
		Dowtherm	0.01	0.212
		0.5% CuO-H_2O	0.0013	0.032
		1% SWCNT-CuO/H_2O	0.008	0.1993
ENVIRONMENTAL and ECONOMIC IMPACT				
Compared to Coal Boiler	Saved Coal (kg)	Water (Base Fluid)	0.135	0.255
		Therminol	0.313	0.656
		Dowtherm	0.3	0.623
		0.5% CuO-H_2O	0.215	0.352
		1% SWCNT-CuO/H_2O	0.216	0.352
	CO_2 Emissions Reduced (kg)	Water (Base Fluid)	0.362	0.684
		Therminol	0.84	1.76
		Dowtherm	0.804	1.67
		0.5% CuO-H_2O	0.576	0.945
		1% SWCNT-CuO/H_2O	0.579	0.943
	Annual Cost Savings ($)	Water (Base Fluid)	9.46	17.85
		Therminol	22	46
		Dowtherm	21	43.5
		0.5% CuO-H_2O	15	24.67
		1% SWCNT-CuO/H_2O	15.11	24.61
Compared to Gas Boiler	Saved Gas (m^3)	Water (Base Fluid)	0.04	0.076
		Therminol	0.094	0.19

		Dowtherm	0.09	0.187
		0.5% CuO-H_2O	0.064	0.106
		1% SWCNT-CuO/H_2O	0.065	0.106
	CO_2 Emissions Reduced (kg)	Water (Base Fluid)	0.06	0.113
		Therminol	0.138	0.29
		Dowtherm	0.132	0.275
		0.5% CuO-H_2O	0.095	0.156
		1% SWCNT-CuO/H_2O	0.0955	0.155
	annual Cost Savings ($)	Water (Base Fluid)	1.56	2.95
		Therminol	3.62	7.58
		Dowtherm	3.46	7.2
		0.5% CuO-H_2O	2.48	4.07
		1% SWCNT-CuO/H_2O	2.49	4.06
Compared to Electric Boiler	Saved Power (kWh)	Water (Base Fluid)	0.76	1.44
		Therminol	1.77	3.7
		Dowtherm	1.7	3.51
		0.5% CuO-H_2O	1.21	2
		1% SWCNT-CuO/H_2O	1.22	2
	CO_2 Emissions Reduced (kg)	Water (Base Fluid)	0.351	0.66
		Therminol	0.813	1.7
		Dowtherm	0.78	1.61
		0.5% CuO-H_2O	0.557	0.915
		1% SWCNT-CuO/H_2O	0.56	0.913
	Annual Cost Savings ($)	Water (Base Fluid)	9.16	17.3
		Therminol	21.2	44.46
		Dowtherm	20.34	42.2
		0.5% CuO-H_2O	14.56	23.9
		1% SWCNT-CuO/H_2O	14.63	23.8

8. THESES – NEW SCIENTIFIC RESULTS

T1. I modeled the DPSTC as a parallel flow heat exchanger and developed a mathematical framework based on the ε-NTU method, applying the effectiveness equation specific to such exchangers. This novel approach, not previously used for DPSTCs, is justified by the collector's dual-channel structure. A MATLAB simulation was developed using meteorological data, and results were validated against experimental studies using RPE and ARPE metrics, confirming the model's accuracy and reduced computational complexity [P1].

T2. I developed three mathematical approaches to analyze the DPSTC. To implement these approaches, I created three MATLAB codes: C1, C2, and C3. Code C1 uses the (ε- NTU) method, C2 employs the heat removal term, and C3 uses the effectiveness term for a parallel flow heat exchanger. Each code underwent mathematical modeling, simulations, and experimental validation, showing good alignment with experimental data. I calculated the Root Mean Square Error (RMSE) and Mean Absolute Error (MAE) for each code, and found that C3 outperformed the other models with the lowest error values. As a result, C3 accurately predicts water and air outlet temperatures and the thermal performance of the DPSTC, significantly contributing to future research in this field [P2].

T3. I investigated the influence of various heat transfer fluids on the thermal behavior of DPSTC using ANSYS Fluent. I noted a considerable gap in the existing literature regarding Computational Fluid Dynamics (CFD) studies related to this type of collector, which I identified as a noteworthy innovation in my work. I evaluated three distinct working fluids: water, Therminol VP-1, and Dowtherm A. The examination of oil-based fluids, alongside conventional water, is particularly pertinent as water becomes ineffective in extreme temperatures. Additionally, the lack of research investigating these alternative fluids in DPSTC systems further underscores the originality of my study. My findings indicate that using Therminol and Dowtherm can considerably improve the overall thermal performance of the DPSTC. Therminol and Dowtherm achieve higher temperatures for the absorber plate, outlet air, and liquid [P3].

T4. I analyzed the performance of DPSTC using CFD simulations in ANSYS Fluent, employing nanofluids CuO-H_2O and MWCNT-H_2O at a 0.5% volume concentration. These nanofluids were selected based on a literature review highlighting their enhanced thermal performance in solar collectors. I compared their effectiveness to that of water, marking the novelty of this research as no prior studies have focused on these nanofluids in DPSTCs. The investigation included two phases: the first varied air flow rates while keeping other parameters constant, and the second varied liquid flow rates. I evaluated the impact of nanofluids on outlet temperatures, heat gains, and overall thermal efficiency. Additionally, I developed a MATLAB program to calculate the thermophysical properties of the nanofluids, allowing for seamless integration into the ANSYS simulation [P4].

T5. I investigated the performance of the DPSTC numerically using ANSYS Fluent, employing three different types of hybrid nanofluids: 1% vol MWCNT-CuO/H_2O, 1% vol SWCNT-CuO/H_2O, and 0.1% vol ZrO-SiC/H_2O. To date, there have been no previous studies

examining the use of hybrid nanofluids (HNFs) in DPSTC, making this application a novel contribution to the field. My findings indicate that the SWCNT-CuO/H_2O fluid significantly enhances the overall thermal performance of the DPSTC in comparison to MWCNT-CuO/H_2O and ZrO-SiC/H_2O. This suggests that the SWCNT-CuO/H_2O nanofluid can be effectively utilized in DPSTC applications [P5].

T6. I evaluated the numerical results obtained in T5 which are related to the HNFs, alongside previous simulation results presented in T4 and T3, through an environmental assessment. My analysis focused on the savings in coal, gas, and electricity, as well as the corresponding carbon dioxide emissions. Additionally, I investigated the size reduction, pressure drop, and pumping power of the DPSTC while using various liquids. These factors have not been previously addressed in the field of DPSTC, making this analysis a novel contribution to this field. I found that both Therminol and Dowtherm significantly outperform other liquids, leading to a considerable reduction in the DPSTC area. Moreover, these two fluids provide the maximum potential savings in coal, gas, and electricity compared to other liquids. However, the findings also indicate that Therminol requires the highest pumping power, followed by Dowtherm and SWCNT-CuO/H_2O, while CuO requires the least power. To minimize hydraulic losses while still achieving potential thermal benefits, it is advisable to maintain a low liquid flow rate for all liquid types [P5].

ACKNOWLEDGEMENTS

I wish to express my deepest and most sincere gratitude to my supervisor, Dr. Krisztián Hriczó. His continuous support, invaluable guidance, and unwavering patience were fundamental to the successful completion of this dissertation. His insightful feedback and expert advice have not only shaped this work but have also profoundly developed my skills as a researcher.

I also extend my sincere thanks and appreciation to my colleague, Dr. Issa Omle, who has been an excellent advisor throughout this journey. I cannot fully express my gratitude for your support and guidance.

This journey would not have been possible without the unwavering love and support of my family. I am eternally grateful to my mother for her constant prayers and moral encouragement, and to the enduring spirit of my father, whose presence and guidance I have felt throughout my studies. My deepest thanks go to my brother and sister for their continual encouragement.

Above all, I owe my heartfelt gratitude to my wonderful wife, who has been my rock, my greatest supporter, and my best friend through every challenge. Her sacrifice and faith in me have been my strongest motivation. To my children, who filled my life with joy and perspective, I offer my deepest thanks for their patience, understanding, and unconditional love during my many absences.

REFERENCES

[1] M. I. Afridi et al., “Numerical investigation on the performance of the solar air collector using jet impingement with W-shaped arrangement,” Case Studies in Thermal Engineering, vol. 71, p. 106154, Jul. 2025, doi: 10.1016/J.CSITE.2025.106154.

[2] P. A. Owusu and S. Asumadu-Sarkodie, “A review of renewable energy sources, sustainability issues and climate change mitigation,” Cogent Eng, vol. 3, no. 1, Dec. 2016, doi: 10.1080/23311916.2016.1167990;JOURNAL:JOURNAL:OAEN20;WGROUP:STRING:PUBLICATION.

[3] S. Bazri, I. A. Badruddin, M. S. Naghavi, O. K. Seng, and S. Wongwises, “An analytical and comparative study of the charging and discharging processes in a latent heat thermal storage tank for solar water heater system,” Solar Energy, vol. 185, 2019, doi: 10.1016/j.solener.2019.04.046.

[4] M. M. Hasan et al., “Harnessing Solar Power: A Review of Photovoltaic Innovations, Solar Thermal Systems, and the Dawn of Energy Storage Solutions,” Energies (Basel), vol. 16, no. 18, 2023, doi: 10.3390/en16186456.

[5] S. A. Kalogirou, “Solar thermal collectors and applications,” Prog Energy Combust Sci, vol. 30, no. 3, pp. 231–295, Jan. 2004, doi: 10.1016/J.PECS.2004.02.001.

[6] A. Yadav, N. Kumar, and K. Tharani, Implementing Solar PV System in DC Microgrid for Electric Vehicle Charging. 2024. doi: 10.1007/978-981-99-8343-8_2.

[7] A. Elottri, M. Boudiaf, A. Ghelam, and L. Mazouz, “Real-Time Control with MPPT Method (P&O) and PI Regulation of a PV system using the Arduino-Uno Card,” in 2022 2nd International Conference on Advanced Electrical Engineering, ICAEE 2022, 2022. doi: 10.1109/ICAEE53772.2022.9962138.

[8] M. Mortadi and A. El Fadar, Solar thermal systems: applications, techno-economic assessment, and challenges, vol. 2. 2023. doi: 10.1016/B978-0-443-18439-0.00005-7.

[9] A. Borode, T. Tshephe, and P. Olubambi, “A critical review of the thermophysical properties and applications of carbon-based hybrid nanofluids in solar thermal systems,” Front Energy Res, vol. 12, p. 1509437, Jan. 2024, doi: 10.3389/FENRG.2024.1509437/XML/NLM.

[10] G. N. Tiwari, A. Tiwari, and Shyam, Flat-Plate Collectors, vol. Part F2123. 2016. doi: 10.1007/978-981-10-0807-8_5.

[11] M. M. A. Khan, N. I. Ibrahim, I. M. Mahbubul, H. Muhammad. Ali, R. Saidur, and F. A. Al-Sulaiman, “Evaluation of solar collector designs with integrated latent heat thermal energy storage: A review,” May 15, 2018, Elsevier Ltd. doi: 10.1016/j.solener.2018.03.014.

[12] G. Boussouar, B. Rostane, K. Aliane, D. Ravi, M. J. Gęca, and A. Gola, “Study of the Thermal Performance of Solar Air Collectors with and without Perforated Baffles,” Energies (Basel), vol. 17, no. 15, 2024, doi: 10.3390/en17153812.

[13] S. Alsaqoor, A. Alqatamin, A. Alahmer, Z. Nan, Y. Al-Husban, and H. Jouhara, “The impact of phase change material on photovoltaic thermal (PVT) systems: A numerical study,” International Journal of Thermofluids, vol. 18, p. 100365, May 2023, doi: 10.1016/J.IJFT.2023.100365.

[14] M. S. Thakare, P. C. Ghosh, and S. Bandyopadhyay, “Optimal sizing of a photovoltaic-thermal hybrid system using energy ratio,” Chem Eng Trans, vol. 45, pp. 373–378, 2015, doi: 10.3303/CET1545063.

[15] M. E. Zayed, J. Zhao, Y. Du, A. E. Kabeel, and S. M. Shalaby, “Factors affecting the thermal performance of the flat plate solar collector using nanofluids: A review,” Apr. 01, 2019, Elsevier Ltd. doi: 10.1016/j.solener.2019.02.054.

[16] E. Vengadesan and R. Senthil, “A review on recent developments in thermal performance enhancement methods of flat plate solar air collector,” Renewable and Sustainable Energy Reviews, vol. 134, p. 110315, Dec. 2020, doi: 10.1016/J.RSER.2020.110315.

[17] Y. Kumar, M. Verma, H. K. Ghritlahre, and P. Verma, “Recent Developments in the Thermal Performance of Flat Plate Solar Water Heaters with Reflectors-A Review,” Energy Sources, Part A: Recovery, Utilization and Environmental Effects, vol. 44, no. 4, pp. 9448–9475, 2022, doi: 10.1080/15567036.2022.2131940.

[18] A. K. Singh and S. K. Verma, “Passive techniques for the thermal performance enhancement of flat plate solar collector: A comprehensive review,” Proceedings of the Institution of Mechanical Engineers, Part E: Journal of Process Mechanical Engineering, 2024, doi: 10.1177/09544089241270833.

[19] Y. Selikhov, J. J. Klemeš, P. Kapustenko, and O. Arsenyeva, “The study of flat plate solar collector with absorbing elements from a polymer material,” Energy, vol. 256, 2022, doi: 10.1016/j.energy.2022.124677.

[20] B. I. Kazandzhan, “Combined solar collectors,” J Phys Conf Ser, vol. 1683, no. 4, p. 042085, Dec. 2020, doi: 10.1088/1742-6596/1683/4/042085.

[21] A. R. Kalaiarasi, S. Aswin, M. Mukilan, and D. Rohith, “Literature Review on Optimizing Solar Panel Efficiency through Dynamic Solar Tracking,” in 3rd International Conference on Electronics and Renewable Systems, ICEARS 2025 - Proceedings, 2025, pp. 13–18. doi: 10.1109/ICEARS64219.2025.10940969.

[22] M. R. Assari, H. B. Tabrizi, H. Kavoosi, and M. Moravej, “Design and performance of dual-purpose solar collector,” in Proceedings of 3rd International Energy, Exergy and Environment Symposium, 2006, pp. 1–5.

[23] M. R. Assari, H. Basirat Tabrizi, and I. Jafari, “Experimental and theoretical investigation of dual purpose solar collector,” Solar Energy, vol. 85, no. 3, pp. 601–608, Mar. 2011, doi: 10.1016/j.solener.2011.01.006.

[24] M. R. Assari, H. B. Tabrizi, I. Jafari, and E. Najafpour, “An energy and exergy analysis of water and air with different passage in a solar collector,” Energy Sources, Part A: Recovery, Utilization and Environmental Effects, vol. 36, no. 7, pp. 747–754, Apr. 2014, doi: 10.1080/15567036.2010.540627.

[25] A. Ershadi, “Energy and exergy analysis of dual purpose solar collector,” 2011. [Online]. Available: https://www.researchgate.net/publication/288457522

[26] J. Ma, W. Sun, J. Ji, Y. Zhang, A. Zhang, and W. Fan, “Experimental and theoretical study of the efficiency of a dual-function solar collector,” Appl Therm Eng, vol. 31, no. 10, pp. 1751–1756, Jul. 2011, doi: 10.1016/j.applthermaleng.2011.02.019.

[27] A. V. A. K and A. P, “Simulation Studies on Porous Medium Integrated Dual Purpose Solar Collector,” International Journal Of Renewable Energy Research, vol. 3, no. 1, pp. 114–120, Mar. 2013, Accessed: May 11, 2025. [Online]. Available: https://dergipark.org.tr/en/pub/ijrer/issue/16080/168279

[28] O. Nematollahi, P. Alamdari, and M. R. Assari, “Experimental investigation of a dual purpose solar heating system,” Energy Convers Manag, vol. 78, pp. 359–366, 2014, doi: 10.1016/j.enconman.2013.10.046.

[29] P. Ganesh Kumar, K. Balaji, D. Sakthivadivel, V. S. Vigneswaran, R. Velraj, and S. C. Kim, “Enhancement of heat transfer in a combined solar air heating and water heater system,” Energy, vol. 221, p. 119805, Apr. 2021, doi: 10.1016/J.ENERGY.2021.119805.

[30] N. G. More and R. Pole, “Numerical and experimental investigation of dual purpose solar collector,” International Journal of Engineering Research & Technology (IJERT)-07-8 (Article), 2018.

[31] R. Miao, X. Hu, Y. Yu, Y. Zhang, M. Wood, and G. Olson, “Experimental study of a newly developed dual-purpose solar thermal collector for heat and cold collection,” Energy Build, vol. 252, Dec. 2021, doi: 10.1016/j.enbuild.2021.111370.

[32] A. Mohajer, O. Nematollahi, M. M. Joybari, S. A. Hashemi, and M. R. Assari, “Experimental investigation of a Hybrid Solar Drier and Water Heater System,” Energy Convers Manag, vol. 76, pp. 935–944, 2013, doi: 10.1016/j.enconman.2013.08.047.

[33] T. Rajaseenivasan and K. Srithar, “Potential of a dual purpose solar collector on humidification dehumidification desalination system,” Desalination, vol. 404, pp. 35–40, Feb. 2017, doi: 10.1016/J.DESAL.2016.10.015.

[34] M. M. Hasan and K. Hriczó, “A Literature Review of a Dual-Purpose Solar Collector,” Lecture Notes in Mechanical Engineering, pp. 302–321, 2023, doi: 10.1007/978-3-031-15211-5_26.

[35] J. Ma, H. Wang, Y. Wang, W. Sun, and J. Ji, “Performance Investigation and Structure Optimization of a Flat Dual-Function Solar Collector,” International Journal of Photoenergy, vol. 2015, 2015, doi: 10.1155/2015/532059.

[36] D. Zhang, J. Li, Z. Gao, L. Wang, and J. Nan, “Thermal performance investigation of modified flat plate solar collector with dual-function,” Appl Therm Eng, vol. 108, pp. 1126–1135, Sep. 2016, doi: 10.1016/J.APPLTHERMALENG.2016.07.200.

[37] J. Ji, C. Luo, T. T. Chow, W. Sun, and W. He, “Thermal characteristics of a building-integrated dual-function solar collector in water heating mode with natural circulation,” Energy, vol. 36, no. 1, pp. 566–574, 2011, doi: 10.1016/j.energy.2010.10.004.

[38] B. Luo, Z. Hu, X. Hong, and W. He, “Experimental Study of the Water Heating Performance of a Novel Tile-shaped Dual-function Solar Collector,” in Energy Procedia, Elsevier Ltd, 2015, pp. 87–94. doi: 10.1016/j.egypro.2015.02.102.

[39] W. He, X. Hong, B. Luo, H. Chen, and J. Ji, “CFD and comparative study on the dual-function solar collectors with and without tile-shaped covers in water heating mode,” Renew Energy, vol. 86, pp. 1205–1214, Feb. 2016, doi: 10.1016/j.renene.2015.09.053.

[40] Z. Hu, B. Luo, W. He, D. Hu, J. Ji, and J. Ma, “Performance study of a dual-function roof solar collector for Chinese traditional buildings application,” Appl Therm Eng, vol. 128, pp. 179–188, 2018, doi: 10.1016/j.applthermaleng.2017.09.019.

[41] J. Ma et al., “The thermal behavior of a dual-function solar collector integrated with building: An experimental and numerical study on the air heating mode,” Energies (Basel), vol. 11, no. 9, Sep. 2018, doi: 10.3390/en11092402.

[42] I. ASHRAE, 2009 ASHRAE handbook: Fundamentals. American Society of Heating, Refrigeration and Air-Conditioning Engineers, 2009.

[43] M. AbdEl-Rady Abu-Zeid et al., “Performance enhancement of flat-plate and parabolic trough solar collector using nanofluid for water heating application,” Results in Engineering, vol. 21, p. 101673, Mar. 2024, doi: 10.1016/J.RINENG.2023.101673.

[44] Y. Guo, Z. Mo, R. Zhang, D. Wang, and J. Fan, “Thermal–Hydraulic Performance of Flat-Plate Solar Collector Plant Using Different Heat-Transfer Fluids,” Energy Technology, p. 2400412, 2024.

[45] G. Sekrani and S. Poncet, “Ethylene- and propylene-glycol based nanofluids: A litterature review on their thermophysical properties and thermal performances,” Applied Sciences (Switzerland), vol. 8, no. 11, Nov. 2018, doi: 10.3390/app8112311.

[46] D. Balamurali and M. Natarajan, “Numerical-Experimental Analysis of Solar Liquid Flat-Plate Collector with Different HTF and Internal Grooves Profiles in the Absorber Duct,” Applied Solar Energy (English translation of Geliotekhnika), vol. 59, no. 3, pp. 244–252, Jun. 2023, doi: 10.3103/S0003701X21101175.

[47] P. Narayana Prasad and S. Kalla, “Numerical investigation of solar flat plate collector using different working fluids,” International Journal of Ambient Energy, vol. 44, no. 1, pp. 483–493, 2023, doi: 10.1080/01430750.2022.2128419.

[48] A. O. Borode, N. A. Ahmed, P. A. Olubambi, M. Sharifpur, and J. P. Meyer, “Investigation of the Thermal Conductivity, Viscosity, and Thermal Performance of Graphene Nanoplatelet-Alumina Hybrid Nanofluid in a Differentially Heated Cavity,” Front Energy Res, vol. 9, p. 737915, Aug. 2021, doi: 10.3389/FENRG.2021.737915/BIBTEX.

[49] S. P. Tembhare, D. P. Barai, and B. A. Bhanvase, “Performance evaluation of nanofluids in solar thermal and solar photovoltaic systems: A comprehensive review,” Jan. 01, 2022, Elsevier Ltd. doi: 10.1016/j.rser.2021.111738.

[50] Q. Al-Yasiri, M. Szabó, and M. Arıcı, “Single and hybrid nanofluids to enhance performance of flat plate solar collectors: Application and obstacles,” Periodica Polytechnica Mechanical Engineering, vol. 65, no. 1, pp. 86–102, 2021, doi: 10.3311/PPme.17312.

[51] M. S. Kamel and F. Lezsovits, “Experimental Study on Pool Boiling Heat Transfer Performance of Magnesium Oxide Nanoparticles Based Water Nanofluid,” Pollack Periodica, vol. 15, no. 3, pp. 101–112, Nov. 2020, doi: 10.1556/606.2020.15.3.10.

[52] R. Saidur, K. Y. Leong, and H. A. Mohammed, “A review on applications and challenges of nanofluids,” Renewable and Sustainable Energy Reviews, vol. 15, no. 3, pp. 1646–1668, Apr. 2011, doi: 10.1016/J.RSER.2010.11.035.

[53] Y. Zhang et al., “Obtaining an accurate prediction model for viscosity of a new nano-lubricant containing multi-walled carbon nanotube-titanium dioxide nanoparticles with oil SAE50,” Tribol Int, vol. 191, p. 109185, Mar. 2024, doi: 10.1016/J.TRIBOINT.2023.109185.

[54] M. M. Hasan and K. Hriczó, “Evaluation of a dual-purpose solar collector using mono-nanofluids: A CFD simulation,” Pollack Periodica, vol. 1, no. aop, Oct. 2025, doi: 10.1556/606.2025.01394.

[55] E. Ekramian, … S. E.-I. J. of, and undefined 2014, “Numerical investigations of heat transfer performance of nanofluids in a flat plate solar collector,” ijtan.avestia.com, Accessed: Apr. 15, 2025. [Online]. Available: https://ijtan.avestia.com/2014/005.html

[56] S. K. Verma, A. K. Tiwari, and D. S. Chauhan, “Experimental evaluation of flat plate solar collector using nanofluids,” Energy Convers Manag, vol. 134, pp. 103–115, Jan. 2017, doi: 10.1016/j.enconman.2016.12.037.

[57] Y. Devarajan and D. B. Munuswamy, “Analysis on the Influence of Nanoparticles of Alumina, Copper Oxide, and Zirconium Oxide on the Performance of a Flat-Plate Solar Water Heater,” Energy and Fuels, vol. 30, no. 11, pp. 9908–9913, Nov. 2016, doi: 10.1021/ACS.ENERGYFUELS.6B02264.

[58] M. A. Alim, Z. Abdin, R. Saidur, A. Hepbasli, M. A. Khairul, and N. A. Rahim, “Analyses of entropy generation and pressure drop for a conventional flat plate solar collector using different types of metal oxide nanofluids,” Energy Build, vol. 66, pp. 289–296, Nov. 2013, doi: 10.1016/J.ENBUILD.2013.07.027.

[59] Z. Hajabdollahi, H. Hajabdollahi, and K. C. Kim, “Multi-objective optimization of solar collector using water-based nanofluids with different types of nanoparticles,” J Therm Anal Calorim, vol. 140, no. 3, pp. 991–1002, May 2020, doi: 10.1007/S10973-019-08444-W/FIGURES/6.

[60] Y. Tong, H. Lee, W. Kang, and H. Cho, “Energy and exergy comparison of a flat-plate solar collector using water, Al2O3 nanofluid, and CuO nanofluid,” Appl Therm Eng, vol. 159, p. 113959, Aug. 2019, doi: 10.1016/J.APPLTHERMALENG.2019.113959.

[61] D. B. Munuswamy, Y. Devarajan, M. N. Babu, and S. Ramalingam, “Experimental investigation on lowering the environmental hazards and improving the performance patterns of solar flat plate collectors by employing the internal longitudinal fins and nano additives,” Environmental Science and Pollution Research, vol. 27, no. 36, pp. 45390–45404, Dec. 2020, doi: 10.1007/S11356-020-10311-3/FIGURES/33.

[62] A. A. Hawwash, M. Ahamed, S. A. Nada, A. Radwan, and A. K. Abdel-Rahman, “Thermal Analysis of Flat Plate Solar Collector Using Different Nanofluids and Nanoparticles Percentages,” IEEE Access, vol. 9, pp. 52053–52066, 2021, doi: 10.1109/ACCESS.2021.3060004.

[63] F. Bazdidi-Tehrani, A. Khabazipur, and S. I. Vasefi, “Flow and heat transfer analysis of TiO2/water nanofluid in a ribbed flat-plate solar collector,” Renew Energy, vol. 122, pp. 406–418, Jul. 2018, doi: 10.1016/J.RENENE.2018.01.056.

[64] O. Al-Oran and F. Lezsovits, “Thermal performance of inserting hybrid nanofluid in parabolic trough collector,” Pollack Periodica, vol. 16, no. 3, pp. 88–93, Apr. 2021, doi: 10.1556/606.2021.00318.

[65] Q. Al-Yasiri, M. Szabó, and M. Arıcı, “Single and hybrid nanofluids to enhance performance of flat plate solar collectors: Application and obstacles,” Periodica Polytechnica Mechanical Engineering, vol. 65, no. 1, pp. 86–102, Jan. 2021, doi: 10.3311/PPme.17312.

[66] A. Vărdaru, G. Huminic, A. Huminic, C. Fleacă, F. Dumitrache, and I. Morjan, “Synthesis, characterization and thermal conductivity of water based graphene oxide–silicon hybrid nanofluids: An experimental approach,” Alexandria Engineering Journal, vol. 61, no. 12, pp. 12111–12122, Dec. 2022, doi: 10.1016/J.AEJ.2022.06.012.

[67] A. Borode, T. Tshephe, and P. Olubambi, “A critical review of the thermophysical properties and applications of carbon-based hybrid nanofluids in solar thermal systems,” Front Energy Res, vol. 12, p. 1509437, Jan. 2024, doi: 10.3389/FENRG.2024.1509437/XML/NLM.

[68] E. Elshazly, A. A. Abdel-Rehim, and I. El-Mahallawi, “4E study of experimental thermal performance enhancement of flat plate solar collectors using MWCNT, Al2O3, and hybrid MWCNT/ Al2O3 nanofluids,” Results in Engineering, vol. 16, p. 100723, Dec. 2022, doi: 10.1016/J.RINENG.2022.100723.

[69] S. Singh, K. Mausam, S. K. Ghosh, and A. K. Tiwari, “An experimental and numerical approach for thermal performance investigation of solar flat plate collector,” Environmental Science and Pollution Research, vol. 30, no. 40, pp. 92859–92879, Aug. 2023, doi: 10.1007/S11356-023-28843-9/FIGURES/18.

[70] S. K. Verma, A. K. Tiwari, and D. S. Chauhan, “Experimental evaluation of flat plate solar collector using nanofluids,” Energy Convers Manag, vol. 134, pp. 103–115, Feb. 2017, doi: 10.1016/J.ENCONMAN.2016.12.037.

[71] Z. Said, R. Saidur, N. A. Rahim, and M. A. Alim, “Analyses of exergy efficiency and pumping power for a conventional flat plate solar collector using SWCNTs based nanofluid,” Energy Build, vol. 78, pp. 1–9, Aug. 2014, doi: 10.1016/J.ENBUILD.2014.03.061.

[72] H. Nabi, M. Pourfallah, M. Gholinia, and O. Jahanian, “Increasing heat transfer in flat plate solar collectors using various forms of turbulence-inducing elements and CNTs-CuO hybrid nanofluids,” Case Studies in Thermal Engineering, vol. 33, May 2022, doi: 10.1016/j.csite.2022.101909.

[73] M. Hemmat Esfe, A. Alirezaie, and M. Rejvani, “An applicable study on the thermal conductivity of SWCNT-MgO hybrid nanofluid and price-performance analysis for energy management,” Appl Therm Eng, vol. 111, pp. 1202–1210, Jan. 2017, doi: 10.1016/J.APPLTHERMALENG.2016.09.091.

[74] A. M. Ajeena, I. Farkas, and P. Víg, “Performance enhancement of flat plate solar collector using ZrO2-SiC/DW hybrid nanofluid: A comprehensive experimental study,” Energy

Conversion and Management: X, vol. 20, p. 100458, Oct. 2023, doi: 10.1016/J.ECMX.2023.100458.

[75] K. A. Al-Shibli and A. K. Hussein, “Enhancement the Performance of FPSC by Utilizing Hybrid Nanofluids - An Extended Review,” International Journal of Heat and Technology, vol. 42, no. 6, pp. 1901–1910, Dec. 2024, doi: 10.18280/IJHT.420607.

[76] S. T. Hamidi, “An Analysis of the Impact of a Nanoparticle’s Sizing on the Effectiveness of Solar Collector Based on Nanofluids,” in 4th International Conference on Current Research in Engineering and Science Applications Iccresa 2022, 2022, pp. 273–277. doi: 10.1109/ICCRESA57091.2022.10352451.

[77] S. M. S. Hosseini, D. Ayar, A. Talebizadeh, and M. Kamyabi, “An experimental investigation on the solar–thermal energy conversion performance of Fe2O3 nanofluid with the focus on nanoparticles shape and concentration,” Int J Energy Res, vol. 46, no. 5, pp. 6126–6143, 2022, doi: 10.1002/er.7553.

[78] A. Z. Sahin, M. A. Uddin, B. S. Yilbas, and A. Al-Sharafi, “Performance enhancement of solar energy systems using nanofluids: An updated review,” Renew Energy, vol. 145, pp. 1126–1148, 2020, doi: 10.1016/j.renene.2019.06.108.

[79] J. Dai, Y. Zhai, Z. Li, and H. Wang, “Mechanism of enhanced thermal conductivity of hybrid nanofluids by adjusting mixing ratio of nanoparticles,” J Mol Liq, vol. 400, 2024, doi: 10.1016/j.molliq.2024.124518.

[80] H.-R. Bahrami, O. Allahdadi, and H. Saffari, “Nanofluids for advanced thermal management: A multi-criteria review of performance, cost, and environmental impacts,” Results in Materials, vol. 27, 2025, doi: 10.1016/j.rinma.2025.100753.

[81] M. Faizal, R. Saidur, and S. Mekhilef, “Potential of size reduction of flat-plate solar collectors when applying Al2O3 nanofluid,” Adv Mat Res, vol. 832, pp. 149–153, 2014, doi: 10.4028/WWW.SCIENTIFIC.NET/AMR.832.149.

[82] R. S. and S. M. M Faizal, “Potential of size reduction of flat-plate solar collectors when applying MWCNT nanofluid,” IOP Conf Ser Earth Environ Sci, vol. 16, no. 1, p. 012004, Jun. 2013, doi: 10.1088/1755-1315/16/1/012004.

[83] M. Faizal, R. Saidur, S. Mekhilef, and M. A. Alim, “Energy, economic and environmental analysis of metal oxides nanofluid for flat-plate solar collector,” Energy Convers Manag, vol. 76, pp. 162–168, Dec. 2013, doi: 10.1016/J.ENCONMAN.2013.07.038.

[84] P. Michael Joseph Stalin, T. V. Arjunan, M. M. Matheswaran, H. Dolli, and N. Sadanandam, “Energy, economic and environmental investigation of a flat plate solar collector with CeO2/water nanofluid,” J Therm Anal Calorim, vol. 139, no. 5, pp. 3219–3233, Mar. 2020, doi: 10.1007/S10973-019-08670-2/TABLES/11.

[85] A. Somwanshi and N. Sarkar, “Thermal performance of a dual-purpose collector-cum-storage type air-water heater,” Appl Therm Eng, vol. 171, May 2020, doi: 10.1016/j.applthermaleng.2020.115094.

[86] E. G. Varuvel, A. Sonthalia, F. Aloui, and C. G. Saravanan, “Basics of heat transfer: Heat exchanger,” Handbook of Thermal Management Systems: E-Mobility and Other Energy Applications, pp. 79–93, Jan. 2023, doi: 10.1016/B978-0-443-19017-9.00016-7.

[87] D. Zhang, J. Li, Z. Gao, L. Wang, and J. Nan, “Thermal performance investigation of modified flat plate solar collector with dual-function,” Appl Therm Eng, vol. 108, pp. 1126–1135, Sep. 2016, doi: 10.1016/j.applthermaleng.2016.07.200.

[88] J. A. Duffie and W. A. Beckman, Solar engineering of thermal processes. John Wiley & Sons, 2013.

[89] J. P. Holman, Heat Transfer (Si Units) Sie. Tata McGraw-Hill Education, 2008.

[90] M. H. Tariq, F. Khan, and T. A. Cheema, “Analytical and Experimental Investigation of a Triangular-Channeled Solar Water Heater †,” Engineering Proceedings, vol. 12, no. 1, 2021, doi: 10.3390/ENGPROC2021012017.

[91] S. Daviran, A. Kasaeian, H. Tahmooressi, A. Rashidi, D. Wen, and O. Mahian, “Evaluation of clustering role versus Brownian motion effect on the heat conduction in nanofluids: A novel approach,” Int J Heat Mass Transf, vol. 108, pp. 822–829, 2017, doi: 10.1016/j.ijheatmasstransfer.2016.12.071.

[92] M. Misale, J. A. Bocanegra, and A. Marchitto, “Long-term experimental study on gravitational sedimentation of water aluminum oxide nanofluid at different volumetric concentrations,” International Journal of Sediment Research, vol. 38, no. 3, pp. 303–315, 2023, doi: 10.1016/j.ijsrc.2023.01.002.

[93] D. Song, D. Jing, W. Ma, and X. Zhang, “Effect of particle aggregation on thermal conductivity of nanofluids: Enhancement of phonon MFP,” J Appl Phys, vol. 125, no. 1, 2019, doi: 10.1063/1.5062600.

[94] L. H. Kumar, S. N. Kazi, H. H. Masjuki, M. N. M. Zubir, A. Jahan, and C. Bhinitha, “Energy, exergy and economic analysis of liquid flat-plate solar collector using green covalent functionalized graphene nanoplatelets,” Appl Therm Eng, vol. 192, p. 116916, Jun. 2021, doi: 10.1016/J.APPLTHERMALENG.2021.116916.

[95] L. Anto Joseph Deeyoko, K. Balaji, S. Iniyan, and C. Sharmeela, “Exergy, economics and pumping power analyses of flat plate solar water heater using thermal performance enhancer in absorber tube,” Appl Therm Eng, vol. 154, pp. 726–737, May 2019, doi: 10.1016/J.APPLTHERMALENG.2019.03.135.

[96] M. Amar et al., “Energy, exergy and economic (3E) analysis of flat-plate solar collector using novel environmental friendly nanofluid,” Scientific Reports 2023 13:1, vol. 13, no. 1, pp. 1–21, Jan. 2023, doi: 10.1038/s41598-023-27491-w.

[97] M. M. Hasan and K. Hriczó, “The optimal approach of various analysis methodologies of a dual-purpose solar collector,” Pollack Periodica, vol. 20, no. 2, pp. 130–135, Apr. 2025, doi: 10.1556/606.2024.01244.

[98] X. Han, C. Li, and H. Ma, “Performance Studies and Energy-Saving Analysis of a Solar Water-Heating System,” Processes 2021, Vol. 9, Page 1536, vol. 9, no. 9, p. 1536, Aug. 2021, doi: 10.3390/PR9091536.

[99] I. Omle, E. Kovács, and B. Bolló, “Applying recent efficient numerical methods for long-term simulations of heat transfer in walls to optimize thermal insulation,” Results in Engineering, vol. 20, p. 101476, Dec. 2023, doi: 10.1016/J.RINENG.2023.101476.

[100] S. Mukherjee, D. Shah, P. Chaudhuri, and P. C. Mishra, “Exergy, economic, and environmental impact of a flat plate solar collector with Al2O3-CuO/Water hybrid nanofluid: Experimental study,” Appl Therm Eng, vol. 266, p. 125640, May 2025, doi: 10.1016/J.APPLTHERMALENG.2025.125640.

[101] M. M. Hasan and K. Hriczó, “A dual-purpose solar collector as a parallel flow heat exchanger: A novel mathematical framework,” International Journal of Thermofluids, vol. 28, p. 101322, Jul. 2025, doi: 10.1016/J.IJFT.2025.101322.

[102] D. C. Montgomery and G. C. Runger, Applied statistics and probability for engineers. John wiley & sons, 2019.

[103] A. A. M. Saleh and M. A. Jasim, “Experimental study of the performance of the dual purpose solar collector,” Eng. Technol. J, vol. 32, no. 11, pp. 2673–2683, 2014.

[104] A. A. M. Saleh and M. A. Jasim, “Experimental Study of The Performance of The Dual Purpose Solar Collector,” 2014.

[105] T. O. Hodson, “Root-mean-square error (RMSE) or mean absolute error (MAE): when to use them or not,” Geosci Model Dev, vol. 15, no. 14, pp. 5481–5487, 2022, doi: 10.5194/gmd-15-5481-2022.

[106] D. S. K. Karunasingha, “Root mean square error or mean absolute error? Use their ratio as well,” Inf Sci (N Y), vol. 585, pp. 609–629, 2022, doi: 10.1016/j.ins.2021.11.036.

[107] M. M. Hasan and K. Hriczó, “Numerical investigation of a dual- purpose solar collector using different liquids,” Pollack Periodica, vol. 1, no. aop, Sep. 2025, doi: 10.1556/606.2025.01379.

[108] J. Alsarraf, A. A. Alnaqi, and A. A. A. A. Al-Rashed, “Simulation of two-phase hybrid nanofluid flow in a flat plate solar collector equipped with spiral absorber tube under the influence of

magnetic field: Hydraulic-thermal, energy, and exergy analysis," J Magn Magn Mater, vol. 585, Nov. 2023, doi: 10.1016/j.jmmm.2023.171120.

[109] A. Mwesigye and İ. H. Yılmaz, "Thermal and thermodynamic benchmarking of liquid heat transfer fluids in a high concentration ratio parabolic trough solar collector system," J Mol Liq, vol. 319, Dec. 2020, doi: 10.1016/j.molliq.2020.114151.

[110] M. M. Hasan and K. Hriczó, "ENERGY, ECONOMIC, AND ECOLOGICAL ASPECTS OF A DUAL-PURPOSE SOLAR COLLECTOR USING VARIOUS LIQUIDS," Pollack Periodica, vol. (in press), 2026.

[111] B. Takabi and S. Salehi, "Augmentation of the Heat Transfer Performance of a Sinusoidal Corrugated Enclosure by Employing Hybrid Nanofluid," https://doi.org/10.1155/2014/147059, vol. 2014, Jan. 2014, doi: 10.1155/2014/147059.

LIST OF PUBLICATIONS RELATED TO THE TOPIC OF THE RESEARCH FIELD

P1. M. M. Hasan and K. Hriczó, “A dual-purpose solar collector as a parallel flow heat exchanger: A novel mathematical framework,” International Journal of Thermofluids, vol. 28, p. 101322, Jul. 2025, doi: 10.1016/J.IJFT.2025.101322.

P2. M. M. Hasan and K. Hriczó, “The optimal approach of various analysis methodologies of a dual-purpose solar collector,” Pollack Periodica, vol. 20, no. 2, pp. 130–135, Apr. 2025, doi: 10.1556/606.2024.01244.

P3. M. M. Hasan and K. Hriczó, “Numerical investigation of a dual- purpose solar collector using different liquids,” Pollack Periodica, vol. 1, no. aop, Sep. 2025, doi: 10.1556/606.2025.01379.

P4. M. M. Hasan and K. Hriczó, “Evaluation of a dual-purpose solar collector using mono-nanofluids: A CFD simulation,” Pollack Periodica, vol. 1, no. aop, Oct. 2025, doi: 10.1556/606.2025.01394.

P5. M. M. Hasan and K. Hriczó, “ENERGY, ECONOMIC, AND ECOLOGICAL ASPECTS OF A DUAL-PURPOSE SOLAR COLLECTOR USING VARIOUS LIQUIDS,” Pollack Periodica, vol. (in press), 2026.

P6. M. M. Hasan and K. Hriczó, “A Literature Review of a Dual-Purpose Solar Collector,” Lecture Notes in Mechanical Engineering, pp. 302–321, 2023, doi: 10.1007/978-3-031-15211-5_26.

P7. M. M. Hasan and K. Hriczó, “Heating a greenhouse using a solar air collector assisted by thermal storage: a simulation study,” Multidiszciplináris Tudományok, vol. 12, no. 3, pp. 217–232, Nov. 2022, doi: 10.35925/J.MULTI.2022.3.20.

P8. M. M. Hasan and K. Hriczó, “Thermal performance estimation of a v-corrugated solar air heater using ann techniques,” Multidiszciplináris Tudományok, vol. 13, no. 4, pp. 42–53, Dec. 2023, doi: 10.35925/J.MULTI.2023.4.5.